Measurement of isolated photons in pp collisions at $\sqrt{s} = 7$ TeV with ALICE

Dissertation
zur Erlangung des Doktorgrades
der Naturwissenschaften

vorgelegt beim Fachbereich Physik
der Johann Wolfgang Goethe-Universität
in Frankfurt am Main

von

Marco Marquard
aus Frankfurt am Main

Frankfurt 2021
(D 30)

Vom Fachbereich Physik
der Johann Wolfgang Goethe-Universität als Dissertation angenommen.

Dekan: Prof. Dr. Harald Appelshäuser

Gutachter: Prof. Dr. Henner Büsching
Prof. Dr. Harald Appelshäuser

Datum der Disputation:

Zusammenfassung

Teilchenkollisionen haben unser aktuelles Bild von der Zusammensetzung der Materie entscheidend geprägt und vervollständigt. Trotz dieses großen Erfolges und dem daraus hervorgegangenen Standardmodell der Teilchenphysik, können Teilchenkollisionen weiterhin neue Erkenntnisse liefern. Im Rahmen dieser Arbeit werden die Messungen von zwei Observablen, der mittlere Transversalimpuls geladener Teilchen und der Wirkungsquerschnitt isolierter Photonen, behandelt. Die Ergebnisse beider Messungen tragen zusammen mit weiteren Messungen zu unserem Verständnis des Quark-Gluon-Plasmas (QGP) bei. Beim QGP handelt es sich um einen Zustand der Materie, bei dem sich Quarks und Gluonen frei bewegen können und der nicht dem Confinement unterliegt. Nach dem aktuellen Verständnis zur Entstehung des Universums hat ein QGP kurze Zeit nach dem Urknall existiert, bevor daraus Hadronen und schlussendlich Atomkerne entstehen konnten. Ähnliche Bedingungen wie kurz nach dem Urknall können durch Schwerionenkollisionen in Teilchenbeschleunigern erzeugt werden und ermöglichen so die Untersuchung von Materie bei hohen Temperaturen und Dichten, sowie die Suche nach einem QGP und dessen Charakterisierung. Der Wechselwirkungsquerschnitt isolierter Photonen trägt des Weiteren zur Bestimmung der Partondichtefunktion (PDF) von Gluonen in Protonen bei.

Die Analyse der beiden Observablen wurde auf Basis von Daten von ALICE am LHC durchgeführt. Beim LHC handelt es sich um den aktuell größten Teilchenbeschleuniger auf der Erde. ALICE, als eines von vier großen Experimenten am LHC, beschäftigt sich vor allem mit der Erforschung des QGP. Die anderen drei großen Experimente haben ihren Fokus auf der Erforschung des Standardmodells und dessen Erweiterung (ATLAS, CMS) oder auf der Präzisionsmessung der CP-Verletzung (LHCb). Als Hauptdetektoren für die Analyse wurden der innere Tracker (ITS), die Spurdriftkammer (TPC) und das elektromagnetische Kalorimeter (EMCal) genutzt. Beim ITS handelt es sich um einen 6-lagigen Siliziumdetektor, der zur genauen Bestimmung des Kollisionsortes, wie auch der Spurbestimmung von geladenen Teilchen genutzt wird. Zusammen mit der TPC lässt sich sowohl der Impuls der Teilchen messen, als auch ihre Art identifizieren. Die Messung von Photonen erfolgt mithilfe des EMCal. Dabei handelt es sich um ein elektromagnetisches Kalorimeter in Schaschlikbauweise, das schichtweise aus Blei und einem Szintillator aufgebaut ist. Dabei dient das Blei als Absorber und der Szin-

tillator als Detektionsmaterial. Die Auslese ist in kleine Zellen unterteilt, wobei die Kantenlänge einer Zelle ungefähr dem Molière Radius (R_M) entspricht, um eine gute Ortsauflösung zu erhalten. Im Rahmen der Datenverarbeitung werden die Signale einzelner Zellen mit benachbarten Zellen zu Clustern kombiniert. Damit ein Cluster erzeugt wird, muss eine Zelle den Start-Schwellenwert überschreiten. Anschließend werden weitere Zellen dem Cluster hinzugefügt, für diese Zellen gilt ein niedrigerer Schwellenwert (Zell-Schwelle). Weiterhin ist es möglich, Cluster, die mehr als ein lokales Maximum besitzen, in mehrere Cluster aufzuspalten. Unter idealen Bedingungen entspricht ein Cluster einem Teilchen, das das Kalorimeter getroffen hat.

Für die Messung des mittleren Transversalimpulses wurde der Pb–Pb Datensatz von 2010 verwendet, während für die Messung des Wechselwirkungsquerschnitts isolierter Photonen pp Kollisionen mit einer Schwerpunktsenergie von $\sqrt{s} = 7\,\mathrm{TeV}$ genutzt wurden. Um eine bessere Statistik bei hohen Photonenenergien zu erhalten, wurde für die Datennahme der pp Kollisionen ein Trigger auf die Energie im EMCal genutzt. Da in pp Kollisionen kein QGP erzeugt wird, dienen sie als Referenzwert beim Studium des QGP in Schwerionenkollisionen.

Bei der Untersuchung des mittleren Transversalimpulses steht vor allem der Vergleich zwischen drei Kollisionssystemen (pp, p–Pb, Pb–Pb) im Vordergrund. Aus dem Vergleich der verschiedenen Kollisionssysteme ergeben sich zwei Herausforderungen. Zum einen muss eine geeignete Observable gewählt werden, die eine Vergleichbarkeit aller Kollisionssysteme ermöglicht und zum anderen entspricht der Vergleichsbereich in Pb–Pb Kollisionen peripheren Kollisionen, die durch einen hohen Untergrund von elektromagnetischen Teilchen dominiert werden. Für den Vergleich wird $\langle p_T \rangle$ als Funktion der wahren Eventmultiplizität n_{ch} berechnet. Dies gewährleistet sowohl die Vergleichbarkeit der verschiedenen Kollisionssysteme, als auch die Nutzung in theoretischen Berechnungen. Um $\langle p_T \rangle$ als Funktion von n_{ch} zu erhalten, müssen die gemessenen Werte für $\langle p_T \rangle$ als Funktion der gemessenen Multiplizität n_{acc} umgerechnet werden. Diese Umrechnung wird durch eine Neugewichtung der gemessenen Werte mithilfe einer $n_{acc} - n_{ch}$ Korrelationsmatrix erreicht.

Zur Studie des elektromagnetischen Untergrundes in peripheren Ereignissen wird das Signal im Zero-Degree Calorimeter mit und ohne Zentralitätsselektionen betrachtet. Aus der Studie ergibt sich eine effektive Reduktion der EM-Interaktionen, die nach aktuellem Kenntnisstand nicht vollständig die unerwünschten Interaktionen

unterdrückt. Zur Abschätzung des verbleibenden Einflusses der EM-Interaktionen wird die Analyse mit zwei unterschiedlichen Zentralitätsselektionen (0 % - 100 % und 0 % - 90 %) durchgeführt. Die Differenz der Ergebnisse wird als zusätzlicher Beitrag zu den systematischen Fehlern behandelt.

Der Vergleich der verschiedenen Kollisionssysteme zeigt ein ähnliches Verhalten mit starkem $\langle p_{\mathrm{T}} \rangle$-Anstieg für niedrige Multiplizitäten für alle Kollisionssysteme. Bei einer Multiplizität von ca. $n_{\mathrm{ch}} = 14$ flacht sich der $\langle p_{\mathrm{T}} \rangle$-Anstieg für alle Systeme ab. Für Pb–Pb Kollisionen steigt $\langle p_{\mathrm{T}} \rangle$ im Vergleichsbereich bis $n_{\mathrm{ch}} = 100$ nur noch leicht an, während pp und p–Pb Kollisionen einen weiteren Anstieg verzeichnen. Dabei fällt der Steigung von p–Pb nicht ganz so steil aus wie für pp Kollisionen. Für diese beiden Kollisionssysteme limitiert die Statistik die Mutliplizitätsreichweite.

Die in dieser Arbeit präsentierten Ergebnisse wurden 2013 in [ALICE|13d] veröffentlicht. In der Zwischenzeit sind Datensätze mit besserer Statistik und weiteren Kollisionssystemen und -energien verfügbar geworden. Des Weiteren wurde als Verbesserung zur Neugewichtung eine Methode basierend auf einer Bayesschen Entfaltung entwickelt, sodass zukünftig verbesserte Resultate einen genaueren Vergleich ermöglichen.

Die zweite Analyse dieser Arbeit setzt sich mit der Messung isolierter Photonen auseinander. Dabei ist zu beachten, dass es sich bei isolierten Photonen um eine Messgröße handelt, die keinem expliziten physikalischen Prozess zugeordnet werden kann. Messtechnisch lassen sich die unterschiedlichen Photonenquellen einer Kollision nicht unterscheiden, da sie wohl zu unterschiedlichen Zeitpunkten produziert werden, diese aber nicht aufgelöst werden können. Für diese Arbeit von besonderem Interesse sind prompte Photonen, die in den ersten Parton-Parton Interaktionen einer Kollision produziert werden. Die Messung des Wechselwirkungsquerschnitts prompter Photonen kann zur Bestimmung der Partondichtefunktion (PDF) von Gluonen genutzt werden. In Schwerionenkollisionen wird der bei den vorrangigen Produktionsprozessen von prompten Photonen, Quark–Anti-Quark Annihilation und Quark-Gluon Streuung, zum Photon entgegengesetzt Partonschauer zur Untersuchung des QGP genutzt. Da nur der Partonschauer mit dem QGP interagiert, lässt sich die Modifikation des Schauers durch das QGP untersuchen. Als erster Schritt zur Untersuchung des QGP mithilfe von Photon-Schauer-Korrelationen dient eine Referenzmessung in pp Kollisionen, da hierbei keine Modifikation des Partonschauers stattfindet. Um experimentell eine möglichst reine

Probe prompter Photonen zu erhalten, nutzt man ein Isolationskriterium, um den Beitrag anderer Photonenquellen zu reduzieren. Zusätzlich nutzt man einen EMCal Trigger, um den Anteil von Ereignissen hochenergetischer Teilchen zu erhöhen. Eine entscheidende Herausforderung bei der Messung isolierter Photonen ist die Differenzierung von Hintergrund und Signal. Dazu wird die Clusterform, beschrieben durch den Parameter σ^2_{long}, mit der Energie innerhalb eines bestimmten Radiuses um den Cluster ($E_{\text{T}_{\text{iso}}}$) korreliert und ein gemeinsamer Phasenraum aufgespannt. Die parametrisierte Clusterform dient zur Unterscheidung zwischen einzelnen Photonen und Photonen aus hadronischen Zerfällen. Die Energie innerhalb von $E_{\text{T}_{\text{iso}}}$ dient als Isolationskriterium. In der vorliegenden Analyse wird ein Kriterium von 2 GeV als Schwellenwert genutzt. Der aufgespannte Phasenraum wird in vier Bereiche ($\mathcal{A}$, $\mathcal{B}$, $\mathcal{C}$, $\mathcal{D}$) aufgeteilt. Bei der Aufteilung werden die Grenzen so gewählt, dass die folgenden Annahmen erfüllt sind:

- Der Beitrag isolierter Photonen ist in den Regionen $\mathcal{B}$, $\mathcal{C}$ und $\mathcal{D}$ vernachlässigbar.
- Die Wahrscheinlichkeit für die Erfüllung des Isolationskriteriums ist unabhängig von der Clusterform.

Dementsprechend enthalten die drei Regionen $\mathcal{B}, \mathcal{C}$ und $\mathcal{D}$ nur Hintergrundcluster und in Region $\mathcal{A}$ sind sowohl Hintergrundcluster, als auch alle Signalcluster enthalten. Diese Aufteilung erlaubt es, den Hintergrund, die Reinheit in Region $\mathcal{A}$ und somit das Signal zu bestimmen. Da die oben genannten Kriterien nicht vollends erfüllt sind, wird die Reinheit mit einem Korrekturfaktor modifiziert. Nach der Bestimmung der Effizienz und der Akzeptanz lässt sich ein korrigiertes Spektrum isolierter Photon berechnen. In einem nächsten Schritt wird der Wechselwirkungsquerschnitt isolierter Photonen bei pp Kollisionen bestimmt. Der Wechselwirkungsquerschnitt kann in dem genutzten Datensatz zwischen 10 GeV/c und 60 GeV/c gemessen werden. Die Ergebnisse wurden erfolgreich in [ALICE|19b] publiziert.

Das Ergebnis wird über den gesamten p_{T}-Bereich mit dedizierten Simulationen verglichen. Da aufgrund unterschiedlicher Isolationskriterien ein direkter Vergleich mit vorherigen Messungen von ATLAS und CMS nicht möglich ist, werden die Verhältnisse von gemessenen Daten zu Simulationen verglichen. Sowohl für den Vergleich von gemessenen Daten zu Simulationen, als auch der Vergleich der Verhältnisse stimmen innerhalb ihrer Unsicherheiten überein. Im Vergleich der bisherigen Messungen am LHC ist sichtbar, dass die ALICE Messungen den bisherigen Messbereich zu

niedrigeren p_T Bereichen erweitert. Zum Vergleich des Wechselwirkungsquerschnitts bei verschiedenen Kollisionsenergien kann man die Ergebnisse als Funktion der Skalenvariablen x_T ($x_T = 2p_T^\gamma/\sqrt{s}$) anstatt p_T auftragen. Da x_T mit $\sqrt{s}$ skaliert, ergibt sich eine gute Vergleichbarkeit der Messungen über einen großen x_T Bereich. Dabei wird deutlich, dass die Messungen von ALICE den Messbereich auch in x_T zu niedrigeren Werten erweitern. Zudem stimmen die Ergebnisse von ALICE im Überlappbereich mit denen von vorherigen Messungen bei niedrigeren Energien überein.

Im Rahmen der Analyse wird durch verschiedene Variation der Analyse die systematische Unsicherheit der Messung ermittelt. Dabei werden Unsicherheiten der $\mathcal{ABCD}$-Methode, der verwendeten Simulationen und der Einfluss von Hardwareeffekten auf das Ergebnis berücksichtigt.

In einer weiteren Analyse wird der Einfluss von verschiedenen Clusterizer-Einstellungen, wie auch unterschiedlichen Clusterizern auf das Ergebnis untersucht. Bei den Clusterizer-Einstellungen werden die Mindestenergie zur Erzeugung eines Clusters und die Mindestenergie einer Zelle, damit sie zu einem Cluster beiträgt, variiert. Die Mindestenergie einer Zelle soll verhindern, dass Zellen ohne Signal durch elektronisches Rauschen zu einem Cluster beitragen. Diese Zellen haben wohl keinen großen Einfluss auf die Gesamtenergie des Clusters, können aber die Clusterform beeinflussen. Für die Untersuchung werden zusätzlich zum Standardwert von 100 MeV auch niedrigere Werte von 75 MeV und 50 MeV untersucht. Für die Erzeugung eines Clusters wird eine Startzelle benötigt, von der aus der Clusterizer weitere Zellen hinzufügt. Für die Untersuchung wird der Standardwert von 300 MeV zu 100 MeV und 500 MeV variiert. Beim Vergleich der Variationen zur Referenz fällt auf, dass sich die Werte für die einzelnen Regionen $\mathcal{A}$, $\mathcal{B}$, $\mathcal{C}$ und $\mathcal{D}$ bis zu 30 % unterscheiden. Der Effekt auf den Wechselwirkungsquerschnitt fällt aber für die meisten Variationen bedeutend geringer aus. Nur die Variation mit einem Schwellenwert von 500 MeV zeigt deutliche Abweichungen. Abgesehen von den Schwellenwerten des Clusterizers wird auch ein weiterer Clusterizeralgorithmus untersucht. Der normale Clusterizer (v1) fügt alle Zellen, die die Mindestenergie erfüllen und aneinandergrenzen, zu einem Cluster zusammen. Dabei kann es vorkommen, dass mehrere Teilchen, die nahe beieinander das Kalorimeter getroffen haben, zu einem Cluster zusammengefügt werden. Dieser Effekt ist im Rahmen der Messung isolierter Photonen gewünscht, da der Hintergrund der Messung aus zusammengefügten Clustern von Photonen aus Zerfällen besteht und dieser so mithilfe der $\mathcal{ABCD}$-

Mehtode bestimmt werden kann. In einem alternativen Ansatz wird stattdessen ein Clusterizer (v2) genutzt, der während der Clustererzeugung Cluster mit mehr als einem lokalen Maximum aufteilt. Dadurch ist es nicht mehr möglich, zusammengefügte Cluster an Hand ihrer Form zu identifizieren, dafür befindet sich aber zusätzliche Energie im Isolationsbereich, wodurch die zweite Annahme der $\mathcal{ABCD}$-Methode nicht mehr zutrifft. Durch die geänderte Vorraussetzungen des v2 Clusterizers lässt sich eine alternative Annahme formulieren: Die Clusterform ist unabhängig von der Energie im Isolationsbereich. Mit der geänderten Annahme lässt sich die $\mathcal{ABCD}$-Methode auch mit dem v2-Clusterizer nutzen. Ein Vergleich des Wechselwirkungsquerschnitts für beide Clusterizer zeigt eine Übereinstimmung innerhalb der statistischen Unsicherheiten. Die Variationen des Clusterizers erzeugen konsistente Ergebnisse und zeigen dabei die Robustheit der $\mathcal{ABCD}$-Methode.

Die beiden in dieser Arbeit durchgeführten Analysen verdeutlichen das Zusammenspiel von verschiedenen Kollisionssystemen bei der Erforschung des QGPs. Die in der $\langle p_{\mathrm{T}} \rangle$ Analyse gewonnenen Ergebnisse erlauben gemeinsam mit den Ergebnissen von pp und p–Pb Kollisionen einen Vergleich von der Multiplizitätsabhängigkeit von $\langle p_{\mathrm{T}} \rangle$. Die dabei beobachteten Unterschiede zeigen, dass unterschiedliche Prozesse in den verschiedenen Kollisionen ablaufen. Die Multiplizitätsabhängigkeit wird sowohl von thermischen Prozessen bei der Entstehung eines QGPs beeinflusst, wie auch von den Eigenschaften von diesem. Weitergehend können durch Modellvergleiche Erkenntnisse über die ablaufenden Prozesse gewonnen werden. Im Gegensatz zur $\langle p_{\mathrm{T}} \rangle$ Analyse befindet sich die Analyse isolierter Photonen in einem früheren Stadium. Dabei werden pp Kollisionen genutzt, um eine neue Analyse zu entwickeln. Die dabei gewonnen Ergebnisse können nicht nur als Referenz für spätere Messungen in Schwerionenkollisionen genutzt werden, sondern tragen für sich genommen zu anderen Themen der Teilchenphysik bei. So sind die Wechselwirkungsquerschnitte isolierter Photonen sowohl für die Bestimmung der PDF von Gluonen in Protonen von Bedeutung, als auch bieten sie einen weiteren Test für pertubative QCD Berechnungen. Für beide Analysen gibt es noch Möglichkeiten für zukünftige Messungen. Weitere Datensätze ermöglichen die $\langle p_{\mathrm{T}} \rangle$ Analyse über einen größeren Multiplizitätsbereich bei pp und p–Pb Kollisionen, bei sehr ähnlichen Schwerpuntksenergien der Kollisionssyteme und die Studie von Xe–Xe Kollisionen. Die Nutzung weiterer Datensätze für die Messung isolierter Photonen ermöglicht einerseits die Studie von p–Pb und Pb–Pb Kollisionen und den sich daraus ergebenden Vergleich, wie auch die Messung bei höheren Schwerpunktsenergien um den x_{T}-Bereich noch weiter

zu niedrigeren Werten zu erweitern. Auch ist es möglich, Korrelationsmessungen mit Teilchenschauern oder einzelnen Hadronen durchzuführen. Die Korrelationsmessungen zeichnen sich besonders durch die Messung der Energie der initialen Wechselwirkung durch das Photon aus. Dadurch ist es möglich, sowohl den Energieverlust des korrelierten Partons, wie auch die Ausbreitung des Schauers im Medium und somit die Eigenschaften des QGPs genauer zu bestimmen.

Contents

Theoretical Introduction 1

Since the discovery of the atomic sub-structure by Rutherford [Rut|11] many theories and experiments [Cha|32, Zwe|64, GM|64, BF^+|69, B^+|69, PLUTO|78, PLUTO|79] revealed the structure of nucleons and the constituents of matter. All those discoveries lead to the Standard Model of Particle Physics, which describes the elementary particles and their interactions. This chapter introduces the Standard Model of Particle Physics with a focus on the strong force, described by quantum chromodynamics (QCD), and the QCD phase diagram. The phase diagram includes a state of deconfined matter, the Quark-Gluon Plasma (QGP). Thereafter the physics and processes in heavy-ion collisions are discussed together with experimental signatures of the QGP. A more detailed description, including a summary of previous measurements, of the two topics of the thesis, the average transverse momentum of charged particles and isolated photons as probes of high-energy particle collisions, closes the chapter.

1.1 Standard Model of Particle Physics

The Standard Model of Particle Physics describes the fundamental constituents of matter and their interactions, except of gravitation. The constituents can be classified by their spin into bosons and fermions. Bosons have an integer spin, while fermions carry a half-integer spin. Fermions can be further subdivided regarding their colour charge (the charge of the strong force) into quarks which carry a colour charge and leptons that carry no colour charge. Each quark carries a colour charge and an electric charge of -1/3 (down, strange, beauty) or 2/3 (up, charm, top) depending on the particle type. Leptons either have an electric charge of -1 (electron, muon, tau) or 0 (electron neutrino, muon neutrino, tau neutrino). For every fermion, an anti-particle with opposite properties exists.

The four fundamental forces are mediated by the corresponding bosons. They differ in their strength, range and the particles they interact with. The weak interaction is limited to fermions, whereas the strong force and the electromagnetic force only interact with particles carrying the appropriate charge. The colour charge has

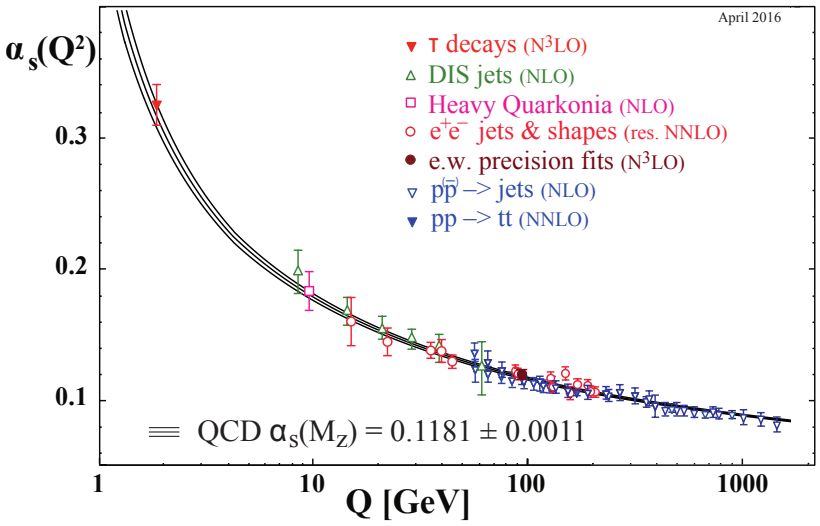

Figure 1.1: Collection of α_s measurements, from multiple experiments and physics processes [PDG|16].

three colours (red, green and blue) and associated anti-colours (anti-red, anti-green and anti-blue). Gluons as bosons of the strong force carry one colour and one anti-colour. The last boson and particle missing in the Standard Model of Particle Physics was the Higgs boson discovered with the LHC in 2012 [ATLAS|12, CMS|12a]. The strength of the forces is described by the coupling constant α_x[1] and depends on the energy of the interaction[2]. In most cases the running coupling is negligible as it only plays a role at very large energies. In figure 1.1 the dependency of the coupling strength as function of the momentum scale Q for α_s is shown. From all coupling constants α_s has the largest energy dependency of the coupling constants. α_s can be described in the following way (for a derivation see [Gri|08]):

$$\alpha_s\left(|Q^2|\right) \approx \frac{12\pi}{(11n - 2N_f) \cdot \ln\left(Q^2/\Lambda^2_{QCD}\right)} \quad \left(|Q^2| \gg \Lambda^2\right) \quad (1.1)$$

Where n and N_f represent the number of colours and flavours, respectively. Λ^2_{QCD} stands for the QCD scale parameter, which describes the energetic limit for pertubative QCD (pQCD). Due to the small energy dependence of α_s at high Q, QCD can be computed with a pertubative approach in the high-energetic regime.

While quantum electrodynamics has a $1/r$ potential, the QCD potential $V_s(r)$ is more complex and can be approximated phenomenologically as:

$$V_s(r) = -\frac{4 \cdot \alpha_s}{3 \cdot r} + F_0 \cdot r \quad (1.2)$$

1: The x defines the nature of the force, i.e. s for the strong forces. α without an identifier commonly corresponds to the electromagnetic coupling constant.

2: This behaviour is known as running coupling.

This potential results in a versatile behaviour of quarks and gluons. In contrast to leptons they cannot be observed as free particles but only as bound states in hadrons. This effect is known as quark confinement. Hadrons consist either of a quark anti-quark pair (meson) or of three (anti-)quarks (baryon) and in sum are always colour-neutral. The majority of hadrons decay by strong or weak interactions into lighter hadrons, leptons, or bosons. The only stable hadrons are neutrons bound in nuclei and protons.

Phenomenologically, the confinement results from the second term in equation 1.2, as the first term is negligible due to the $1/r$ dependency at large distances. With increasing distance r the potential is increasing and thus the potential energy. A new quark anti-quark pair is created once the potential energy exceeds the required energy to create a new quark anti-quark pair. While at large distances the QCD potential gets larger, the opposite effect, known as asymptotic freedom, occurs at very small distances. Accordingly, quarks and gluons interact only weakly over short distances. As constituents of hadrons, quarks and gluons are also referred as partons. Each parton carries a fraction of the total momentum of the nucleon. The parton distribution functon (PDF) describes the probability of finding a parton with the momentum fraction x at a certain energy scale. The energy scale refers to the energy of the probing particle.

1.2 Quark-Gluon Plasma

Cabibbo and Parisi [CP|75] first predicted a state of matter where quarks and gluons are not confined in a large volume. The prediction included the first sketch of a QCD phase diagram (see figure 1.2). The two observables in this diagram are the temperature T and the baryon number density ρ_B. Under common conditions, low T and low ρ_B, the matter exists in a confined state (I). If the temperature and/or the baryon number density is increased a deconfined state is created (II). The phase of deconfined matter is known as Quark-Gluon Plasma (QGP). This happens if V_s gets small enough, due to the small distances (large ρ_B) or the large momentum transfer between the particles (high T).

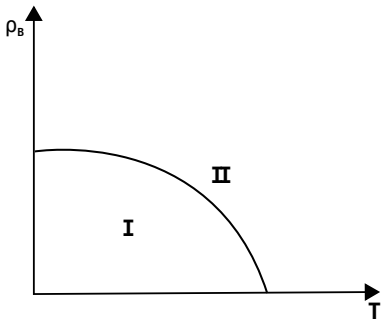

Figure 1.2: First proposal of the QCD phase diagram derived from [CP|75]

By our current understanding in nature, a QGP may exist inside neutron stars and has been created shortly after the Big Bang. On earth, the necessary temperatures and pressure to form such a state can be achieved in heavy-ion collisions. Additionally, it is nowadays possible to calculate the properties of QCD matter in lattice calculations [Phi|13]. Through these calculations our knowledge about

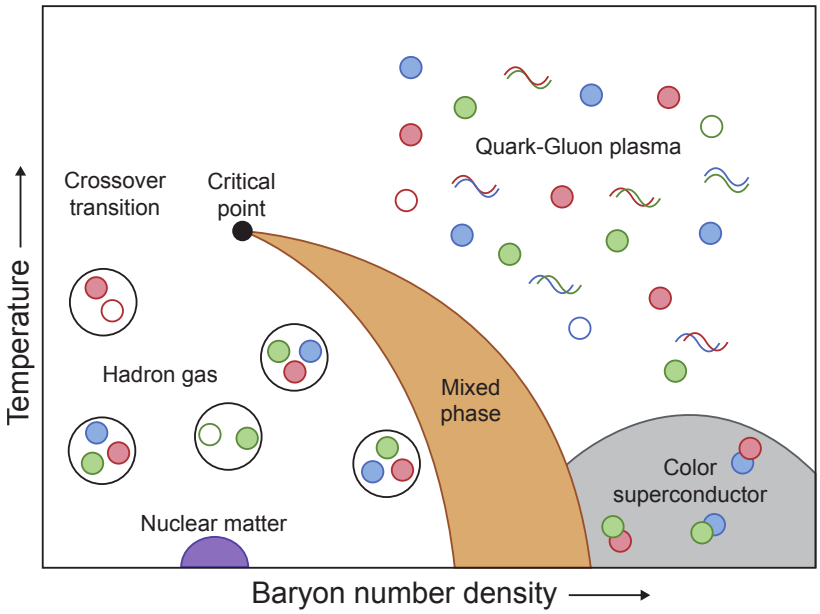

Figure 1.3: Sketch of the QCD phase diagram with known predicted effects and phases [Boo|15].

the QCD phase diagram and the QGP has been developed further. Thus the phase diagrams include more predictions about the QCD at extreme conditions, as seen in figure 1.3. It now contains different states for large T and ρ_B, a possible critical point, as well as different phase transitions.

1.3 Heavy-Ion Collisions

To study the QGP experimentally, heavy-ions are collided with the help of particle accelerators at different energies. During the initial phase of heavy-ion collisions hard scattering processes between single partons take place. In these interactions, heavy-quarks, prompt photons, or other particles with a high transverse momentum (p_T) are created. After this, further interactions between the partons in the overlapping region of the nuclei take place. This interaction volume is referred to as fireball. Depending on the overlap during this phase, nucleons can be divided into participants and spectators. Participants interact with nucleons from the other nuclei during the collision, while spectators do not take part in the interactions and just pass by the collision region. Apart from the overlap, the numbers of the participants and spectators also depend on fluctuations of the nucleon distribution inside the nuclei, as shown in figure 1.4. The nucleons are not uniformly distributed within the nuclei, resulting in differences in the number of participants and spectators at the same overlap. These distributions can be modelled by Glauber Monte Carlo simulations [MR$^+$|07]. The overlap also defines the volume of the interaction region and can be

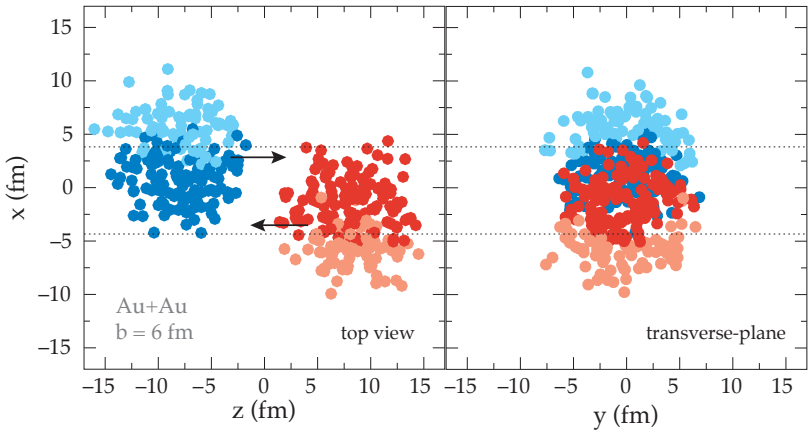

Figure 1.4: Parton distribution of two colliding gold nuclei with differentiation into participants and spectators and a non-uniform nucleon distribution [Kar|15], adapted from [MR+|07].

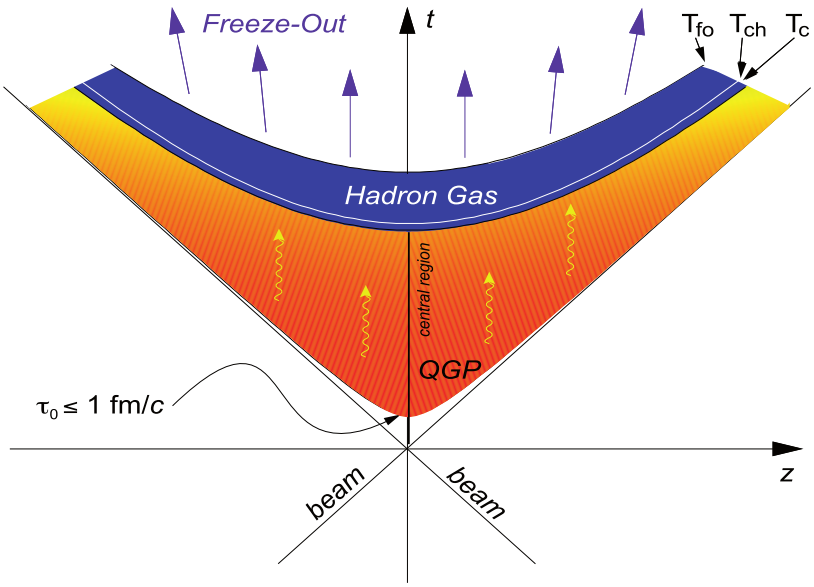

Figure 1.5: Time and space evolution of a heavy-ion collision [KS+|10]

correlated with the hadron rapidity density $\mathrm{d}N/\mathrm{d}y$. This correlation is used for the centrality determination. The centrality defines the percentile of events with a larger overlap [3]. Through the various parton interactions the temperature inside this region increases. If it exceeds the critical temperature T_c, a QGP is formed [CP|75]. The evolution of the initial collision phase and the QGP is shown in figure 1.5. Due to initial fluctuations of the parton distribution in the collision, the fireball is not in a thermal equilibrium and needs less then a few fm/c to reach it. While the hot volume expands adiabatically, the temperature decreases. When the temperature falls below $T_{ch} \approx 160\,\mathrm{MeV}$, the chemical freeze out starts and the partons recombine to hadrons. After this recombination kinematic interactions continue, but the quark content of the hadrons does not change any more. If the temperature falls further below the kinetic freeze-out temperature T_{fo}, no further interactions between the produced hadrons take place.

3: The centrality interval between 0 % to 5 % corresponds to the most central collisions, while the interval of 90 % to 100 % represents the most peripheral ones.

1.4 QGP signatures

To identify the QGP inside a fireball it is necessary to recognize the signals related to a deconfined state. During the short time of a heavy-ion collision, many reactions and processes take place. Possible signatures of a QGP are superimposed by final state particles created by the underlying collision and subsequently detected by the experiment. The different signatures are analysed by specialised experiments. As an example WA98 [G+|91] and PHENIX [PHENIX|03] focus on photon production while NA49 [NA35|91] and STAR [STAR|03] concentrate on the identification of charged particles. Due to many different potential signatures of a QGP the measurements result in a complex picture of a QGP. To identify modifications or signals in the results, often a comparison to pp collisions is used. To take the difference in the number of participants into consideration the pp collisions are scaled by a scaling factor extracted from the above mentioned Glauber Monte Carlo simulations. A possible description of the difference between the two collision systems is the nuclear modification factor (R_{AA}). It can be described as the ratio of the yield in heavy-ion collisions (Y_{AA}) to the yield from pp collisions (Y_{pp}) modified by a scaling factor (s):

$$R_{\mathrm{AA}} = \frac{Y_{\mathrm{AA}}}{s \cdot Y_{\mathrm{pp}}} \tag{1.3}$$

The scaling factor depends on the number of participants N_{AA}.

In the following some signatures associated with a QGP are presented. The selection is limited to probes from hard processes in the collision and modifications of the particle kinematics by a phase transition. [4]

4: This selection is chosen to coincide with the measurement of isolated photons and $\langle p_{\mathrm{T}} \rangle$ in this work.

Heavy-quarks: One of the most prominent signatures for a QGP is the suppression of the J/Ψ and Υ mesons, which was predicted by Matsui and Satz [MS|86]. Only the initial collisions have enough energy to produce a pair of heavy-quarks (quarkonia). Depending on their binding energy the quarkonia may get dissolved inside the QGP. If the Debye screening-length λ_{D} inside the plasma is smaller then the bounding radius of the quarkonia, the bound state is broken and the two quarks dissolve inside the plasma. As different states of quarkonia have different bounding radii, their suppression is varying. These variations may reveal information about the QGP temperature. Figure 1.6a shows a stronger suppression for weak bound bottomium states compared to the Υ ground state. At

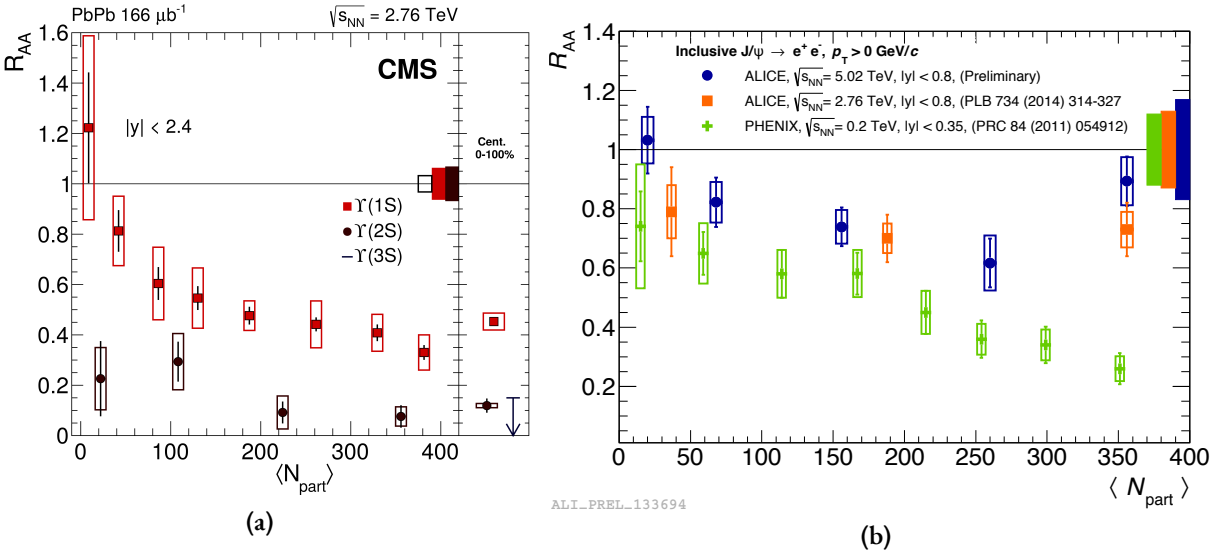

Figure 1.6: Nuclear modification factor R_{AA} for different bottomium (Υ) states (a) [CMS|17] and energy dependence of J/Ψ nuclear modification factor R_{AA} (b) [ALICE|17c].

high energetic heavy-ion collisions like at the LHC the high number of produced J/Ψ can result in an enhanced J/Ψ [ABM$^+$|07]. In figure 1.6b the recombination of J/Ψ for increasing collision energies from RHIC to LHC is shown. For higher energies the suppression also decreases with the increase of the number of participants.

Particle suppression: Similar to quarkonia, partons with a high transverse momentum originate from the initial scatterings of the collision. During their propagation through the fireball these partons or their fragments will interact with other partons. Thus the p_T spectrum of the partons is modified by the medium. The modification depends on the medium properties of the fireball and can be studied in various observables. The nuclear modification factor (R_{AA}) for charged particles depends strongly on the centrality of the collision, as shown in figure 1.7. For central events the particle yield is strongly suppressed while the modification decreases for peripheral collisions. A similar modification can be observed by the per trigger yield I_{AA}, where the angular correlation of particles to an high-energetic trigger particle is analysed. The angular correlation of charged hadrons shows a suppression on the away side in central heavy-ion collisions, as shown in figure 1.8. In contrast, the yield on the near-side of the trigger particle is incremented. For peripheral events only a faint dependency is observed.

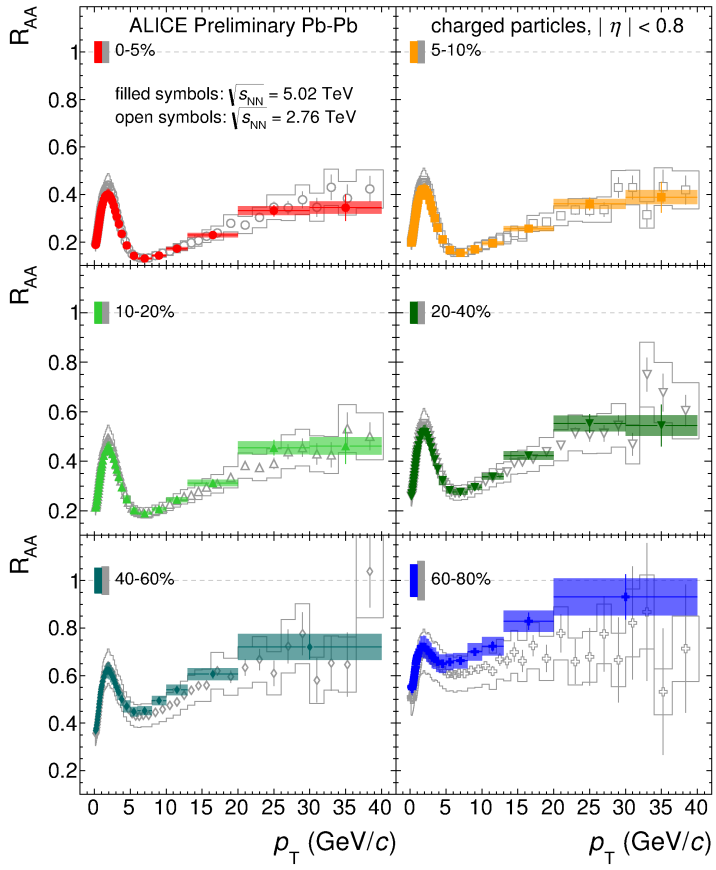

Figure 1.7: Particle spectra modification in Pb–Pb collisions for different centralities at $\sqrt{s_{\mathrm{NN}}} = 2.76$ TeV and 5.02 TeV [ALICE|17d].

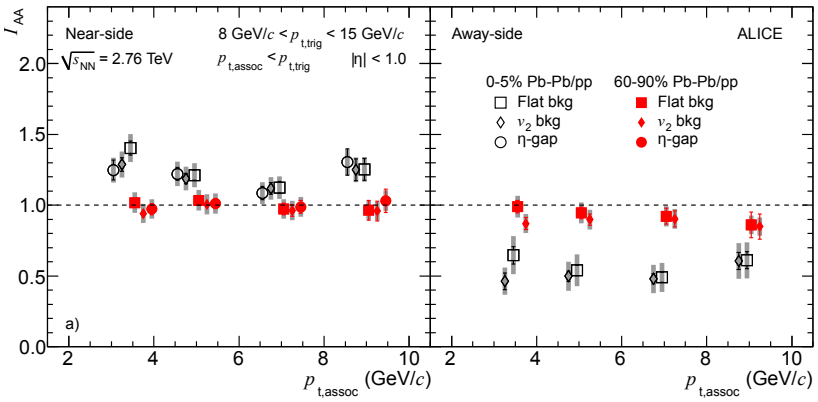

Figure 1.8: Difference of the per trigger yield between near-side (left) and away-side (right) [ALICE|12].

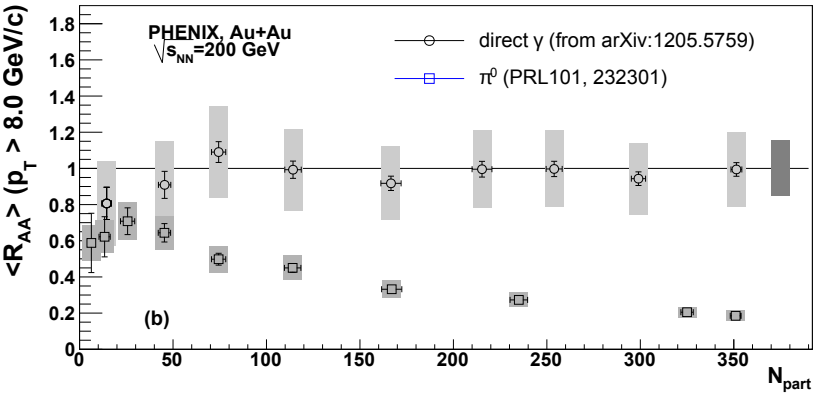

Figure 1.9: Comparison of the nuclear-modification factor of π^0 and direct photons for different collision centralities [PHENIX|13].

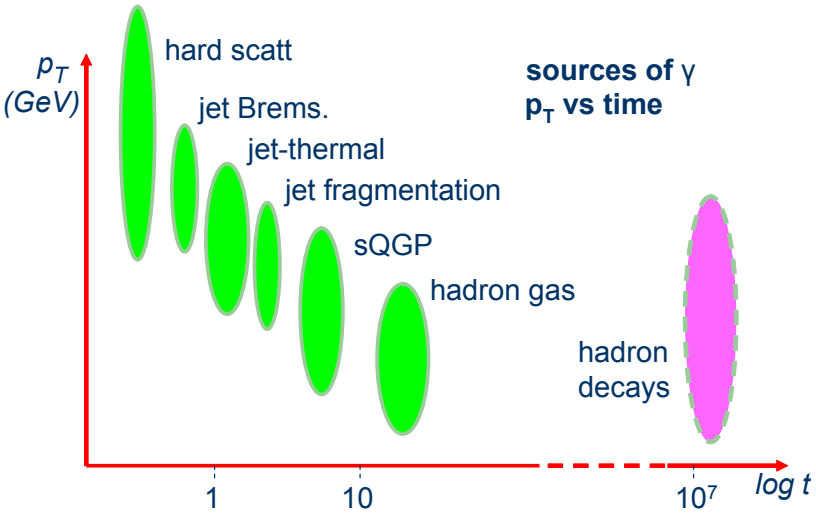

Figure 1.10: Energy and time distribution for γ production mechanisms in heavy-ion collisions [Sak|08].

Electro-magnetic probes: In comparison to most of the other signatures, electro-magnetic particles are not affected by the strong force. As a consequences, electro-magnetic particles can traverse the fireball nearly unaffected (see [Paq|17] for details). This effect can be observed by comparing the nuclear modification factor of photons and π^0, which decay into photons, as shown in figure 1.9. Two kinds of electro-magnetic probes are used to study particle collisions: dileptons and photons. The main source of dileptons is hadronic particle decays. They also provide the possibility to measure the thermal radiation of the QGP. Photons from hadronic decays represent a major process of photon production. Photons who are not produced by a decay process are grouped as direct photons and represent a good probe to study the collision processes and the medium properties. In heavy-ion collisions, they are produced through all stages of the collision. Figure 1.10 provides a sketch of the different photon production processes, their production time, and their p_T spread. Prompt photons are produced in the early stages of a collision. They allow to study the scaling of binary collisions compared to pp collisions, and if tagged with a jet provide an excellent probe to study in medium modifications. An

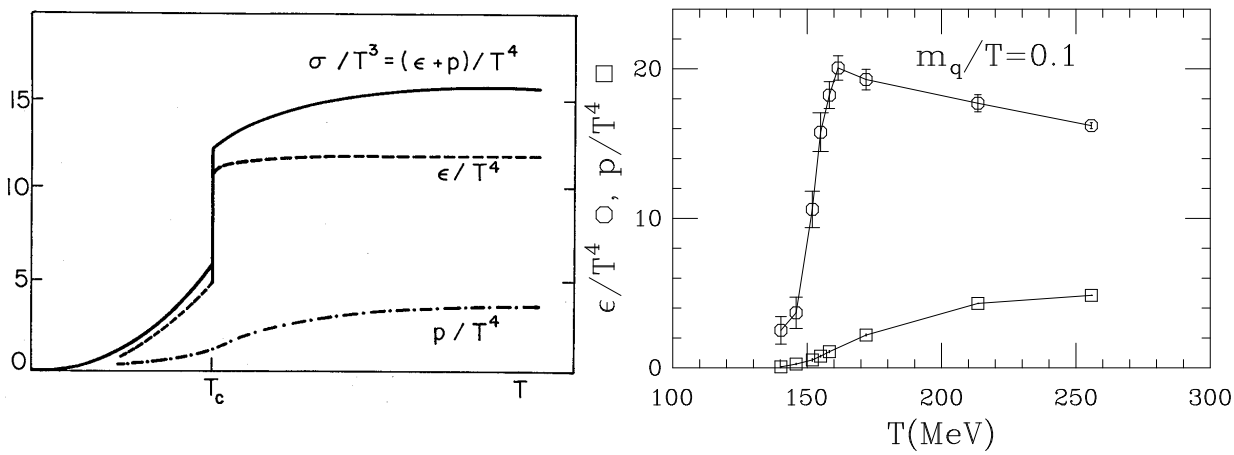

(a) [VH|82] **(b)** [BK⁺|95, HM|96]

Figure 1.11: Behaviour of energy density ϵ (dashed line/circles), pressure p (dash-dot line/squares) and entropy density (solid line) as function of the medium temperature T, for a thermodynamic prediction (a) and a lattice calculation (b).

additional source of photons is the thermal radiation of the QGP and the hadron gas, which provides the possibility to measure the temperature of the medium. Due to the continuous production of thermal photons during the whole evolution of the collision, it is not possible to specify the in-medium temperature accurately. Despite the missing modifications inside the medium the measurements are challenging due to small production cross-sections and large backgrounds from particle decays and jet related photons.

Kinematic observables: Apart from modifications of direct signals a possible phase transition inside the fireball would effect properties of the medium like the energy density ϵ, the pressure p, or the entropy density σ [HM|96]. In figure 1.11 the implications of a possible transition at a critical temperature of 150 MeV are shown. To pronounce the changes both observables are scaled with $1/T^4$. The steep slope arises from the increased number of degrees of freedom in the phase transition. Changes in these fundamental properties would result in a change of different observables of the underlying event like the average transverse momentum $\langle p_T \rangle$, the hadron rapidity density dN/dy, and the transverse energy distribution dE_T/dy.

1.5 Detailed description

1.5.1 Average transverse momentum

The average transverse momentum of charged particles may show signs of a phase transition as predicted by Van Hove [VH|82]. This effect would be visible in the dN/dy dependence of $\langle p_T \rangle$. The multiplicity n can be approximated to be proportional to $\sigma \cdot V$, with σ as entropy density and V as the volume of the collision at a fixed time. For studying the thermodynamic implications on the particle production, in a first step the volume of the fireball is assumed to be constant. With the volume fixed, σ is proportional to n and by increasing n also σ and accordingly the temperature T rises. The rise of T induces an increase of $\langle p_T \rangle$. Once the T has reached the critical temperature T_c, σ rises further but T stays constant, as visible in figure 1.11a. $\langle p_T \rangle$ stays constant or may decrease as $p/(T\sigma)$ decreases in a phase transition. For multiplicities above the phase transition, the temperature and $\langle p_T \rangle$ inside the fireball increase as before the phase transition. This increase will have a smaller slope, because the particles created in the collision freeze-out at T_{fo}. Taking all three phases into account, the phase transition should be visible in a s shaped gradient as shown by the dashed line in figure 1.12. For inclusive centrality the effect would be washed out, due to mixing of different collision volumes. Anyhow a shoulder in the $\langle p_T \rangle$ vs. dn/dy correlation should be still visible as indicated by the solid line.

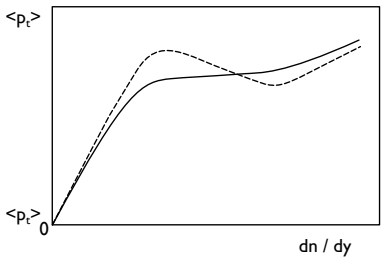

Figure 1.12: Prediction of $\langle p_T \rangle$ development for a phase transition by [VH|82]. The solid line shows the gradient for all events, while the dashed lined shows the behaviour for a fixed impact parameter.

The $\langle p_T \rangle$ of charged particle production was measured over a wide energy range in the past decades. Most measurements were performed in light collision systems like pp, K^+p and π^+p, but also some measurements for heavy-ion collisions exist. Figure 1.13a summarizes measurements from 5.6 GeV/c to 1.8 TeV/c for light collision systems. At low multiplicities all measurements show a rising $\langle p_T \rangle$ with increasing multiplicity. For higher multiplicities the trend depends on the collision energy. The energy of low energetic collisions is not sufficient to boost the momentum of the produced particles in high multiplicity events. Thus the $\langle p_T \rangle$ drops with the increasing multiplicity. The slope of the decline, decreases with increasing collision energy. From a collision energy of $\sqrt{s} = 63$ GeV onwards the $\langle p_T \rangle$ shows a positive correlation with multiplicity. This increase is larger for higher energies, but also shows a flattening for highest multiplicities.

For heavy-ion collisions, CMS and STAR published results for different collision energies [CMS|13]. A compilation of these results is

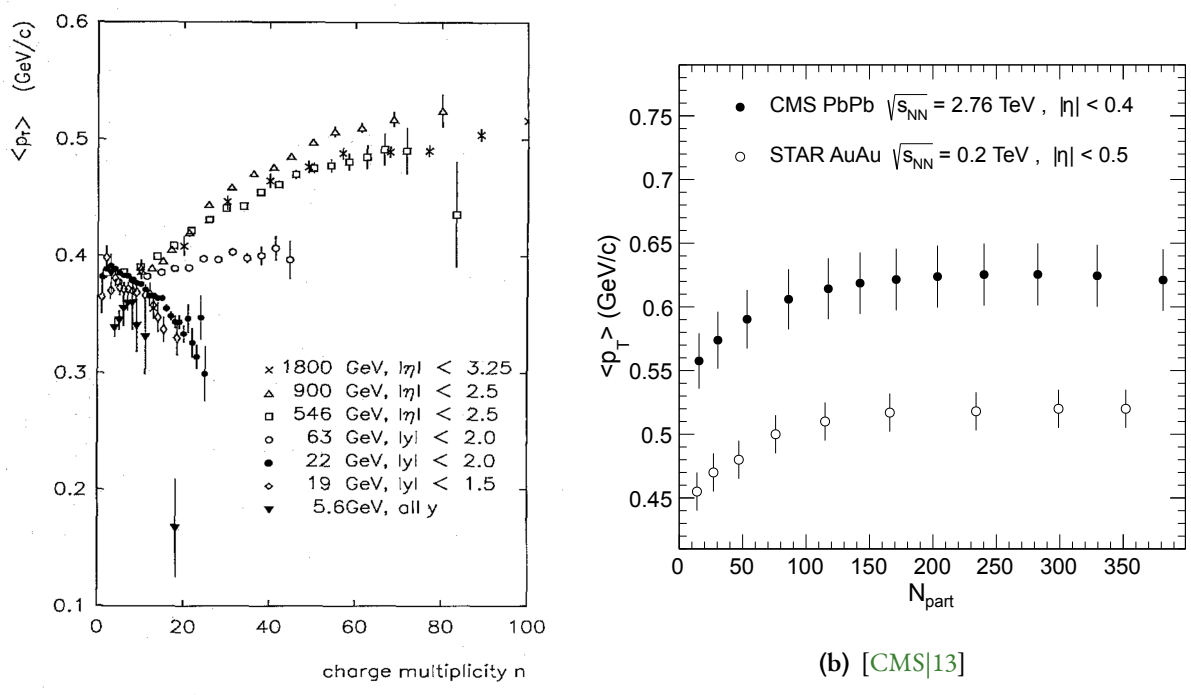

(a) [EHS/NA22|88] **(b)** [CMS|13]

Figure 1.13: Behaviour of average p_T against multiplicity for different energies in light collision systems (a) and in heavy-ion collisions (b).

shown in figure 1.13b. Even though the collision energies differ by one order of magnitude, $\langle p_T \rangle$ only differs by 100 MeV. Both results show a very similar behaviour with an increase of $\langle p_T \rangle$ for peripheral collisions. This rise of $\langle p_T \rangle$ decreases for semi-central events and disappears for central events.

Due to the different experimental properties it is not possible to properly compare the $\langle p_T \rangle$ behaviour between pp collisions and heavy-ion collisions with the existing data.

1.5.2 Isolated photons

As mentioned before, prompt photons are produced in the initial scattering processes of a particle collision. They can be either created by quark-gluon scattering and quark anti-quark annihilation in the scattering process or radiated in a jet (fragmentation, bremsstrahlung) originating from the scattering. [5] This classification of prompt photons may be precise from the theoretical point of view, but does not provide a clean criterion to distinguish the photons experimentally. To achieve such a differentiation a measurable criterion is required. By applying an isolation criterion to prompt photons, the contributions from fragmentation photons

5: For a better differentiation of the processes, in the following photons produced directly in the initial scattering are referenced as photons from $2 \rightarrow 2$ processes.

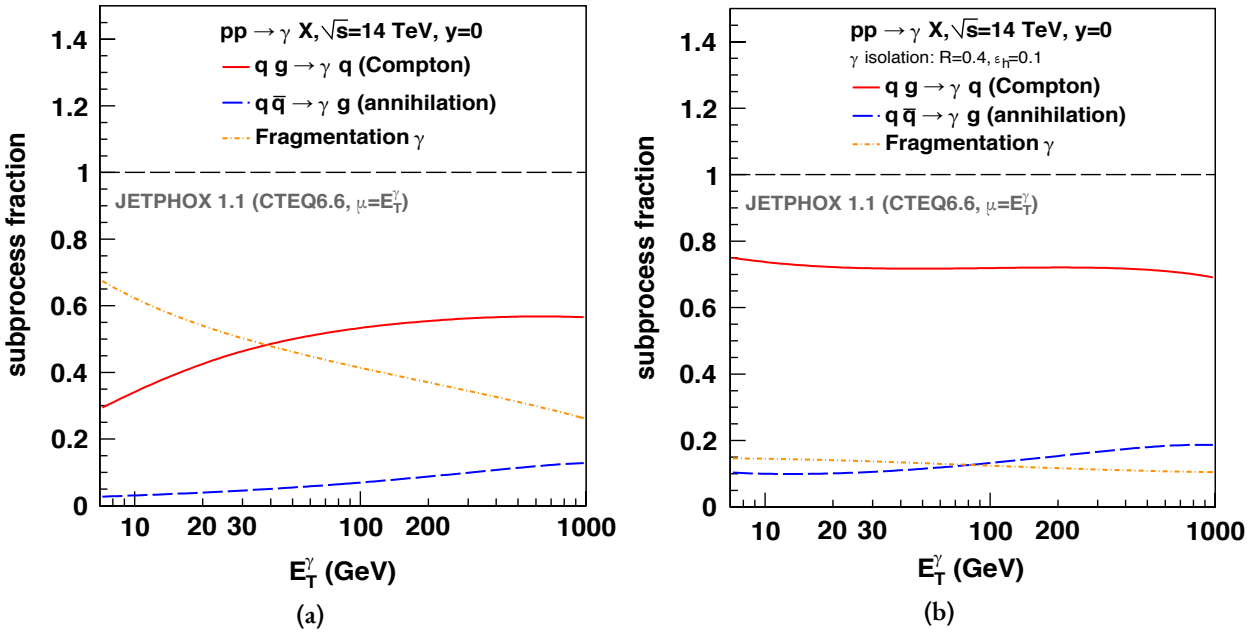

Figure 1.14: Distribution of prompt photons without (a) and with (b) an isolation cut [Id|10].

are significantly reduced, while it has only a small effect on photons from $2 \rightarrow 2$ processes, as shown in figure 1.14.

The results of isolated photon spectra provide a test case for pQCD calculations. The spectra also can contribute to measurements of parton distribution functions (PDF) [AB$^+$|89]. Especially, the gluon distribution can be probed with photons from $2 \rightarrow 2$ processes. Pairs of isolated photons are also produced by certain particle decays. In the search and study of the Higgs Boson a pair of isolated photons is used to probe the $H \rightarrow \gamma + \gamma$ decay channel [D0|09, CDF|09, ATLAS|11b, CMS|12b].

Isolated photons are measured over a wide range of collision energies and collision systems. A compilation of isolated photon E_T spectra from pp and $p\overline{p}$ collisions is performed in [dR|12]. The compilation contains data from collision energies between $\sqrt{s} = 200\,\text{GeV}$ and $\sqrt{s} = 7\,\text{TeV}$ and multiple experiments. The results are compared to different theoretical models and used to constrain parameters in PDF calculations. Figure 1.15 shows the comparison of the spectra against two different variables: E_T in figure 1.15a and the scaling variable $x_T = 2E_T^\gamma/\sqrt{s}$ in figure 1.15b. For the x_T spectra the cross-sections are additionally scaled with a value of $\sqrt{s}^n$, where exponent n equals 4.5. For E_T, all measurements show a power law behaviour and cover photon energies between 3 GeV and 400 GeV. The cross-section expands over 9 orders of magnitude. In the x_T spectrum all measurements line up on top of each other with deviations for non-midrapidity measurements. The existing LHC meas-

urements provide results for the smallest x_T values, where the lowest bin ranges from 15 to 20 GeV [ATLAS|11a]. With a lower photon-energy reach, it would be possible to extend the x_T spectrum further down and also provide new information for gluon PDFs.

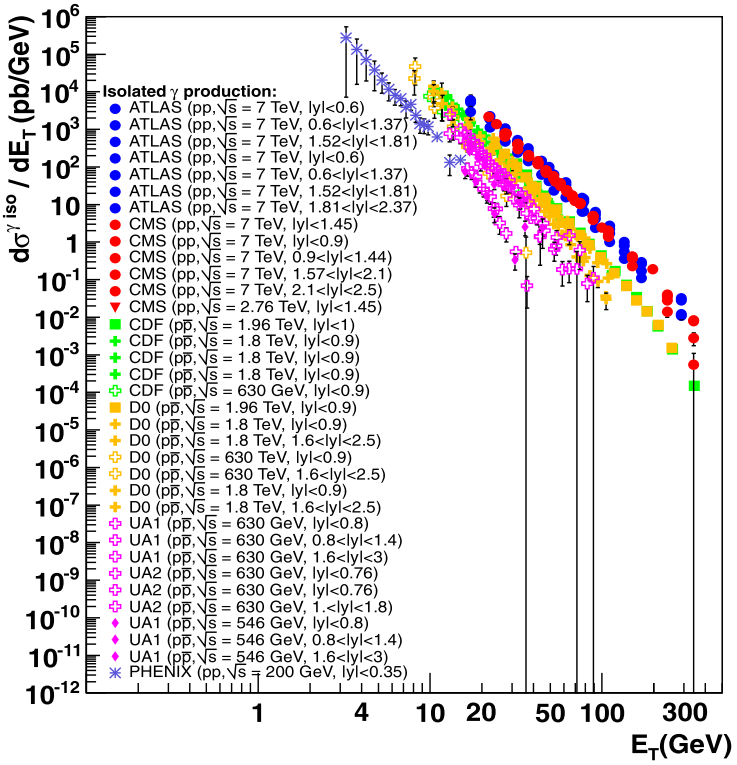

(a)

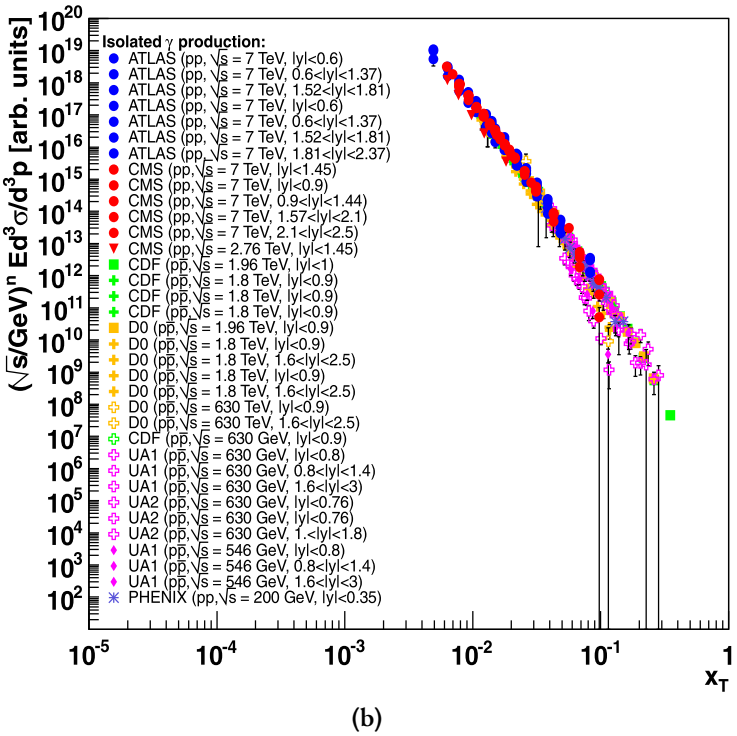

(b)

Figure 1.15: Isolated photon cross-section in pp and $p\bar{p}$ collisions (a) and the corresponding x_T values (b) from different experiments and collision energies [dR|12].

Experimental Setup 2

In the following, an introduction to the accelerator systems and the experiments of the LHC will be given. Afterwards, a more detailed view on ALICE experiment and its detectors will be given. A special focus will be on the detectors relevant for the analyses performed in this work. The chapter closes with a description of the analysis-relevant software components.

The European particle physics laboratory CERN[1] is one of the leading accelerator facilities in the world, located at the Swiss-French border near Geneva. It operates many different particle accelerators (Fig. 2.1), which are used for a wide range of research topics. With a circumference of nearly 27 km the Large Hadron Collider (LHC) is the largest and most powerful accelerator at CERN. The six experiments located at the LHC cover different research topics. Two small experiments, TOTEM[2] and LHCf[3], measure particles in the very forward region and are placed close to CMS [4] and ATLAS [5], respectively. TOTEM focuses on precision measurements of proton properties and LHCf reproduce and study properties of cosmic rays. ATLAS and CMS are general purpose experiments with an emphasis on high-energy particle physics, while the key aspects of LHCb[6] are precision measurements of CP violation and rare b-decays. ALICE as a dedicated heavy-ion experiment is the newest in a long history of experiments at CERN which focus on the discovery and measurement of the QGP, for instance NA45, NA49, NA61, WA80, and WA98.

1: Conseil Européen pour la Recherche Nucléaire

2: TOTal, Elastic and diffractive cross-section Measurement

3: Large Hadron Collider forward

4: Compact Muon Solenoid

5: A Toroidal LHC ApparatuS

6: Large Hadron Collider beauty

2.1 LHC

The LHC provides the highest energies of all accelerators at CERN. Apart from the LHC, PS and SPS also provide particle beams to many other experiments at CERN. At their start of operation in 1959 and 1976, respectively, both were the largest accelerators at CERN and opened the door for new physics discoveries [HF$^+$|73, Gargamelle|73, UA1|83b, UA2|83a, UA1|83a, UA2|83b]. To reach the high energies in the LHC many accelerators are linked to an accelerator chain, where the energy of the particles is increased in multiple steps. An ion source is connected to a linear accelerator which splits the continual particle beam into bunches and performs

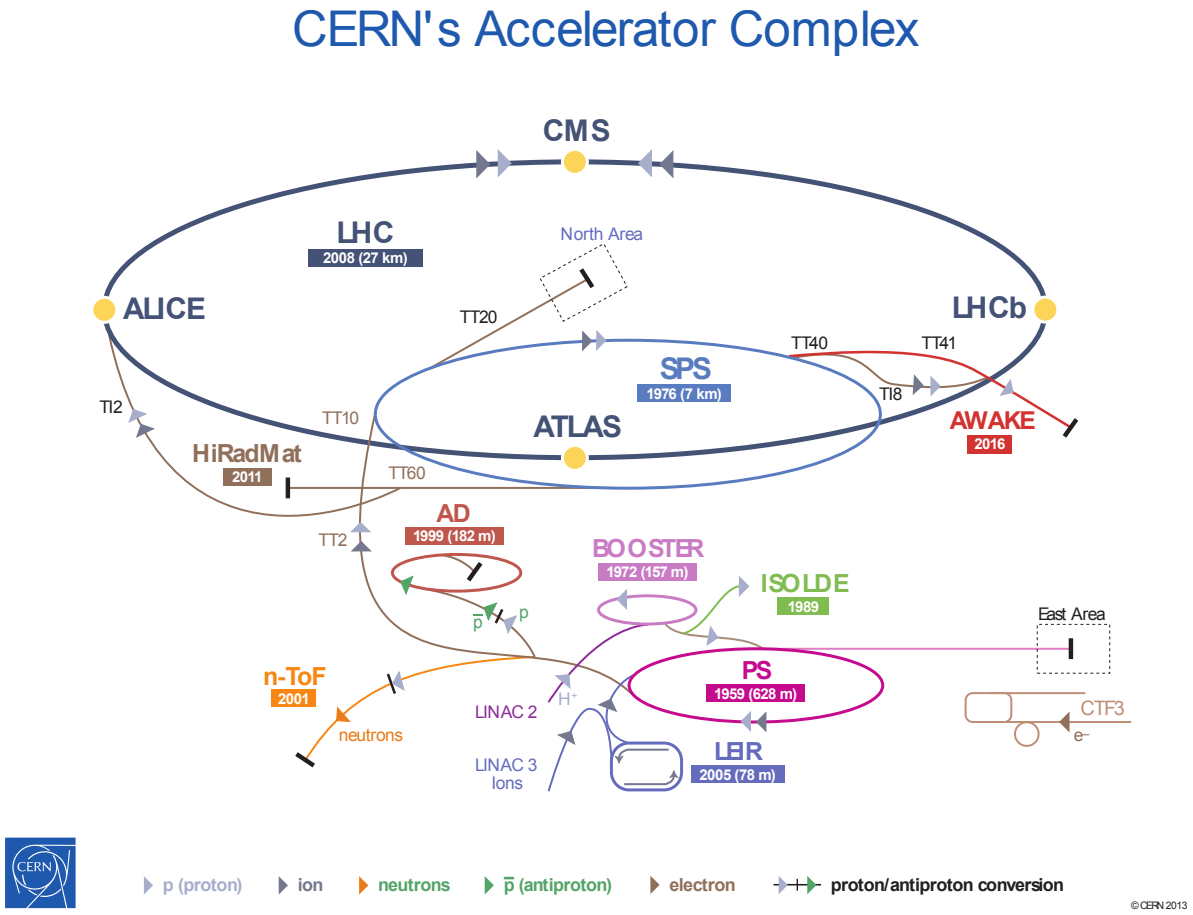

Figure 2.1: Sketch of all accelerators operated in 2016 at CERN with transfer lines and running experiments [DM|16]

a first acceleration. Subsequently, a first ring accelerator further increases the energy of the particles. For protons those two accelerators are LINAC 2 and Booster, while for lead ions the acceleration starts with LINAC 3 and LEIR. Next, the protons as well as the Pb ions are transferred to the Proton Synchrotron (PS) and then the Super Proton Synchrotron (SPS), which is the last pre-accelerator before the LHC.

The LHC first stores the bunches injected from SPS. To achieve a high luminosity, this process is repeated multiple times until the intended number of bunches is stored. As shown in figure 2.2, the LHC consists of two beam pipes, in which particle bunches rotate clockwise / counterclockwise. The LHC is divided into eight sectors, they contain different parts of the synchrotron infrastructure as the acceleration system or the beam dump. In four sectors, the two beam pipes cross each other. At these crossing points the particle collisions take place and the four large experiments are placed. To keep the beams on the circular trajectory, the beam pipes are placed inside superconducting dipole magnets with magnetic fields up to 8.4 T. The LHC accelerates the protons from an in-

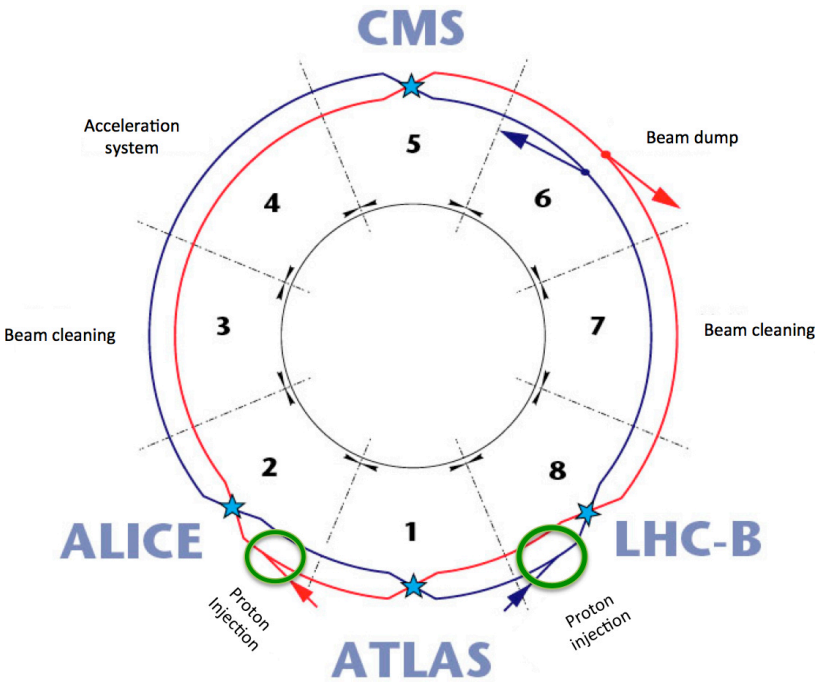

Figure 2.2: Divison of LHC in sectors, with position of interaction points (experiments) and injection points [Ros|14]

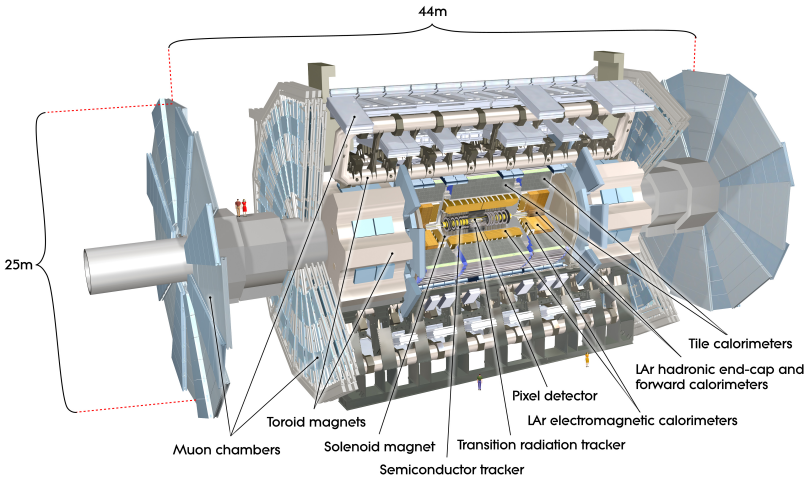

Figure 2.3: The ATLAS detector [ATLAS|08]

jection energy of 450 GeV to a maximum of 6.5 TeV. After the designated energy is reached, the particle beams are collided in the crossing points. The collisions are performed for many hours until the beam intensities have decreased and the beams are dumped.

2.1.1 ATLAS

ATLAS [ATLAS|08] is the largest of the LHC experiments. It has been designed as a multi-purpose experiment and focuses on the detection and precise measurement of high energetic particles expected from the decay of the Higgs bosons and physics Beyond the Standard Model (BSM). This is achieved by the usage of 3 magnets and

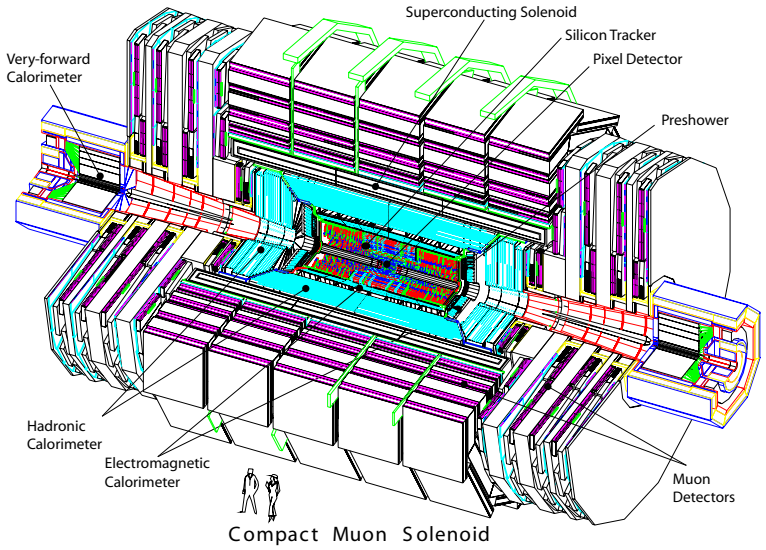

Figure 2.4: CMS experiment [CMS|08]

6 different sub-detectors. Close to the collision point, a solenoid produces a magnetic field of 2 T. Inside of the solenoid, the three innermost detectors are placed. The pixel detector and the semiconductor tracker both use silicon detectors for vertex reconstruction, tracking and momentum measurement of charged particles. The transition radiation tracker additionally can discriminate between electrons and pions. Outside of the solenoid, two toroids create a field of 4 T [ATLAS|05]. Between the magnets an electromagnetic and a hadronic calorimeter are placed. Parts of the muon spectrometer are embedded into the toroids, while other parts are placed outside the magnets. The acceptance of the tracking system and the calorimeters are $|\eta| < 2.5$ and $|\eta| < 3.2$, respectively.

2.1.2 CMS

CMS [CMS|08] has the same physics goals as ATLAS. Hence both detectors can confirm the results of each other and thus provide an important cross-check for new discoveries. The innermost part comprises of silicon pixel and micostrip detectors, organised in 13 layers. They provide a high accuracy tracking capability. Surrounding the tracking detectors, an electromagnetic calorimeter with leadtungstate crystals allows for the energy measurement of photons and electrons. The energy of hadronic particles can be measured by the next outward detector, the hadronic calorimeter. All those detectors are positioned inside a superconducting magnet, which delivers a field of 4 T. The outermost part is the muon system. Its detection layers are placed in alternating order with the iron yoke of the magnet. The coverage for the different detectors are $|\eta| < 2.5$ for the

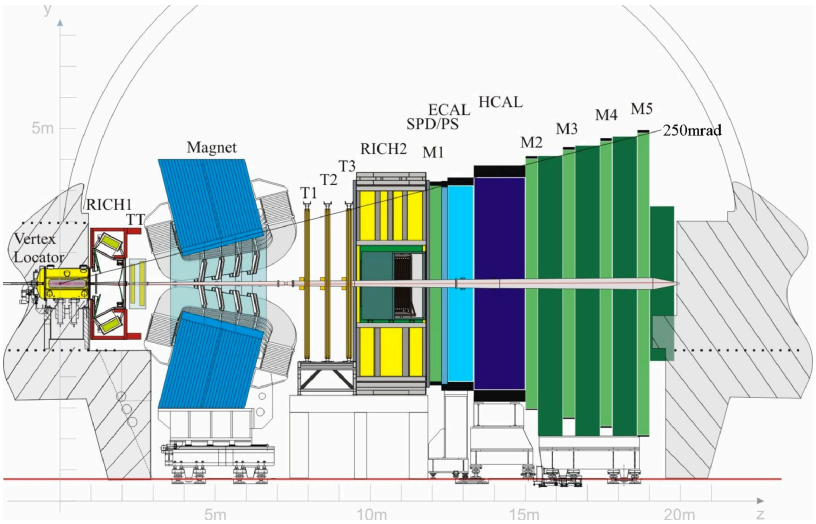

Figure 2.5: Detector layout of LHCb [LHCb|08]

tracking system, $|\eta| < 3$ for the calorimeters. The hadronic calorimeter extends this coverage with a dedicated forward calorimeter to $|\eta| < 5.2$

2.1.3 LHCb

LHCb [LHCb|08] focuses on b-physics in order to precisely measure CP violation and searches for hints of BSM physics. At LHC, $b\bar{b}$ pairs are mainly produced via gluon fusion. Because the momenta of the participating gluons are highly asymmetric, the b pairs are boosted in beam direction. This effect also leads to the layout of LHCb, which differs from the other large LHC experiments. As shown in figure 2.5, LHCb is built in forward direction. The vertex locator (VELO), placed around the interaction region, detects the primary as well as secondary vertices and also acts as a first tracking detector. To measure the momenta of charged particles, a dipole magnet is installed further downstream. On both sides, the magnet is enclosed by additional tracking detectors and Ring Imaging Cherenkov (RICH) detectors for particle identification. Subsequently, the calorimeter station follows. It consists of an electromagnetic calorimeter with a pre-shower detector and a hadronic calorimeter. The outermost detector is the muon system. LHCb covers a pseudorapidity range of $1.9 < \eta < 4.9$. To offer studies with different collision systems at LHCb, it has the possibility to inject gas in the interaction region and collect data from beam-gas interactions as a fixed-target experiment.

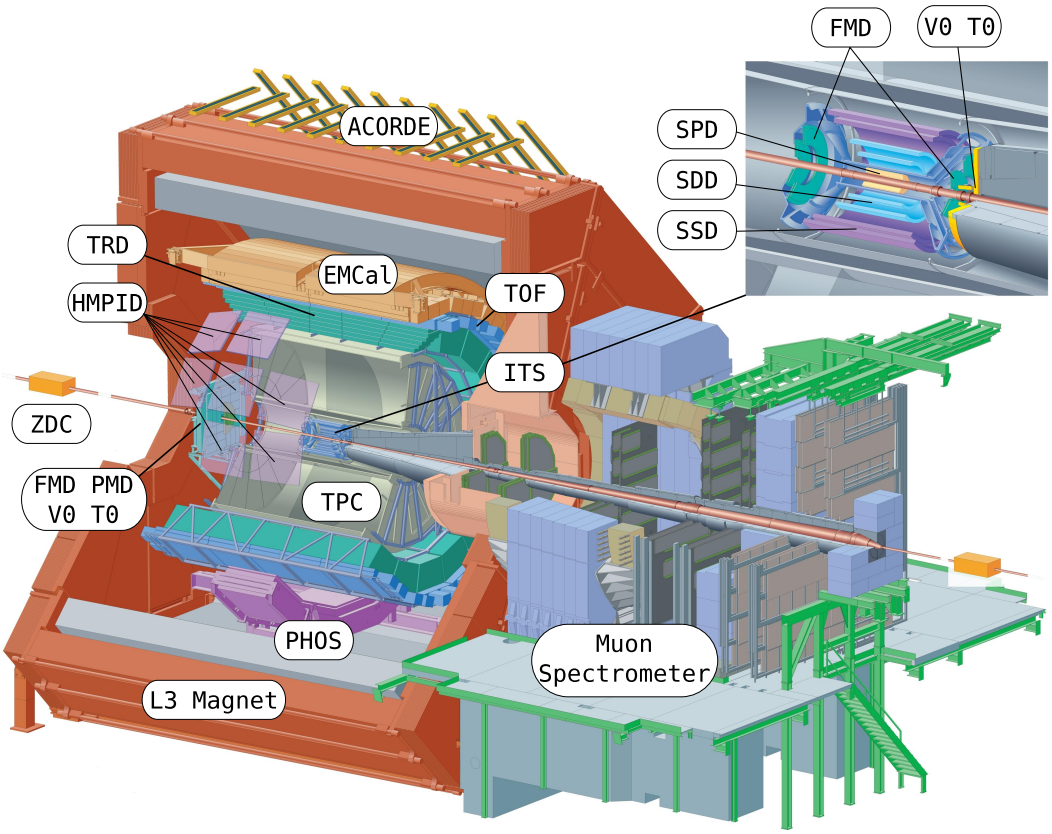

Figure 2.6: Layout of ALICE with locations of all detectors [ALICE|08a]

2.2 ALICE

ALICE primarily investigates the properties of heavy-ion collisions at the LHC and looks for signs of a QGP and the conditions under which it is formed. The layout of the whole experiment is focused on tracking and particle identification (PID) of large quantities of particles, as created in heavy-ion collisions. The detectors of the experiment can be grouped into two categories, forward detectors, these are placed along the beam axis and central detectors which are placed around the collision vertex. Most of the detectors are placed inside a solenoidal magnet, thus the momentum of charged particles can be calculated by the bending radius.

For analysis purposes a right-handed global coordinate system for ALICE is defined as shown in figure 2.7 and described in the following: The x-axis points to the centre of the LHC, the y-axis points upwards and the z-axis is oriented along the beam line in the direction of the ATLAS experiment. The azimuthal angle φ starts at the positive x-axis and rotates mathematically positive in the x-y plane, while the polar angle ϑ starts at the positive z-axis and increases towards the positive y-axis. Instead of the polar angle ϑ the pseudorapidity η is used in analyses.

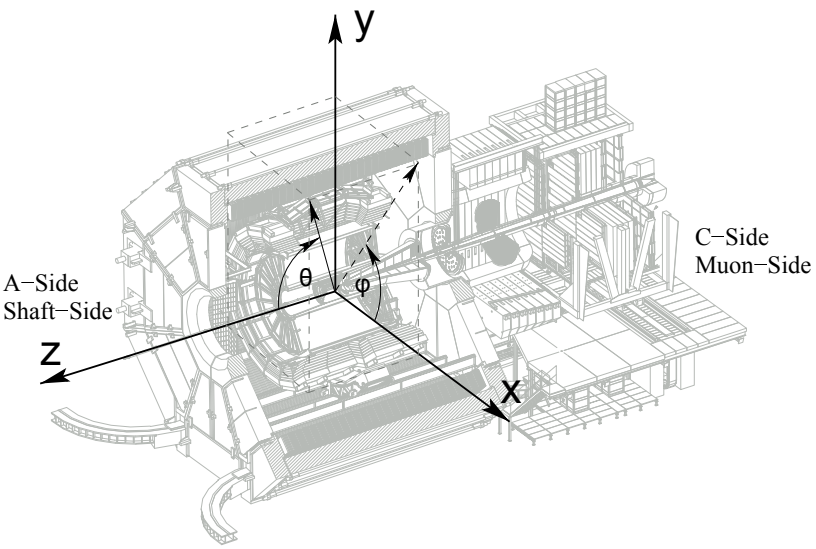

Figure 2.7: Sketch of the setup with the right-handed coordinate system [Wie|08] as described in section 2.2.

2.2.1 Magnet

The magnetic setup of ALICE consists of a magnet for the central part of the experiment and one for the forward part of the experiment. The central detectors are placed inside a normal-conducting solenoid, which was already used by the L3 experiment at LEP and provides a magnetic field of up to 0.5 T. The space inside of the magnet has a diameter of 11.50 m and a length of 12.1 m and accommodates most of the detectors. As part of the muon spectrometer a dipole magnet is placed in forward direction.

2.2.2 Forward Detectors

2.2.2.1 Muon Spectrometer

The muon spectrometer is placed in forward direction (negative z) along the beam axis to measure muons from the decay of heavy-quark mesons. To identify mesons and to reduce the background of the measurement an absorber is positioned between the interaction point and the active components of the detector. Due to their high mass only muons can traverse the absorber without being stopped. The detection of the muons takes place in five tracking stations, of which two are located before, one inside and two after the magnet. Each station is equipped with two layers of pad chambers. This structure in combination with the magnetic field of 0.67 T provides the possibility of measuring the momentum of muons. Additionally, a muon trigger system is positioned behind a second absorber, that stops low energetic muons. Thus, events with muons from

heavy quarks can be pre-selected. The whole device has a coverage of $-4 \leq \eta \leq -2.5$.

2.2.2.2 FMD

The Forward Multiplicity Detector (FMD) measures charged particles in the forward/backward direction. It uses 3 rings of silicon strip detectors to cover $-3.4 \leq \eta \leq -1.7$ and $1.7 \leq \eta \leq 5.0$. With the overlapping coverage of FMD and SPD it is possible to measure the charged particle density over a large pseudorapidity range.

2.2.2.3 PMD

In forward direction it is also possible to measure the multiplicity of photons with the Photon Multiplicity Detector (PMD). For the photon detection a converter is placed between two planes of gas proportional chambers. As photons will leave no signal in the first plane, the electrons and positrons from conversions will leave a signal in the second plane and thus can be identified.

2.2.2.4 T0

The layout of the T0 detector focuses on a fast signal to measure the collision time. For this purpose Cherenkov counters located on both sides of the interaction point are used that cover a pseudorapidity of $-3.28 \leq \eta \leq -2.97$ and $4.61 \leq \eta \leq 4.92$. The time measured by the T0 detector is also used as starting time for the time-of-flight measurement performed by TOF. Additionally, the T0 detector generates a fast trigger signal.

2.2.2.5 V0

The V0 measures the charged particle multiplicity in the forward/-backward direction to provide a multiplicity estimation which is uncorrelated to the track multiplicity measured by the central tracking detectors. The setup of two scintillators is placed on both sides of the interaction point. Every scintillator consists of four rings with different radii and is read out via Wave-Length-Shifting (WLS) fibres. The scintillators cover a range of $2.8 \leq \eta \leq 5.1$ and $-3.7 \leq \eta \leq -1.7$. As the setup delivers a fast multiplicity estimation, the V0 detector is also used in different trigger configurations: The

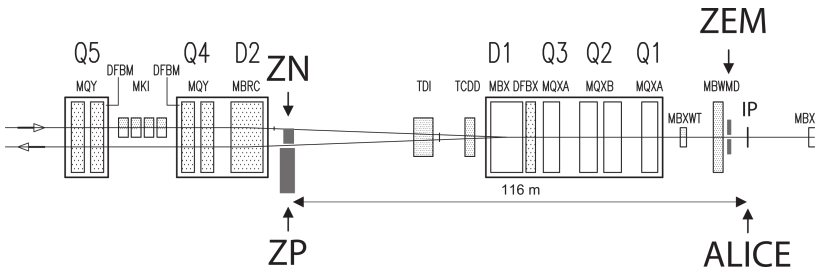

Figure 2.8: One side of the ZDC detector [ALICE|08a]

Minimum Bias trigger, Multiplicity trigger, semi-Central trigger, and Central trigger.

2.2.2.6 ZDC

The Zero-Degree Calorimeter (ZDC) consists of three different sub-detectors to measure the centrality of heavy-ion collisions. Two calorimeter pairs are positioned on both sides of the interaction point in a distance of 116 m, where the two beam lines are focussed to the interaction point. Each pair contains one calorimeter for measuring protons (ZP) and one for measuring neutrons (ZN). The ZP is located outside the beam pipes to detect protons which are deflected by the LHC magnets, while the ZN is placed between the beam-pipes to detect neutrons. These calorimeters measure the number of spectators in heavy-ion collisions but cannot distinguish between central and peripheral collisions as the mass to charge ratio of heavy fragments from peripheral interactions is similar to the ratio of lead. For this purpose a pair of electromagnetic calorimeter (ZEM) is placed 7 m apart from the interaction point opposite the muon arm. They measure the number of charged particles created during the collision in forward direction. By correlating the measurements of the three calorimeters it is possible to provide a centrality measurement for heavy-ion collisions.

The layout of all three calorimeters is very similar. They use an absorber with quartz fibres to detect Cherenkov light of the particle cascade created by the absorbed particles. As absorber material a tungsten alloy, brass and lead are used for ZN, ZP and ZEM, respectively.

2.2.3 Central Barrel Detectors

2.2.3.1 ITS

In total, the Inner Tracking System (ITS) comprises of six layers of silicon detectors and represents one of the major tracking devices in

ALICE. The layers are grouped pairwise and their names refer to the silicon technology used. The two innermost layers are made of Silicon Pixel Detectors (SPD) and use a digital readout. Their coverage of $|\eta| < 1.98$ overlaps with the FMD and they provide a vertex resolution of 100 μm. The outer four layers are capable to measure the specific energy loss ($d\mathrm{E}/d\mathrm{x}$) and thus provide information about the particle species. The four layers differ by the used silicon chips. While the two middle layers use Silicon Drift Detectors (SDD), the two outermost layers rely on Silicon Strip Detectors (SSD). The six layers are positioned at radii of 3.9 cm, 7.6 cm, 15.0 cm, 23.9 cm, 38.0 cm, and 48.9 cm around the interaction point. The good track resolution is used to distinguish primary from secondary particles as well as increase the momentum resolution of tracks.

2.2.3.2 TRD

The Transition Radiation Detector (TRD) is used for PID with a focus on the separation between electrons and pions with $p > 1$ GeV/c. Transition radiation photons are produced if a charged relativistic particle crosses the boundary surface of two materials with different dielectric constants. The photons are detected in a Multi-Wire Proportional Chamber (MWPC) where a $\mathrm{Xe}/\mathrm{CO}_2$ gas mixture absorbs the photons and produces a prominent signal. The $d\mathrm{E}/d\mathrm{x}$ signal can be used to improve the general PID performance of ALICE. The coverage of $|\eta| < 0.84$ is achieved with 18 supermodules with 6 layers of 5 stacks each.

2.2.3.3 TOF

The Time-Of-Flight (TOF) detector measures the arrival time of particles to identify particles through their velocity. With the start signal from the T0 detector the velocity can be calculated. To achieve a time resolution of less then 40 ps multi gap resistive plate chambers are used, which provide the required fast response. With this time resolution it is possible to distinguish pions from kaons up to $p = 2.5$ GeV/c and kaons from protons up to $p = 4$ GeV/c. Like the TRD also TOF is subdivided into 18 supermodules that are assembled of 5 modules each and have a pseudorapidity coverage of $|\eta| < 0.9$.

2.2.3.4 PHOS

The PHOton Spectrometer (PHOS) as one of two calorimeters in the central barrel of ALICE focuses on the measurement of photons and neutral pions. It uses lead-tungstate crystals as detection material which provide a good energy resolution and are identical to the crystals used in the CMS experiment. With a crystal size of $22\,\mathrm{mm} \times 22\,\mathrm{mm}$ and a distance of $4.6\,\mathrm{m}$ to the interaction point also a good position resolution is realised. The setup consists of three modules with 3584 cells each and a total coverage of $|\eta| \leq 0.12$ and 60° in φ.

2.2.3.5 HMPID

The High-Momentum Particle Identification Detector (HMPID) uses the particle velocity to identify the particle species as well. Compared to the TOF it uses Cherenkov light produced in a radiator of C_6F_{14} with refraction index of 1.2989 to measure the velocity of the particles. After the radiator the Cherenkov photons enter the detection volume consisting of a MWPC with CsI photo cathodes. These convert the photons into electrons which induce the signal to be read-out. The detector layout allows to distinguish pions from kaons and kaons from protons, up to $p = 3\,\mathrm{GeV/c}$ and $p = 5\,\mathrm{GeV/c}$, respectively. Also the identification of light (anti-)nuclei at high momenta is possible. The maximum extent of the seven HMPID modules is $|\eta| < 0.6$ and $1.2^\circ < \varphi < 58.8^\circ$.

2.2.3.6 ACORDE

ACORDE, the only central detector located outside the L3 magnet, is placed on the three top faces of the magnet. It comprises of 60 modules, which are located within a pseudorapidity range of $|\eta| < 1.3$. Each module consists of plastic scintillator bars with dimensions of $26 \times 10 \times 300\,\mathrm{cm}^3$ and acts as veto or trigger for atmospheric muons. The triggers events are used for calibration and alignment purposes as well as for the analysis of high-energetic cosmic particles.

2.2.4 TPC

The Time Projection Chamber (TPC) [AA+|10] represents the main tracking device of ALICE. As such it provides the main data for the analysis of $\langle p_\mathrm{T} \rangle$ (chapter 3) and also contributes significantly

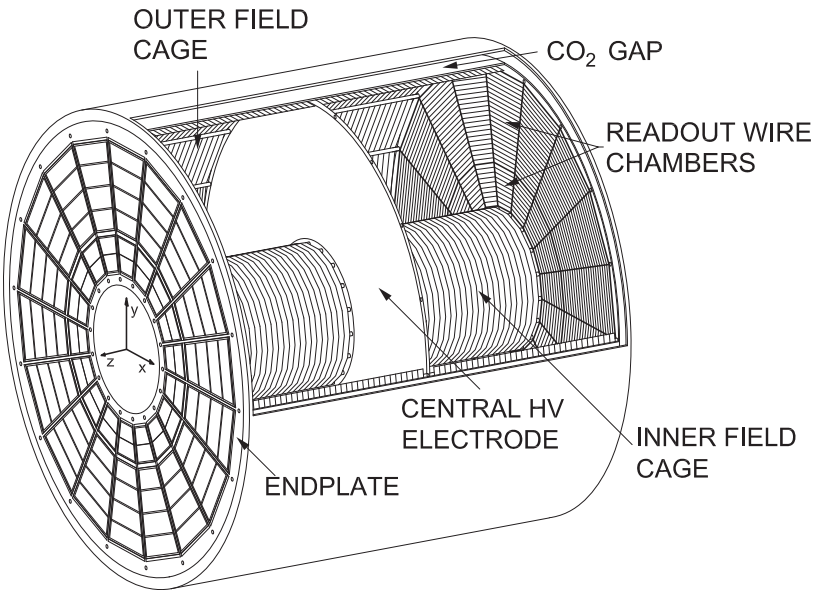

Figure 2.9: Sketch of the ALICE TPC layout [AA+|10]

to the analysis of isolated photons (chapter 4). It consists of a gas filled hollow cylinder with a length of 500 cm and an inner and outer radius of 85 cm and 250 cm, respectively, a sketch is shown in figure 2.9. The volume of ~ 90 m^3 was filled with a mixture of $Ne/CO_2/N_2$ before 2011, for the remaining run 1 (until beginning of 2013) the mixture was composed of Ne/CO_2. The volume is divided into two drift regions by the central electrode that provides a negative voltage of 100 kV and in conjunction with a field cage produces a homogeneous drift voltage of 400 V/cm. The end plates are segmented in 18 trapezoidal sectors in φ. Every sector is additionally divided radially in two readout chambers. Until the end of run 2 (end of 2018) the readout chambers consist of a multi-wire proportional chamber (MWPC) with a cathode pad plane, anode wires, cathode wires, and gating wires, as shown in figure 2.10. In radial direction, the readout pads are arranged in 160 rows; to cross all rows at nominal magnetic field a particle needs a minimum p_T of 150 MeV/c. In η, all charged particles within $|\eta| < 0.9$ can be measured with their full track length.

2.2.4.1 Working principal

Charged particles, crossing the gas volume of the TPC, ionize the gas along their path. The electrons and ions drift in opposite directions, due to the electric field of the central electrode. In figure 2.10 the path of a drifting electron in the TPC is shown. In the amplification region between the cathode wires and the anode wires the electrons are accelerated and produce an electron avalanche. Due to their slow drift velocity the remaining ions induce a mirror charge on

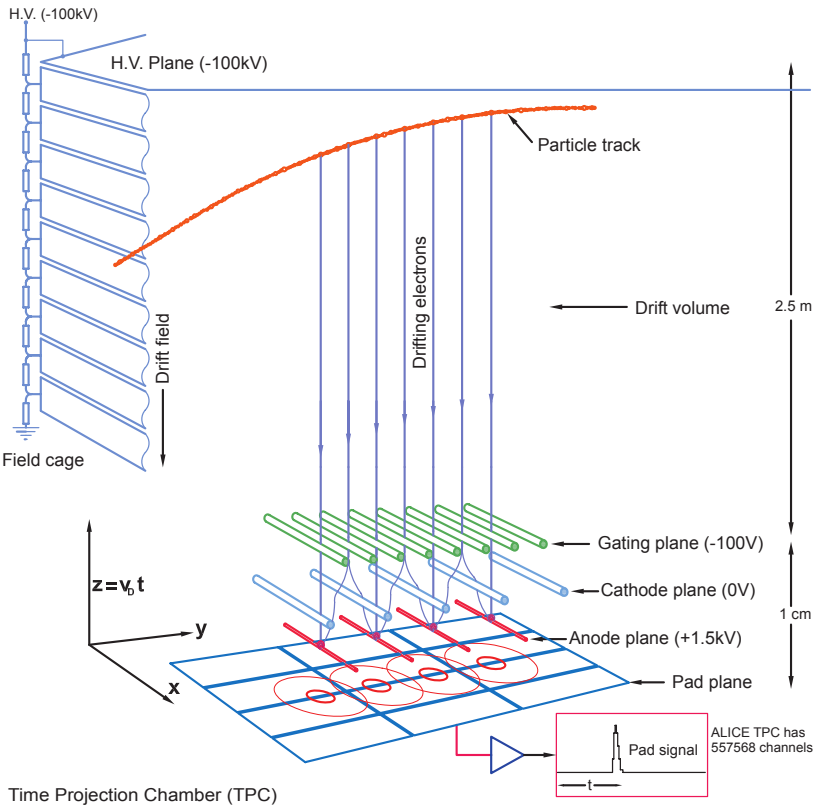

Figure 2.10: Detection mechanism of the TPC [Kal|12]

the pad plane. To reconstruct the local position of the particles inside the TPC the readout happens in time samples. In combination with the constant drift velocity this allows for a full 3-dimensional reconstruction of tracks. As the back drifting ions would create distortions inside the drift volume the gating grid is only open for the maximal drift time of 92 µs after a trigger has fired. While it is closed the wires are charged alternating to absorb both electrons and ions from the drift volume and the amplification region, respectively. As the MWPCs work in proportional mode, it is possible to gather information about the initial charge and thus about the energy loss of the ionizing particle. With the knowledge of the momentum and the energy loss of a particle it is possible to identify the particle species, as shown in figure 2.11.

2.2.5 EMCal

The ELectroMagnetic CALorimeter (EMCal) [ALICE|08b] is one of two electromagnetic calorimeters in ALICE and used as main detector for the isolated photon analysis (chapter 4). For the second LHC run the coverage of EMCal was extended with the installation of the DCal on the opposite site. While the layout differs in many points, the working principle and the detection mechanisms are the same.

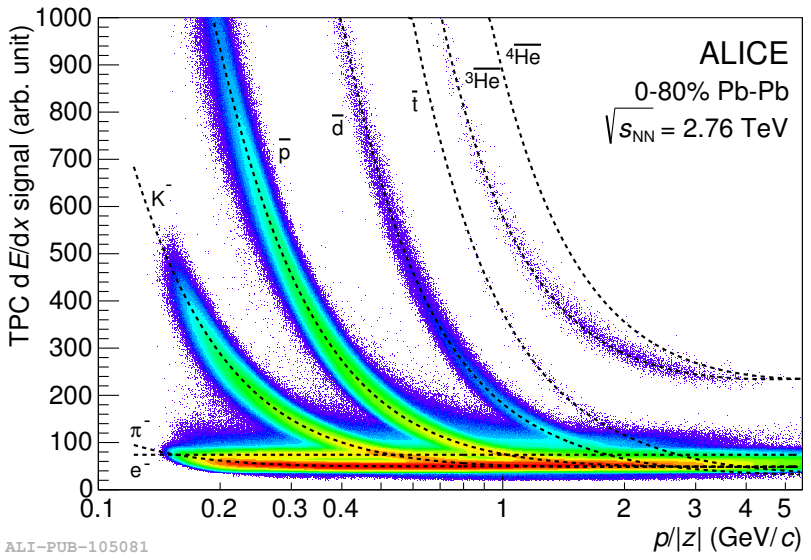

Figure 2.11: TPC dE/dx spectra for different particle species and the corresponding Bethe-Bloch parametrisation [ALICE|16]

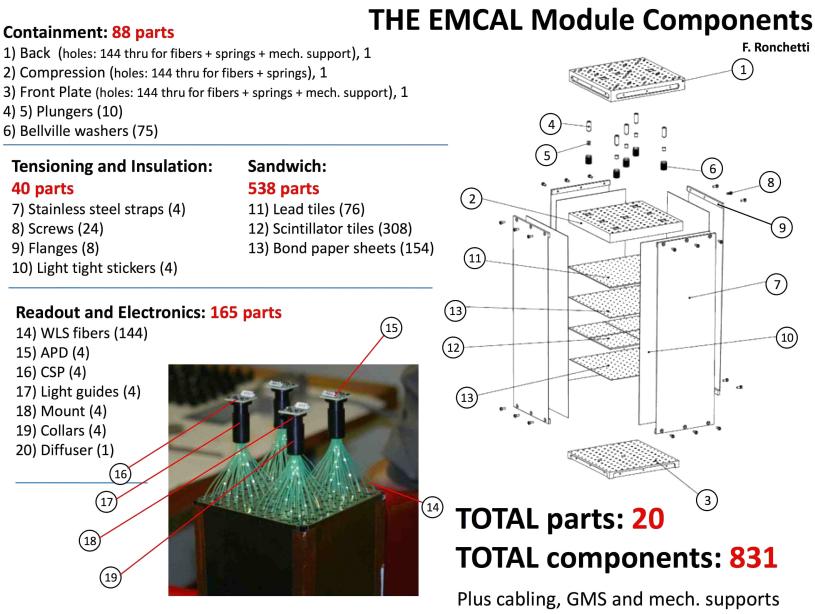

Figure 2.12: Explosion view of an EMCal module with all components, including the readout electronics [ALICE|08b]

2.2.5.1 Layout

The EMCal can be divided into the following substructures: from large to small this are supermodules, modules and towers/cells. While towers represent the smallest readout unit, during production the smallest units were modules, which contain 2 x 2 towers. A detailed structure with all important elements of a module is shown in sketch 2.12. It consists of 77 layers of scintillator alternating with 76 layers of Pb absorber, where every layer of scintillator is sandwiched between two layers of white paper for a better light yield. This Shashlik design represents a material thickness of ~ $20X_0$. To guarantee a clean readout of each tower the layers of scintillator are segmented into four tiles for each layer. The light created in the scintillators is collected by WLS fibres, which is read-out by an

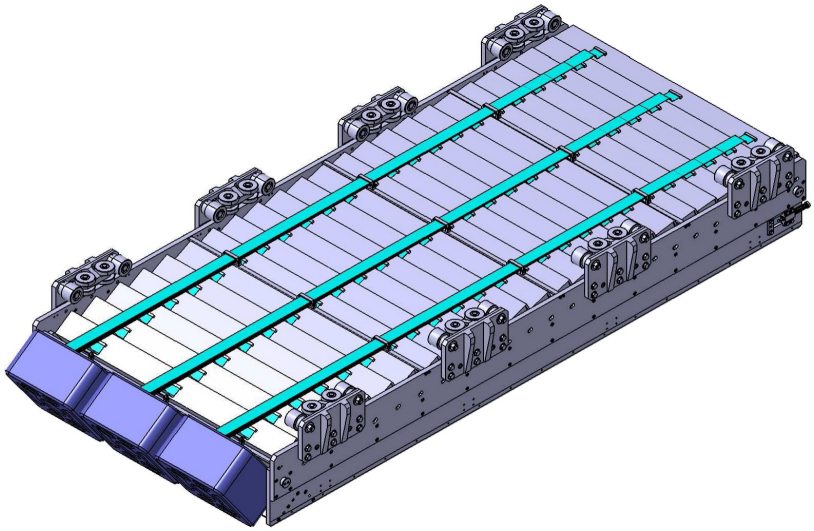

Figure 2.13: Backside of an EMCal supermodule, the inclination of the tilted modules increases to the outside [ALICE|08b]

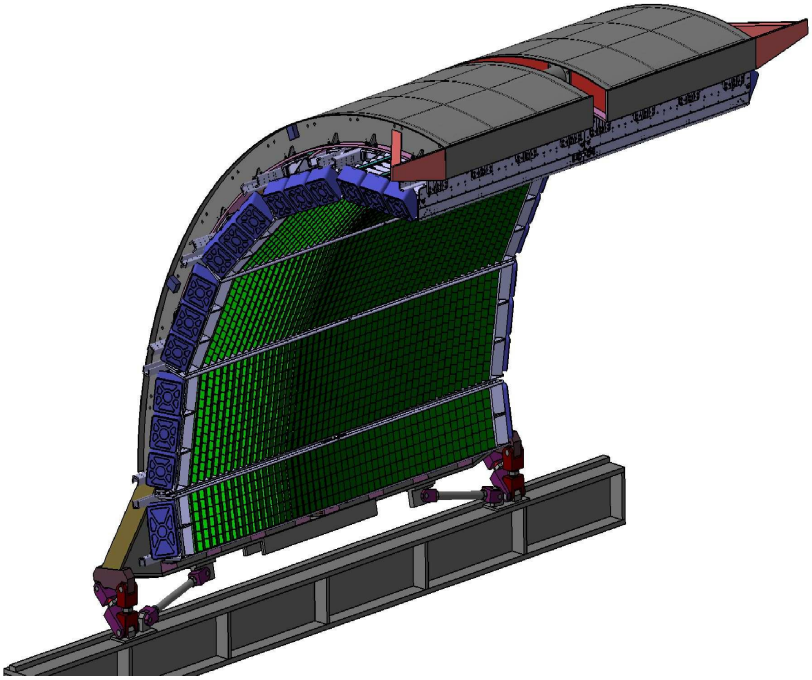

Figure 2.14: Drawing of the EMCal detector, with support structure and supermodules [ALICE|08b].

avalanche photodiode (APD). The 288 modules grouped in one supermodule are tilted according to their η position (see figure 2.13) to provide a uniform $\eta - \varphi$ coverage of $\Delta\eta \times \Delta\varphi = 0.014 \times 0.014$ for every module. The whole EMCal is made of 10 full size supermodules and 2 1/3 size super modules, arranged in an array of 5 1/3 times 2 supermodules as shown in figure 2.14. All supermodules together cover a pseudorapidity of $|\eta| < 0.7$ and a φ range of $\Delta\varphi = 107^{\circ}$.

For the readout, the data created by the APDs is processed by Front End Electronics (FEE), which process the signal and send a low gain and high gain value for each tower to the data readout. Additionally, the FEE together with the Trigger Region Unit (TRU) cards

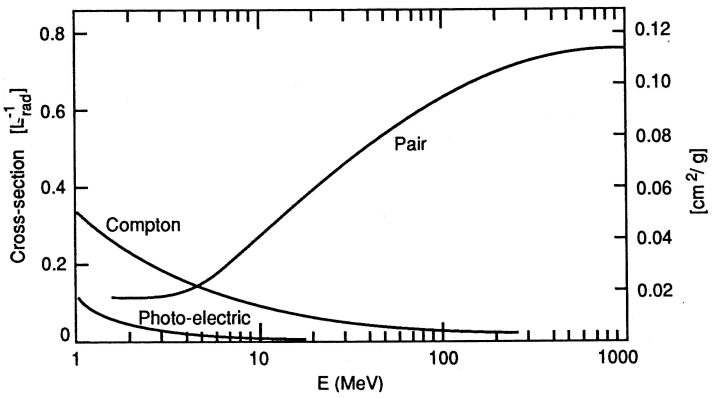

Figure 2.15: Cross-sections of energy-loss mechanisms for photons [Fab|87] in matter

perform a fast processing of the raw signal to provide different EMCal triggers to the ALICE trigger system.

2.2.5.2 Working principal

Calorimeters can be divided into two categories, depending on the measured particles. Electrons and photons are measured by electromagnetic calorimeters, while hadrons are measured by hadronic calorimeters. As this analysis focuses on photons, the description is limited to electromagnetic calorimeters. A description of hadronic calorimeters and a more detailed description of electromagnetic calorimeters can be found in [FG|03]. The detection mechanism of calorimeters is sensitive to all particles independent of their charge and provides a good energy resolution for high energetic particles. In calorimeters, particles are absorbed and their energy is deposited in the material. The amount of deposited energy correlates to a measurable physics property. i.e. light or electric current, which is read out. Compact electromagnetic calorimeters require a short electromagnetic radiation length X_0, that depends on the atomic number Z and the atomic mass A:

$$X_0(\,\mathrm{g\,cm^{-2}}) \simeq \frac{716\,\mathrm{g\,cm^{-2}} A}{Z(Z+1)\ln(287/\sqrt{Z})} \tag{2.1}$$

During the absorption process, the particle interacts with the material and creates a shower of secondary particles. The type of interaction depends on the particle type and its energy. For photons and electrons, the cross-sections of different processes over a wide energy regime is shown in figures 2.15 and 2.16, respectively. From the figures one can see that the electromagnetic shower consists only of electrons, positrons, and photons.

The shower properties of electrons and photons are similar and can both be described in terms of X_0 (compare [FG|03]). A second im-

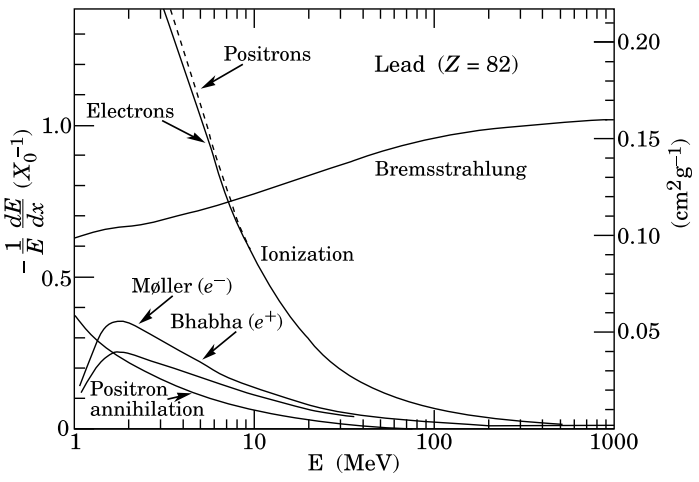

Figure 2.16: Cross-sections of energy-loss mechanisms for electron/positrons [PDG|02] in matter

portant variable for the characterization of calorimeter properties is the critical energy ϵ, which can be approximated in the following way for solids (gases).

$$\epsilon = \frac{610(710)\,\text{MeV}}{Z + 1.24(0.92)} \tag{2.2}$$

With ϵ and X_0 it is possible to approximate the longitudinal and the radial shower profile. These properties are required to properly chose the thickness and the cell size of a calorimeter. The thickness should be sufficient to contain most of the shower energy and still minimize the material use. The properties can be estimated with the following formulas.

$$t_{\text{max}} \simeq \ln \frac{E_0}{\epsilon} + t_0 \tag{2.3}$$

$$t_{95\,\%} \simeq t_{\text{max}} + 0.08\,\text{Z} + 9.6 \tag{2.4}$$

with t_{max} as the depth, in radiation length, where the most energy is deposited and $t_{95\,\%}$ as the length which contains 95 % of the original energy E_0. Because t_{max} increases logarithmically, the required thickness of a calorimeter only increases slowly. A good compromise is $\simeq 25X_0$, which results in an energy leakage below 1 % for 300 GeV electrons. The radial shower size can be estimated by the Molière radius (R_{M}):

$$R_{\text{M}}(\text{g/cm}^2) \simeq 21\,\text{MeV}\frac{X_0}{\epsilon(\text{MeV})} \tag{2.5}$$

This radius contains approximately 90 % of the shower energy over the full depth of the calorimeter and is roughly energy independent. The cell size of a calorimeter should be in the order of the corresponding Molière radius to provide a good position resolution.

The energy measured in an ideal calorimeter depends on the signal induced in the detection material, which is correlated to the total track length of all ionizing particles in a shower T_0:

$$T_0 \propto X_0 \frac{E_0}{\epsilon} \tag{2.6}$$

Thus, the energy resolution depends on the fluctuation of T_0, which can be described as stochastic process. Thus the energy resolution can be written as:

$$\frac{\sigma(E)}{E} \propto \frac{1}{\sqrt{T_0}} \propto \frac{1}{\sqrt{E_0}} \tag{2.7}$$

In a realistic calorimeter, the energy resolution additionally depends on further detector properties: The two major contributions are the noise which is created in the readout chain and a constant offset created by imperfections of the calorimeter. With summing these three contributors quadratically, the energy resolution can be written in the following way:

$$\frac{\sigma}{E} = \frac{a}{\sqrt{E}} \oplus \frac{b}{E} \oplus c \tag{2.8}$$

Where a, b and c are the detector specific factors for the stochastic term, the noise term, and the constant term, respectively.

2.2.6 Data Taking

2.2.6.1 Trigger

The trigger decision in ALICE is performed by the Central Trigger Processor (CTP). It evaluates the data from detectors contributing to the trigger decision and sends a signal to all detectors in case their data is read-out. Detectors responsible for the trigger decision are pooled into different trigger classes. The detectors to be read-out are grouped into trigger clusters. To enhance the selection of different physics, trigger classes and trigger clusters are combined accordingly.

The trigger decision is evaluated in a multi level process. During the first stage (L0) the data from fast responding detectors are evaluated. The L1 trigger additionally includes data from detectors with a longer processing time. This includes detectors which are located far away from the interaction point (ZDC), detectors with longer

read-out time (i.e. TRD) and also processed data from fast detectors (i.e. EMCal).

After a successful trigger evaluation, a signal is sent to the corresponding trigger cluster. The data from the detectors is sent to the Data Acquisition (DAQ) system.

For the analyses of this thesis two trigger classes are important. The minimum bias trigger as basic trigger to accept all events, but rejecting non physical interactions. In pp collisions, a signal from both sides of the V0 detector is required. For Pb–Pb collisions, an additional signal from the SPD is needed to accept the event. The EMCal trigger is used to increase the yield of events with high-energetic photons. It can be used as L0 trigger as well as L1 trigger. In the L0 configuration, the front-end electronics sums the energy of a module and fires if the energy exceeds the threshold. In case of the EMCal L1 trigger, a successful EMCal L0 trigger is required. In the additional available processing time, the CTP recalculate the energy in all possible 2x2 (photon case) and 16x16 (jet case) tower combinations and provides a more versatile trigger. In the 7 TeV pp data taken in 2011, only the L0 trigger with a threshold of 5.5 GeV was used.

2.2.6.2 Data preparation

For analysis purposes, ALICE uses a common data format for recorded data and simulations. While the output format is identical, the processing and preparation differs in both cases.

All signals recorded by the detectors are stored as raw signals. These are further processed during the reconstruction. During the reconstruction process, the signals from the detectors are combined to tracks and clusters to reduce the computing requirements in the analysis. The results of the reconstruction are stored in Event Summary Data (ESD) files. The recoded data is labelled and divided into samples. The classification depends on three parameters: year, period and run. For each year the data is divided into periods, with similar conditions, like same collision system or bunch structure of the LHC. Typically, a period covers a few weeks of data taking. Within a period the data is divided into runs, which represent a time span with constant conditions of the detectors in ALICE. A run can last from a few minutes to a few hours. Depending on the duration of the run and the beam conditions, a run contains between a few thousands and afew million events.

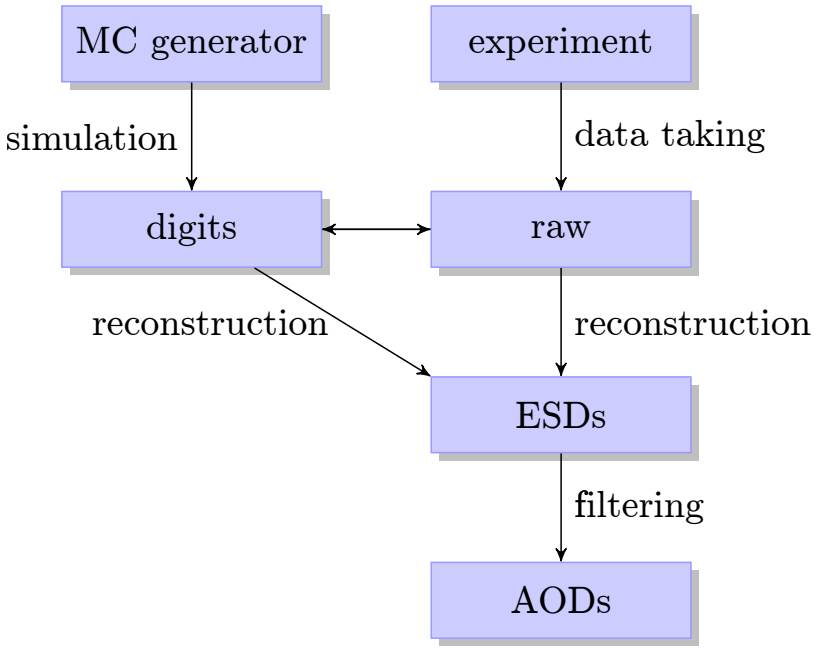

Figure 2.17: Schematic view of the reconstruction and simulation chain in ALICE [Kle|14]

ESDs are also produced in the simulation process. The simulation process is split into two subprocesses. In a first step, the origin of the particles is simulated. This can be either a dedicated particle well or a simulation of particle collisions. To simulate a particle collision, dedicated simulations are used for pp collisions (i.e. PYTHIA [SMS|06]) and Pb–Pb collisions (i.e. HIJING [WG|91]). Depending on the analysis additional generators are used for comparison(i.e.EPOS [PK$^+$|15]). In a second step, the particle transport, processes inside the detectors and the simulation of the detector responses are computed. For this also different transport simulation programs are available (i.e. GEANT3 [BB$^+$|94], GEANT4 [GEANT4|03]). The simulated detector responses are also reconstructed into ESDs.

To reduce the computation power and storage requirements needed for the analysis, ESDs can be further filtered into Analysis Object Data (AOD). These contain only data which fulfil certain quality cuts and does not included analysis irrelevant tracks and clusters. The whole reconstruction chain is visualised in figure 2.17.

2.3 Clusterizer

In the calorimeters the signals of the single cells are merged into clusters. The working principle of the clusterizer for the EMCal and PHOS is similar but differs in details like the minimal cell energy. Signals from electronic noise are reduced during the clusterization by the application of two energy thresholds. A cluster

is only formed around a cell whose energy surpasses the so called seed threshold. Each cell merged into a cluster has to satisfy the cell threshold. Typically the seed threshold is higher than the cell threshold.

The EMCal uses two different clusterizers (v1 and v2). While v1 is based on a simple summation of cells, v2 additionally splits clusters with more than one local energy maximum. In figure 2.18 two examples for the two different clusterizers are shown. The v1 clusterizer starts with the highest energetic cell in the calorimeter and checks for each of the orthogonal adjacent cells if the cell threshold is exceeded. In this case the cell is added to the cluster and the neighbouring cells of the newly added cell are checked. This procedure is repeated until all cells in the vicinity of the cluster which pass the cell threshold are added. The highest energetic cell, which is not assigned to a cluster, is used as seed for a new cluster. This routine is repeated until all cells with energy above the seed threshold are associated with a cluster.

The algorithm for the v2 clusterizer is based on the same approach as the v1 clusterizer. While the v1 clusterizer accepts all neighbouring cells above the cell threshold, the v2 clusterizer in addition requires that the energy of neighbouring cells is lower then the current cell. An increasing energy in the neighbouring cells hints to a contribution from a different particle. The splitting of clusters allows for measuring particles with a small spatial separation independently.

2.3.1 Cluster properties

The clusterization process defines different cluster properties that are relevant for the isolated photon analysis. The cluster energy as the most relevant property is calculated by summing the energies of all associated cells. Due to the fast response of the EMCal it is possible to assign clusters to different bunch crossings. The cluster time is defined as the time of the seed cell. The distribution of the cells assigned to a cluster defines the cluster center and the cluster shape. For the calculation of these cluster properties a weight w_i is assigned to every cell, taking the cell energy and the relative contribution to the cluster energy into account:

$$w_i = 4.5 - \log\left(\frac{E_i}{E_{cluster}}\right) \tag{2.9}$$

Wtih 4.5 as empirical value evaluated from test beam data to achieve the best spatial resolution (details can be found in [AO$^+$|92]). The

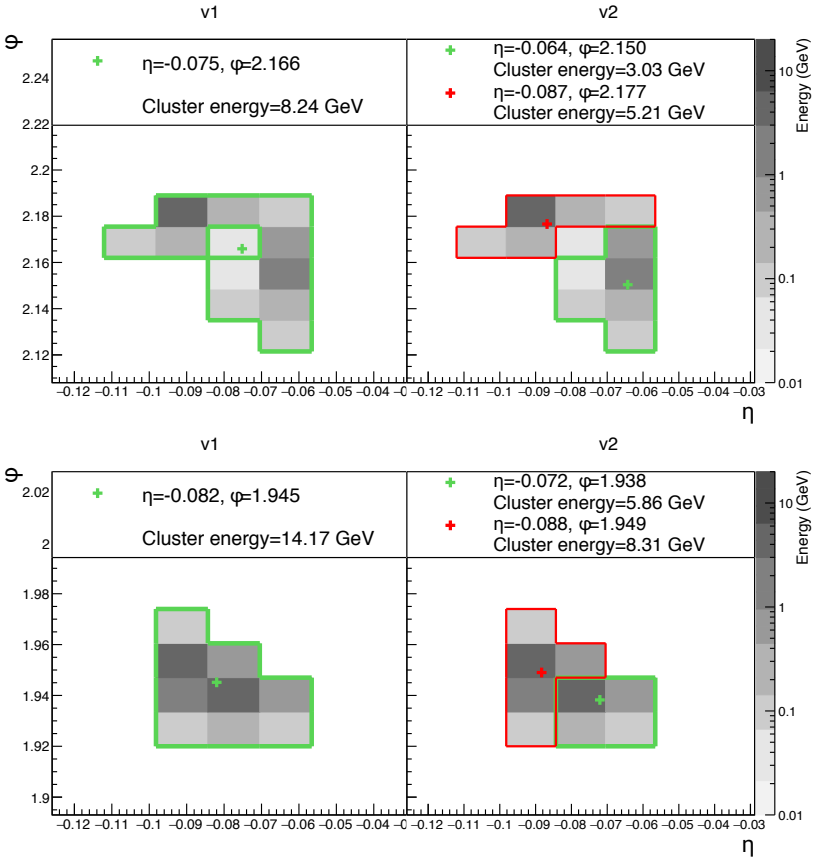

Figure 2.18: Comparisons of v1 and v2 clusterizer for two merged π^0 [Wol|14]

cluster shape can reveal information about the nature of the detected particle, especially if the two photons from a neutral meson decay merged into one cluster and create an elliptic cluster shape. The shape is characterised by the cluster parameters σ^2_{short} and σ^2_{long}, which correspond to the minor and major axis of an ellipsoid parametrization of the cluster shape. σ^2_{short} and σ^2_{long} can be derived from the covariance matrix of the ellipse (a detailed description can be found in [CB|05, ALICE|06]):

$$S = \begin{pmatrix} S_{xx} & S_{xy} \\ S_{yx} & S_{yy} \end{pmatrix} \tag{2.10}$$

with x and y representing the cluster coordinates η and φ. $s_{\varphi\varphi}$, $s_{\eta\eta}$ and $s_{\varphi\eta}$ are defined in the following way:

$$s_{AB} = \frac{\sum_i w_i A_i B_i}{\sum_i w_i} - \frac{\left(\sum_i w_i A_i\right)\left(\sum_i w_i B_i\right)}{\left(\sum_i w_i\right)^2} \tag{2.11}$$

Finally, this results in the following definitions for σ^2_{short} and σ^2_{long}:

$$\sigma^2_{\text{short}} = \frac{s_{\varphi\varphi} + s_{\eta\eta}}{2} - \sqrt{\left(\frac{s_{\varphi\varphi} - s_{\eta\eta}}{2}\right)^2 + \left(s_{\varphi\eta}\right)^2} \tag{2.12}$$

$$\sigma^2_{\text{long}} = \frac{s_{\varphi\varphi} + s_{\eta\eta}}{2} + \sqrt{\left(\frac{s_{\varphi\varphi} - s_{\eta\eta}}{2}\right)^2 + \left(s_{\varphi\eta}\right)^2} \tag{2.13}$$

In case of the v1 clusterizer also the Number of Local Maxima in a cluster (NLM) is stored as important cluster property.

The usage of the above mentioned cluster properties in the isolated photon analysis is discussed in chapter 4.2.3.

Average Transverse Momentum

3

In this chapter the analysis of the average transverse momentum $\langle p_{\mathrm{T}} \rangle$ in Pb–Pb collisions will be discussed. The analysis is part of a comparison of $\langle p_{\mathrm{T}} \rangle$ in pp, p–Pb and Pb–Pb collisions and the combined results are published in [ALICE|13d].

Details about the data and the corresponding simulations used for the Pb–Pb analysis are discussed in section 3.1. As shown in figure 3.1, the p_{T} spectrum is dominated by low p_{T} tracks. Consequently, also the $\langle p_{\mathrm{T}} \rangle$ measurement is dominated by low p_{T} particles. While this analysis focuses on all charged particles (a detailed definition and further details of the track selection can be found in section 3.2), other analyses studying the mass dependence of $\langle p_{\mathrm{T}} \rangle$ for identified particles can be found in [ALICE|15] and [ALICE|13b].

The average transverse momentum is measured as a function of the event true track multiplicity n_{ch}. n_{ch} is chosen as observable, as it contains corrections for detector effects like detector resolution and efficiency and allows a comparison between different experiments and theory predictions. Because n_{ch} cannot be obtained directly, a reweighting procedure is applied to correlate the number of accepted tracks (n_{acc}) with n_{ch}. A detailed description of the used procedure together with results from the $\langle p_{\mathrm{T}} \rangle$ calculation can be found in section 3.3. In the following section 3.4 the evaluation of the corresponding systematic uncertainties is described. In addition to the systematic uncertainties, in section 3.5 the influence of non-hadronic interactions is studied. These interactions generate a significant background in peripheral Pb–Pb collisions and thus affect low multiplicity results. Section 3.6 focus on the comparison of the results of $\langle p_{\mathrm{T}} \rangle$ analysis in Pb–Pb collisions with the other $\langle p_{\mathrm{T}} \rangle$ measurements performed in other collision systems by ALICE. The shown results represent the status of the $\langle p_{\mathrm{T}} \rangle$ analysis at publication time. In the meantime improvements for tracking and new techniques for the $\langle p_{\mathrm{T}} \rangle$ were developed. These enhancements together with possible measurements by new data sets are discussed in section 3.7.

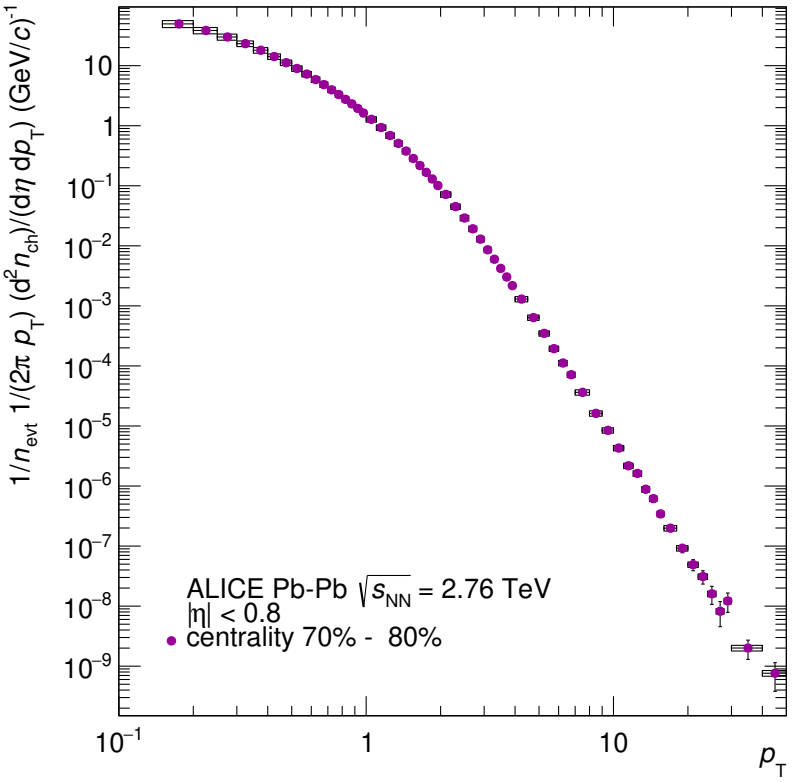

Figure 3.1: p_T spectrum of charged particles at peripheral Pb–Pb collisions at $\sqrt{s_{NN}}$ = 2.76 TeV (data from [ALICE|13a]).

3.1 Data set and MC production

In this analysis, the average transverse momentum in Pb–Pb collisions at a collision energy of $\sqrt{s_{NN}}$ = 2.76 TeV is measured. The data set with a total statistics of about 16 million minimum bias triggered events was recorded in 2010 and within ALICE is referred to as LHC10h. The used data consists of 90 runs. A full list of runs and their statistics can be found in Appendix A.

For simulation purposes a HIJING production with 1.5 million events is used. To reproduce the detector behaviour properly, the simulation is divided into 90 runs as well in order to take the detector conditions during data taking into account.

3.2 Track selection

For the analysis charged primary particles are used. A primary particle is defined by ALICE as: *"A primary particle is a particle with a mean proper lifetime τ larger than* 1 cm/c , *which is either a) produced directly in the interaction , or b) from decays of particles with τ smaller than* 1 cm/c , *restricted to decay chains leading to the interaction."* [ALICE|17a] The track selection applies different

quality criteria, including the requirement of a hit in the innermost ITS layer. Faulty parts in the ITS implicate a non-uniform spatial distribution after the track selection. Due to different priorities, two settings are used for the track selection. For the $\langle p_{\mathrm{T}} \rangle$ calculation, an accurate p_{T} resolution is needed, while for the multiplicity classification an uniform detector response is more crucial.

In order to achieve a good p_{T} resolution, track data from the ITS is necessary to constrain the track parameters. Consequentially, only tracks passing the ITS criterion are used for the $\langle p_{\mathrm{T}} \rangle$ calculation. To circumvent the non-uniform track distribution, in the reweighting procedure (section 3.3.1) the multiplicity of TPC-standalone tracks is used.

3.3 Measurement of average transverse momentum

The average transverse momentum of charged particles is calculated using all tracks within a kinematic range of $|\eta| < 0.3$ and $0.15 \leq p_{\mathrm{T}} < 10\,\mathrm{GeV/c}$. The limitation was chosen to perform the comparison in the same pseudorapidity for all collision systems. For symmetric collision systems in the TPC a pseudorapidity range of $|\eta| < 0.8$ is used. In p–Pb collisions, particles measured by the TPC have a pseudorapidity of $1.3 \leq \eta < 0.3$, as a result of the moving centre-of-mass system. With an additional requirement of a symmetric coverage in pseudorapidity, the coverage is limited to $|\eta| < 0.3$ in all collision systems. The lower limit of p_{T} is given by the minimum track momentum needed to cross the full TPC radius. For the upper limit different conditions are taken into account. With increasing p_{T} the number of tracks is decreasing drastically and the p_{T} resolution of tracks worsens as the bending radius is increasing. These considerations result in a maximum p_{T} cut at $10\,\mathrm{GeV/c}$, to ensure a constantly high track quality and good statistics. To assure a consistent track quality, additional selection criteria are applied. A detailed study of the track criteria can be found in [Kni|15].

Every event is classified by the accepted multiplicity (n_{acc}) of TPC-standalone tracks that pass the track selection. For each multiplicity class a p_{T} spectrum is created. From this spectrum the average transverse momentum of the class is calculated. For the calculation of

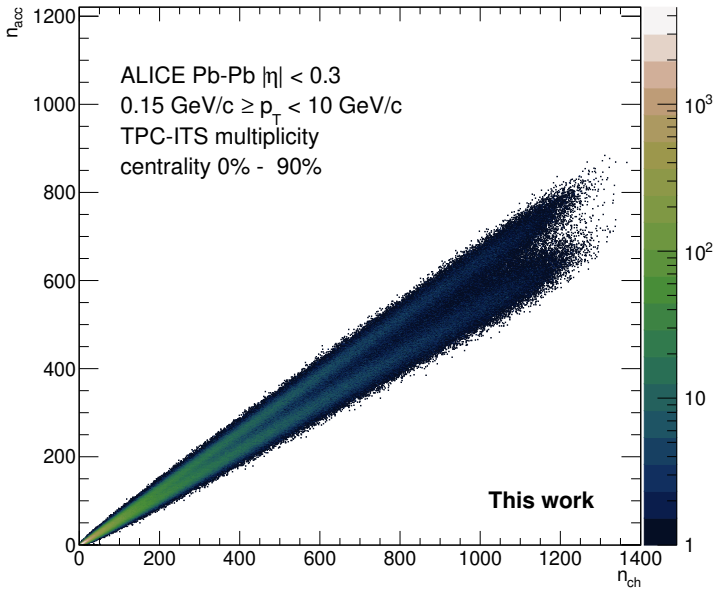

(a)

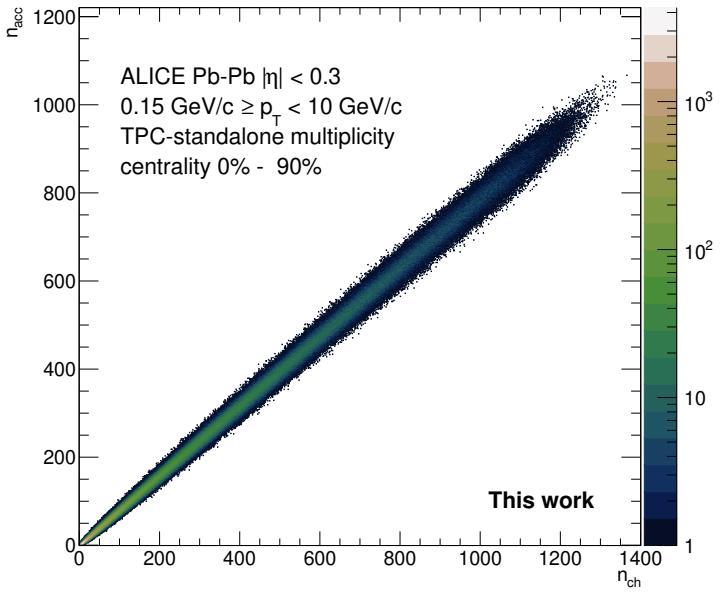

(b)

Figure 3.2: Correlation matrices for Pb–Pb collisions with TPC-ITS tracks (a) and TPC-standalone tracks (b).

$\langle p_T \rangle_{n_{acc}}$ the following formula is used,

$$\langle p_T \rangle_{n_{acc}} = \frac{\sum y\,(p_T) \cdot w\,(p_T) \cdot p_T}{\sum y\,(p_T) \cdot w\,(p_T)} \tag{3.1}$$

with the yield y, the p_T width of the bin w, and the value at bin centre p_T.

3.3.1 Reweighting

To obtain the average transverse momenta for charged particles ($\langle p_{\mathrm{T}} \rangle (n_{\mathrm{ch}})$) a reweighting procedure is used. The reweighting procedure is based on HIJING simulations of Pb–Pb collisions and the related detector response. The simulations make it possible to compare the number of tracks created in the collision and passing through the detectors, with the number of reconstructed tracks. The resulting correlation is shown in figure 3.2, with the number of created tracks (n_{ch}) on the x-axis and the number of accepted tracks (n_{acc}) on the y-axis. The reweighting procedure calculates for every multiplicity bin in n_{ch} the sum of all $\langle p_{\mathrm{T}} \rangle$ values in n_{acc} weighted by their relative contribution to this n_{ch} multiplicity $R(n_{\mathrm{acc}}, n_{\mathrm{ch}})$. The procedure can be expressed as

$$\langle p_{\mathrm{T}} \rangle (n_{\mathrm{ch}}) = \sum_{n_{\mathrm{acc}}} \langle p_{\mathrm{T}} \rangle (n_{\mathrm{acc}}) \cdot R(n_{\mathrm{acc}}, n_{\mathrm{ch}}) \,. \tag{3.2}$$

The acceptance limitations of the ITS as described in section 3.2 induce a z-vertex dependency of the multiplicity. As a result the correlation matrix as shown in figure 3.2a contains a split distribution and consequentially cannot be used for the determination of n_{ch}. To obtain reasonable results from the reweighting procedure, a narrow correlation matrix is needed. By using only TPC tracks for the multiplicity estimation as described above, a narrow and distinct distribution can be achieved, as shown in figure 3.2b.

3.4 Systematic uncertainties for the average transverse momentum

The total systematic uncertainties of the measurement of $\langle p_{\mathrm{T}} \rangle$ consist of multiple individual contributions which are added in quadrature. For the contributions of track selection, secondary contamination and event selection to the total systematic uncertainty, the analysis of $\langle p_{\mathrm{T}} \rangle$ is repeated with different settings. Further systematic uncertainties are adopted from the Pb–Pb spectra analysis [ALICE|13a]. A detailed study about the systematic variations can be found in [Kni|15].

To estimate the systematic uncertainties, the track selection criteria are varied to a more a stringent and a looser value. The variations either increase the track quality while reducing the statistics or vice versa. For each case, the average p_{T} is calculated and the difference

Variable	Standard value	Variation 1	Variation 2
χ^2 TPC cluster	4	5	3
ITS requirement	Hit in any SPD layer required	No SPD hit required	
No. of crossed rows	120	130	100
Crossed rows over findable	0.8	0.9	0.7

Table 3.1: Variations of the track selection used for the calculation of systematic uncertainties.

to the standard setting is treated as an individual contribution. The track criteria and their variations are listed in table 3.1. The results of the variations are shown in figure 3.3a, as well as the combined uncertainty of all tracking variations. In total, the contributions sum to a maximum of 0.45 %. For most multiplicities the track selection contributes about 0.2 % to the total uncertainty.

Contamination by secondary particles mainly arises from strange particles with a long life-time. The contribution of the secondary contamination is estimated by repeating the $\langle p_{\mathrm{T}} \rangle$ analysis without a secondary particles correction. To account for the influence of the event selection, the analysis is repeated with a z-vertex cut of 5 cm instead of 10 cm.

The contributions of the secondary contamination and the z-vertex cut are shown in figure 3.3b together with all other contributions. Both contributions only have minor influence of around 0.1 %. The main sources of uncertainty with 0.6 % and 0.35 % are the uncertainties on the tracking efficiency and the particle composition in MC simulation, respectively. In contrast, the trigger bias and vertex bias only play a minor role.

3.5 Discrimination of electromagnetic interactions from hadronic interactions

An important goal of the event selection is the differentiation of hadronic interactions from non-hadronic ones. Especially in the low multiplicity region, events from non-hadronic interactions contribute significantly to the measured event selection. This background is assumed to originate from electromagnetic interactions of the Pb nuclei [ALICE|13c], whose production mechanism depends quadratically on the charge of the particles. Photons produced in the electromagnetic interaction of the nuclei interact with other Pb nuclei and excite them. The main decay process of the excitation is the

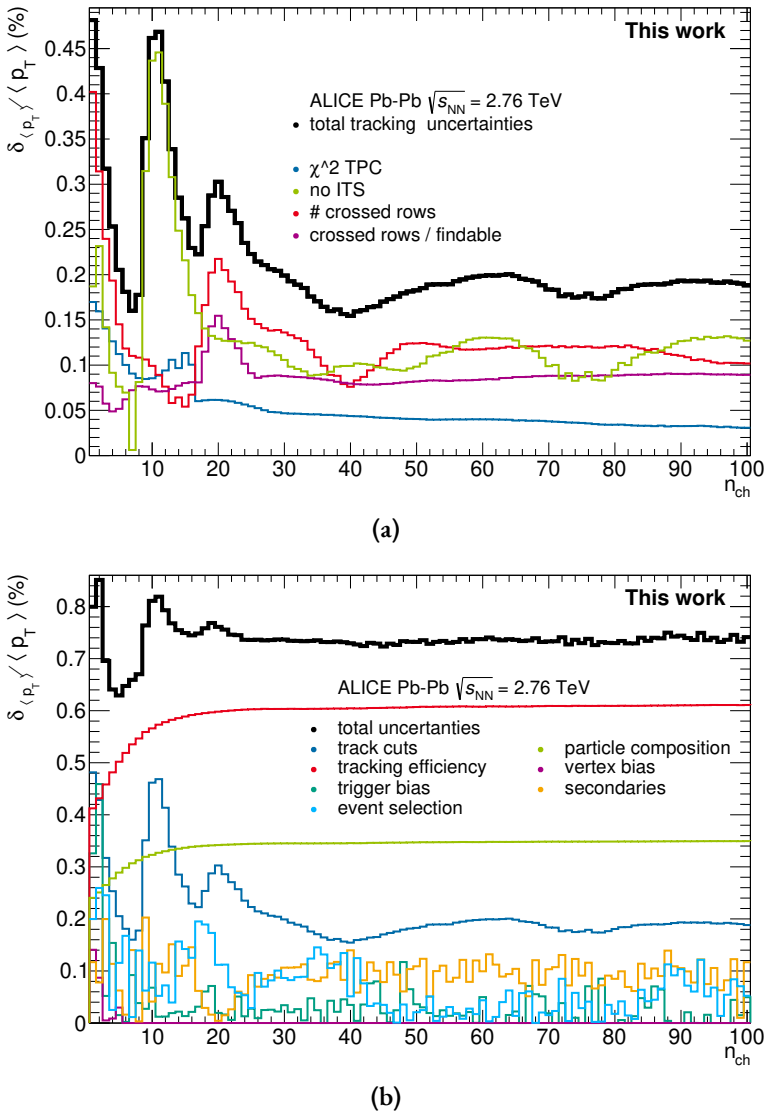

Figure 3.3: Overview of contributions to systematic uncertainties. Contributions by different variations of the track selection (a) and all contributions (b).

emission of a single neutron, which can be detected in the ZN calorimeters of the ZDC.

In Pb–Pb collisions the background reduction is part of the centrality determination. A detailed explanation of the centrality determination and background reduction used in the analysis can be found in [ALICE|13c]. In ALICE, the centrality is determined by a measurement of the signal amplitudes in the V0 detectors. The measured distribution is parametrised by a negative binomial distribution. The parametrisation allows to slice the events into centrality percentiles through integration of the function. Cuts in the neutron detector of the ZDC are applied in the centrality determination to reduce the background from electromagnetic interactions. These cuts reduce the background significantly but are not able to completely reject non-hadronic events. For most analyses a centrality selection of 0 % to 80 % or 90 % is used to minimize the influence of non-hadronic in-

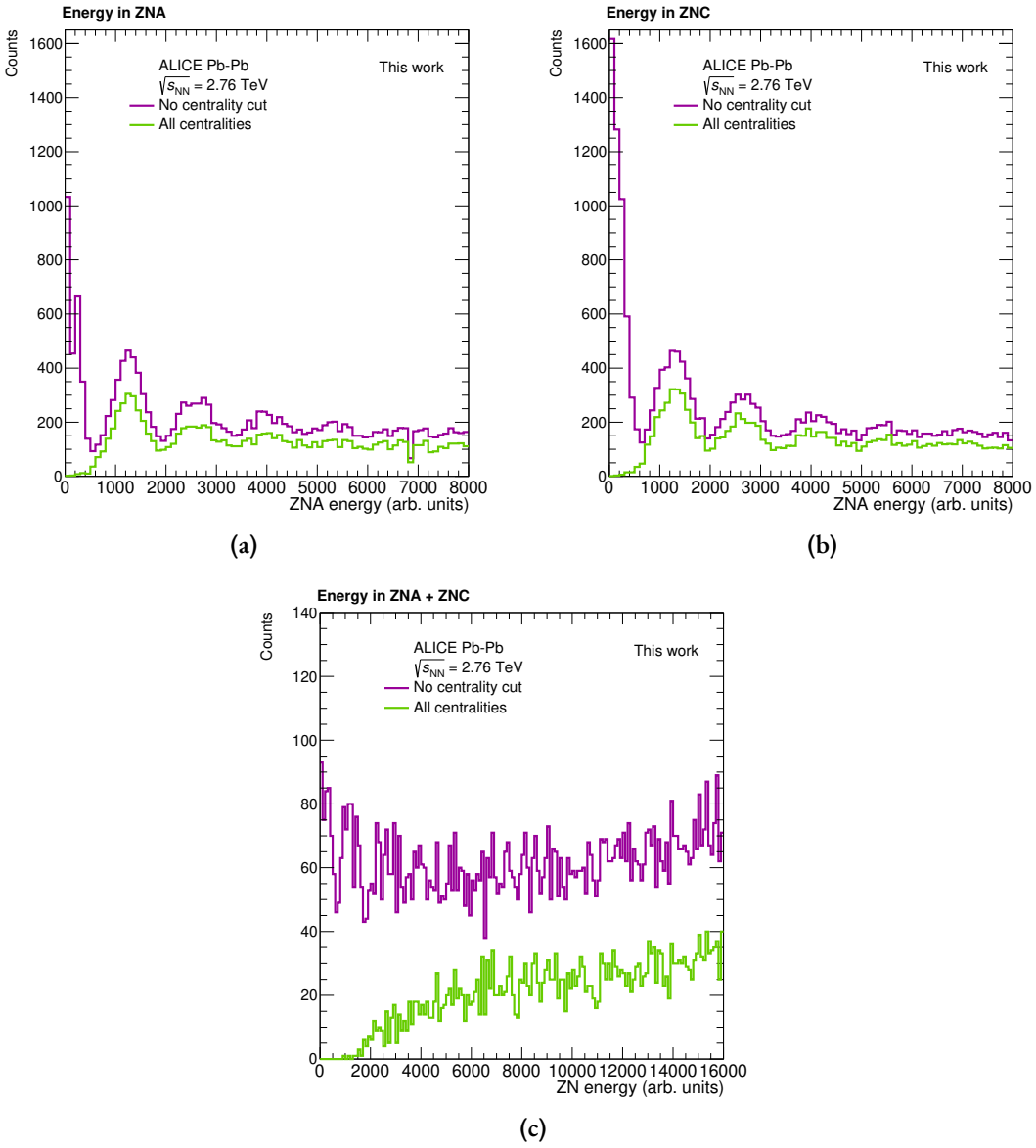

Figure 3.4: Energy deposition from neutral particles measured with the ZN sub-detector of the ZDC. With (green) and without (purple) centrality selection, for A-side only (a), C-side only (b) and the sum of both (c).

teractions and reduce uncertainties of the centrality determination. As the comparison between the different collision systems is only possible for peripheral events with low multiplicities such a selection is not feasible for this analysis. To better understand the effect of the centrality selection the signals in the ZDC detector are studied in the following.

In figure 3.4 the energy deposition for low multiplicity events in the ZN detectors is plotted, for the ZNA detector (a), the ZNC detector (b) and the sum of the deposited energy in both detectors (c). In each figure the energy distribution is plotted for all events passing the event selection (purple) and events passing additionally the cent-

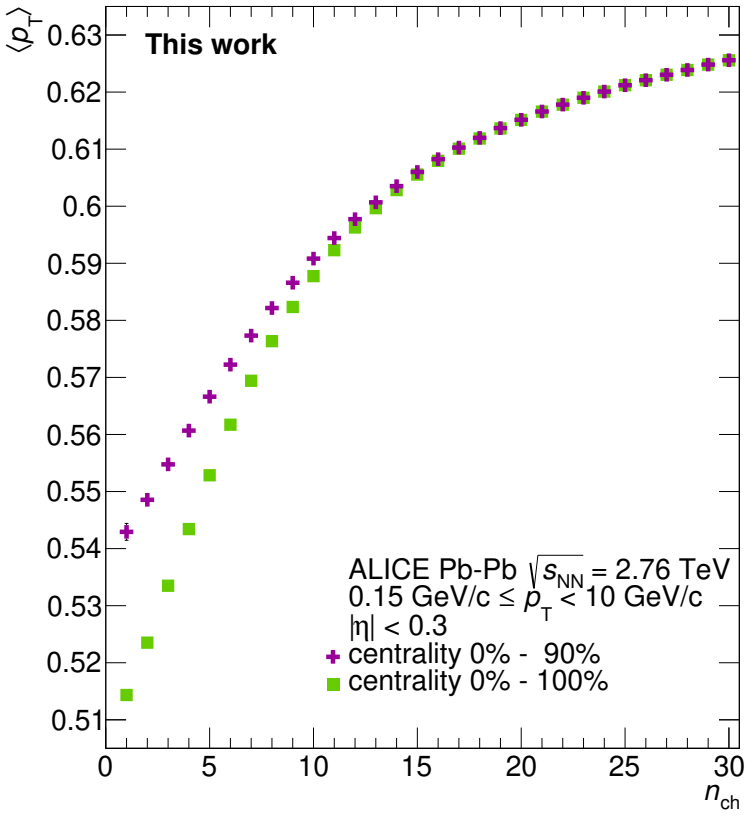

Figure 3.5: Effect of the most peripheral events on $\langle p_T \rangle$ for low multiplicity events.

rality selection. The energy distribution is limited to low energies, as only low numbers of detected neutrons are relevant for the rejection of non-hadronic events. For the single ZN calorimeters local maxima in the distribution are visible at approximately 1300, 1600 and 4000. These peaks correspond to the deposition of one, two and three neutrons in the calorimeter, respectively. By applying the centrality selection, mostly events with an energy deposit less the energy of a single neutron are rejected. A large fraction of the electromagnetic background is rejected by the centrality selection. Due to their large cross-section, non-rejected background events still contribute significantly to the peripheral events passing all cut criteria.

To estimate the influence of the contamination the analysis is performed in the range of 0 % to 100 % centrality in addition to the range of 0 % to 90 % centrality. In figure 3.5 the average p_T for both centrality selections is plotted against the multiplicity for events with $n_{ch} < 30$. The difference of the two selections only affects events with n_{ch} smaller than 15. For $n_{ch} = 1$, the difference in $\langle p_T \rangle$ between the two selections is about 5.5 %. The difference between the two variations is added as independent contribution to the systematic uncertainties described in section 3.4 for events with $n_{ch} \leq 15$.

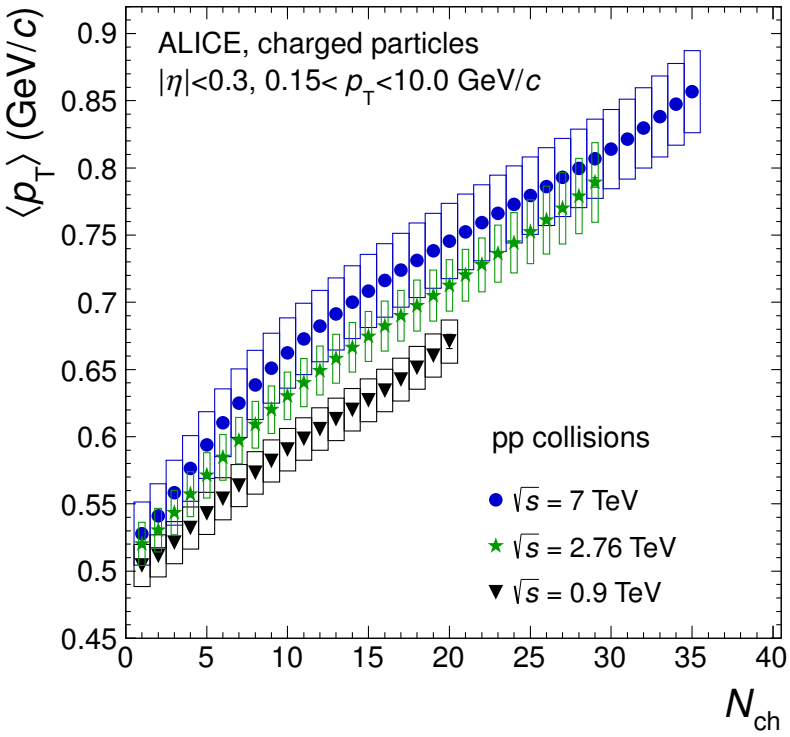

Figure 3.6: Comparison of average p_T in pp collisions for three different energies [ALICE|13d].

3.6 Comparison of average transverse momentum in different collision systems

In the following the results for the average transverse momentum measurements for pp collisions at $\sqrt{s}$ = 0.9 TeV, 2.76 TeV, and 7 TeV are compared, as well as the results for pp collisions at $\sqrt{s}$ = 7 TeV, p–Pb collisions at $\sqrt{s_{\mathrm{NN}}}$ = 5.02 TeV, and Pb–Pb collisions at $\sqrt{s_{\mathrm{NN}}}$ = 2.76 TeV. In a first step the collision energy dependency of the $\langle p_{\mathrm{T}} \rangle$ measurement is studied by comparing the results of pp collisions at different collision energies. The study together with previous $\langle p_{\mathrm{T}} \rangle$ measurements by other experiments is used to estimate the effect of differing collision energies.

In figure 3.6 $\langle p_{\mathrm{T}} \rangle$ is plotted against n_{ch} for the three different pp collision energies. Independent of the collision energy, pp collisions show a linear rise of $\langle p_{\mathrm{T}} \rangle$ with increasing multiplicity n_{ch}. For all three energies, the slope changes around $n_{\mathrm{ch}} \approx 12$. While the collision energy varies by nearly one order of magnitude, the $\langle p_{\mathrm{T}} \rangle$ increases at most by 10 %. The dataset of pp collisions at $\sqrt{s}$ = 7 TeV contains the most recorded events of the three datasets and allows to calculate $\langle p_{\mathrm{T}} \rangle$ up to $n_{\mathrm{ch}} = 35$. Accordingly, the 7 TeV dataset is used for the comparison of the different collision systems to achieve

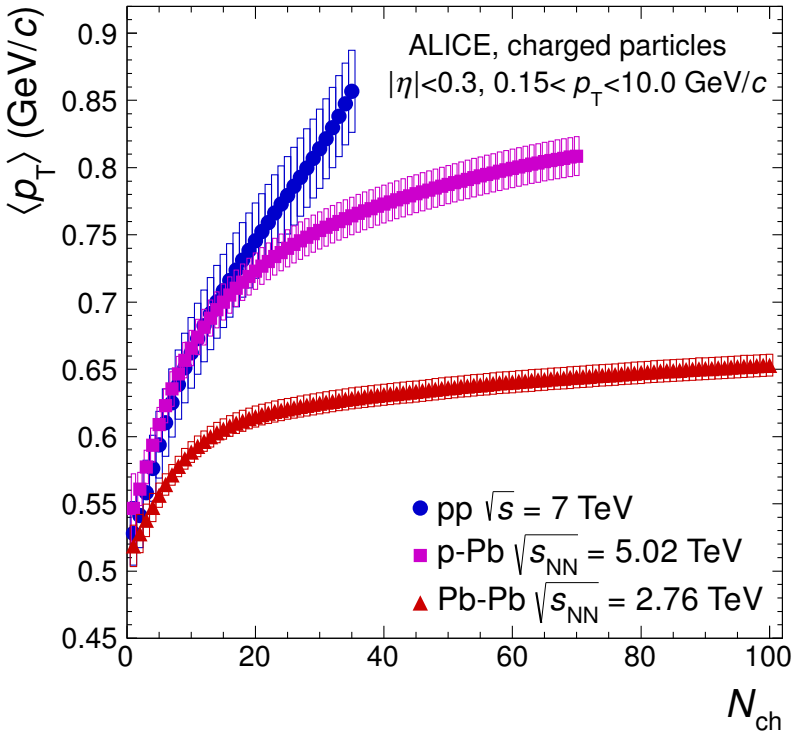

Figure 3.7: Comparison of average p_T for three different collision systems [ALICE|13d].

a comparison over the largest possible multiplicity range. For heavy-ion collisions, the energy dependence may differ, but the comparison of $\langle p_T \rangle$ measurements between CMS and STAR data in figure 1.13b indicates only a small collision energy dependence of $\langle p_T \rangle$.

The comparison of $\langle p_T \rangle$ as function of n_{ch} in figure 3.7 for three different collision systems shows a more versatile picture. Due to the low multiplicity in pp and p–Pb collisions, the multiplicity in Pb–Pb is limited to $n_{ch} = 100$, which corresponds to peripheral Pb–Pb collisions. A comparison of $\langle p_T \rangle$ as function of event multiplicity and $\langle p_T \rangle$ as function centrality can be found in [Mar|12].

For events with a multiplicity below $n_{ch} = 14$ the slopes of $\langle p_T \rangle$ in pp and p–Pb events agree with each other, while $\langle p_T \rangle$ for Pb–Pb events also have a linear rise in this multiplicity region, but with a smaller slope. Around $n_{ch} = 14$ in all three collision systems the gradient decreases. The significance of the modification varies between the three collision systems. For pp collisions, the change in slope is rather small, while p–Pb and Pb–Pb reveal a more pronounced change. The multiplicity range for pp and p–Pb is limited by the recorded statistics and reaches $n_{ch} = 35$ and $n_{ch} = 70$, respectively.

3.7 Recent developments and outlook

The results presented in this chapter show the status of the $\langle p_T \rangle$ analysis with the datasets from LHC run 1. In the meantime during LHC run 2 new data with more events and different collision energies was recorded. With the new data collected during LHC run 2 between 2015 and 2018 it is possible to repeat this analysis with a collision energy of 5.02 TeV in all three collision systems. The new data sets also includes pp and p–Pb data taken with a high-multiplicity trigger to increase the statistics in the high multiplicity region and offers the possibility of a comparison over a wider multiplicity range. With the higher multiplicity reach a study of the $\langle p_T \rangle$-flattening at high multiplicities could be possible. During run 2 also new heavy-ion data from Xe–Xe collisions was recorded and allows to compare the behaviour of $\langle p_T \rangle$ at high multiplicities for different heavy-ion collision systems. Additionally, the analysis could be repeated in different centrality selections to constrain the impact parameter of the collision. The result of such an analysis can be compared to the predictions shown in figure 1.12.

In Addition to the new data sets, better understanding of the detectors and using a Bayesian unfolding approach, as shown in [Krü|17], can improve the results of the measurement.

4 Isolated Photons

An analysis of isolated photons represents an experimental approach to measure prompt photons from $2 \rightarrow 2$ processes, as they cannot be distinguished from prompt photons of other sources. As described in section 1.5.2 theoretical calculations and predictions show that an isolation criterion significantly decreases the background contribution from fragmentation photons. The analysis strategy for isolated photons consists of the photon identification and the isolation criterion as the main constituents. This analysis is based on the $\mathcal{ABCD}$ method used by the ATLAS collaboration [ATLAS|11a]. It describes a combined approach between photon identification and background estimation. The analysis presented in this work is part of a common effort from different groups to publish the first isolated photon measurement by the ALICE collaboration [ALICE|19b]. The published result contains contributions from all analyses, including this one. In section 4.6 a comparison between the published results and the results of this analysis is shown.

4.1 Data Set

4.1.1 Experimental data

The experimental data for this measurement was recorded in 2011 and is one of the first data sets recorded with the EMCal trigger. The relevant data set consists of two subsets LHC11c and LHC11d, both recorded with a trigger threshold of 5.5 GeV. After the quality assurance on run conditions, EMCal and tracking performance, 41 runs from LHC11c with 4.51×10^6 events and 29 runs from LHC11d with 2.84×10^6 events are used in the analysis. In total, these runs contain 7.35×10^6 events. A detailed list of the run statistics can be found in Appendix B.

4.1.2 Monte Carlo simulations

The simulated data used in the analysis is composed of three different MC samples. For the description of signal events, the final state of the particle generator has to be a photon and a jet (γ-jet) and the

p_T hardbin	γ-jet MC (GeV/c)	jet-jet MC1 (GeV/c)	jet-jet MC2 (GeV/c)
1	5-11	5-7	10-14
2	11-21	7-9	14-19
3	21-36	9-12	19-26
4	36-57	12-16	26-35
5	57-84	16-21	35-48
6	84-117	21-∞	48-66
7			66-∞

Table 4.1: List of all p_T hardbins used for the three simulations.

photon has to point to the EMCal surface. The other two simulations are used to describe background events. In theses simulations, two jets (jet-jet) are required as final state of the particle generator. Additionally, a photon from a hadron decay has to be within the EMCal acceptance and needs at least an energy of 3.5 GeV or 7 GeV, respectively. In the analysis the signal and the background productions are combined (MC mixing) to obtain a dataset similar to the recorded data. To simulate enough statistics over the whole relevant p_T range, every simulation is split into multiple smaller simulations to reduce the needed computation time. In each sub-simulation (p_T hardbin) the kinematic range of the initial hard process in the simulation is limited. The corresponding limits are listed in table 4.1. To further reduce the needed computation time, only detector conditions from two runs for each period are used as reference point.

4.2 Analysis Strategy

Figure 4.1 shows the analysis strategy to obtain the cross-section of isolated photons. The processing steps are explained in more detail in the following sub-sections. Details about corrections and modifications specific to the analysis are explained in section 4.3.

4.2.1 Event selection

From all recorded events only events which pass certain quality criteria are used for the analysis. Only events recorded with an EMCal trigger are selected to enhance the number of high energetic clusters. The analysis requires at least one track to constrain the position of the collision vertex. A cut on the vertex position along the z-axis of 10 cm ensures a uniform acceptance of tracks and clusters in η in all detectors. Additionally, events with multiple collisions, so called

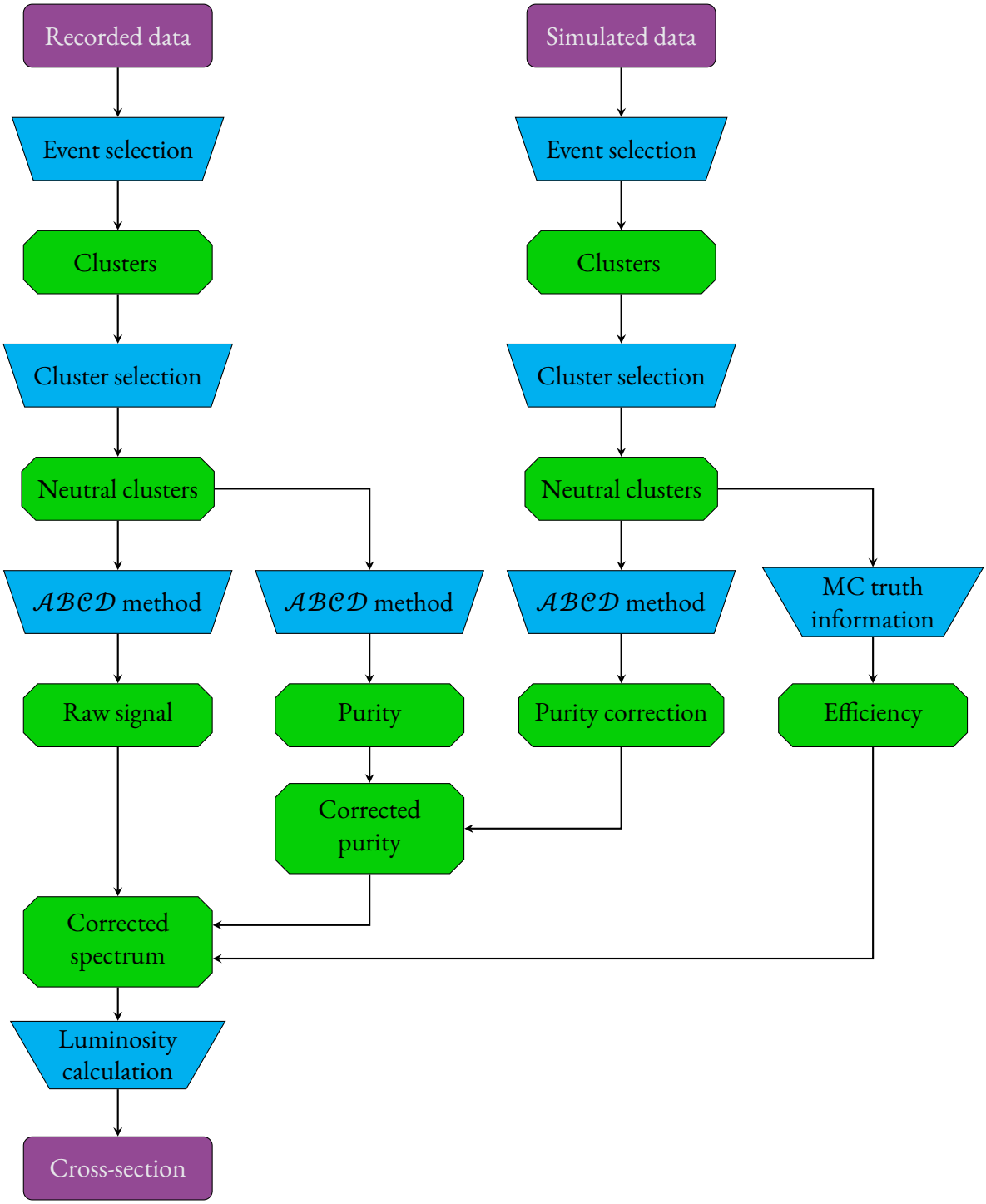

Figure 4.1: Schematic representation of the analysis strategy for isolated photons. The blue trapezia illustrate analysis steps, while the green octagons depict the resulting observables.

pile-up events, are rejected as it is not possible to distinguish the origin of photons.

4.2.2 Cluster selection

Similar to the event selection, clusters also need further selection. During the clustering process, clusters with exotic properties are removed. Subsequently, clusters are further selected on their properties.

First a cut on the cluster time is used to select only clusters of the corresponding collision. This is achieved by limiting the cluster time to -30 ns to 30 ns in respect to the bunch crossing. In the next step, all clusters consisting of at least two cells are selected. For the number of local maxima (NLM) a default cut of NLM ≤ 2 is applied. This rejects clusters created by jets, but still accepts clusters from merged π^0 or converted photons. To reject clusters from charged particles, the distance to the next track is calculated for each cluster. If the track lies within a range of $|\Delta\eta| \leq 0.1 + \left(p_{\mathrm{T}} + 4.07\right)^{-2.5}$ and $|\Delta\varphi| \leq 0.15 + \left(p_{\mathrm{T}} + 3.65\right)^{-2}$ around the cluster centre, where p_{T} stands for the track p_{T}, the cluster is expected to be of charged origin and is not handled as a photon candidate. In addition, every cluster centre needs to have a distance of at least two full EMCal cells to the next defective cell on EMCal. With the given distance the influence of bad cells to the cluster properties is minimized. In the last step, only clusters are accepted which have at least a distance of 0.4 in η and φ from the borders of EMCal. This fiducial cut is needed to completely take the contribution of neutral particles to the isolation cone around the cluster into account.

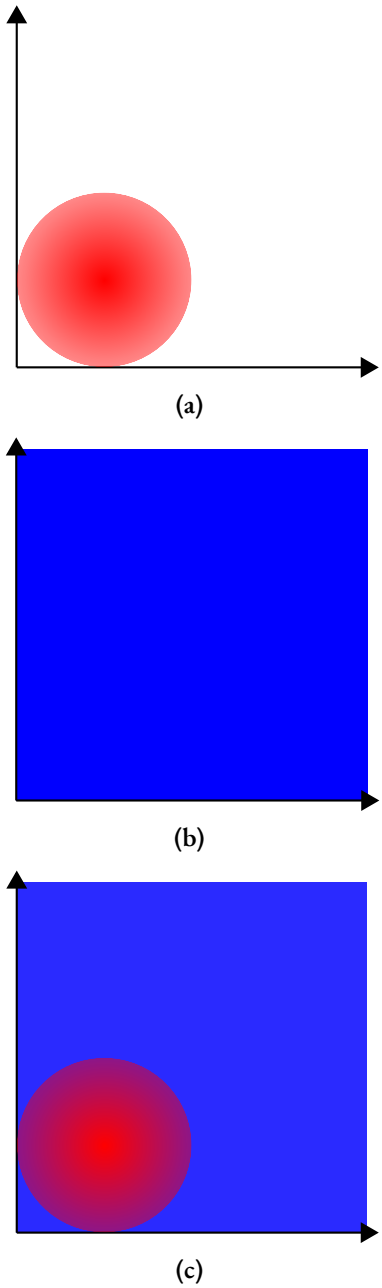

Figure 4.2: Sketch with ideal signal (a) and background (b) distribution and the combination (c) of both contributions.

4.2.3 $\mathcal{ABCD}$ method

The $\mathcal{ABCD}$ method uses the general assumption that the data sample consists of a mixed (signal + background) sample in a two dimensional parameter space. The signal is limited to a certain region in the space, while the background is distributed over a wider region including the signal region.

Figure 4.2 shows a simplified version of a signal and background contribution to an arbitrary parameter space. Sketch 4.2a shows the limited signal distribution, while the background in plot 4.2b is evenly distributed over the whole space. In the combined allocation in figure 4.2c, the signal region is still visible, but has an additional contribution from the background.

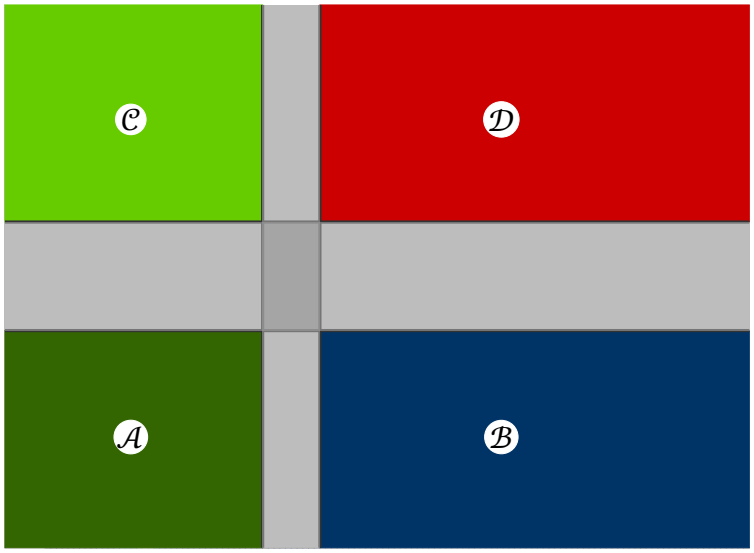

Figure 4.3: Sketch of the four regions used in the analysis and naming of the corresponding regions.

4.2.3.1 Observables

The observables for the $ABCD$ method are chosen to distinguish prompt photons from background contributions. As mentioned in this chapter's introduction, an isolation criterion ($E_{\mathrm{T_{iso}}}$) helps to distinguish prompt photons from fragmentation photons. The criterion is defined by the energy of all particles inside a cone with radius $R = 0.4$ around the photon cluster ($^{\gamma}$), with

$$R = \sqrt{(\eta - \eta^{\gamma})^2 + (\varphi - \varphi^{\gamma})^2}. \tag{4.1}$$

The discrimination of background from photons from particle decays, depends on the mass and energy of the mother particle. The low mass of the most relevant particle decays ($\pi^0 \rightarrow \gamma + \gamma$ and $\eta \rightarrow \gamma + \gamma$) results in small opening angles for high-energetic particles and thus in merging of the two clusters from the decay photons. These clusters can be identified by the cluster variable σ^2_{long}. For lower particle energies, the second decay photon will not merge, but will lie inside the isolation radius. Thereby, the primary photon will be rejected by the isolation criterion. Particle decays with larger opening angles can be neglected, as the energy of the decay photons is below the measured energy range or can be ignored due to their rareness.

The parameter space of $E_{\mathrm{T_{iso}}}$ and σ^2_{long} is not distributed uniformly as shown in figure 4.4. To account for this inhomogeneity, the parameter space is grouped into four regions, by dividing each parameter into two ranges, as depicted in figure 4.3. To better discriminate between the four regions and reduce the contamination, gaps are

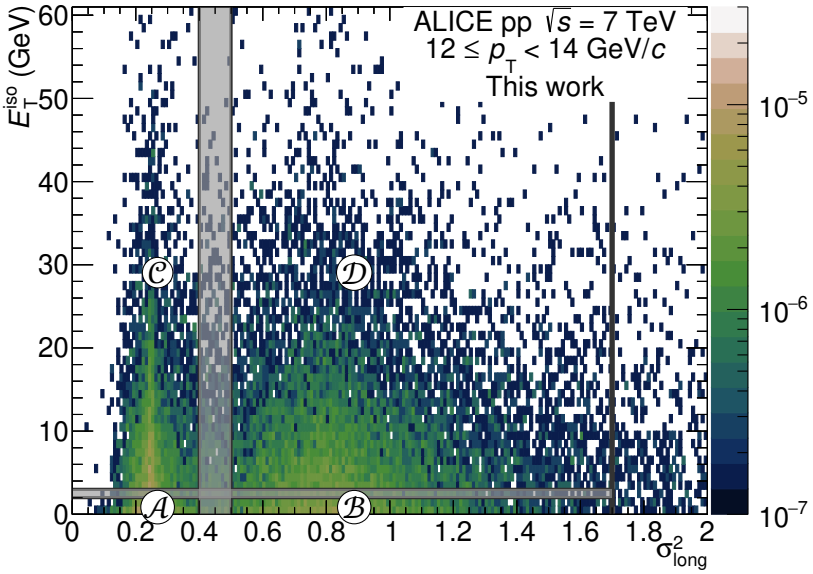

Figure 4.4: Regions in the p_T bin between 12 GeV/c and 14 GeV/c.

Region	Isolation criterion	Cluster shape
$\mathcal{A}$	fulfilled	γ-like (narrow)
$\mathcal{B}$	fulfilled	π^0-like (wide)
$\mathcal{C}$	not fulfilled	γ-like (narrow)
$\mathcal{D}$	not fulfilled	π^0-like (wide)

Table 4.2: Comparison of the four regions.

used to separate the regions. For γ-like and π^0-like clusters, this is especially important at higher energies, where both of the cluster shapes start to have a similar shape. The boundaries of the two parameters are chosen such that the following two assumptions are fulfilled: First, apart from region $\mathcal{A}$, the contribution by the signal is negligible. Second, the distribution between isolated and non-isolated background clusters is independent of the cluster shape. The four regions can be described as follows: region contains the signal and fulfils both criteria, in regions $\mathcal{B}$ and $\mathcal{C}$, either the criterion on σ^2_{long} or $E_{\text{T}_{\text{iso}}}$ is not fulfilled, respectively. In region $\mathcal{D}$ neither of the two criteria apply. In table 4.2 the properties of the four regions are summarized.

4.2.3.2 Signal extraction

The aforementioned classification of the parameter space allows for the extraction of the signal from the mixed region. Mathematically, the limitation of the signal to region A can be described in the following way:

$$B_{\mathcal{B},\mathcal{C},\mathcal{D}} = N_{\mathcal{B},\mathcal{C},\mathcal{D}} \tag{4.2}$$

$$S = S_{\mathcal{A}} = N_{\mathcal{A}} - B_{\mathcal{A}} \tag{4.3}$$

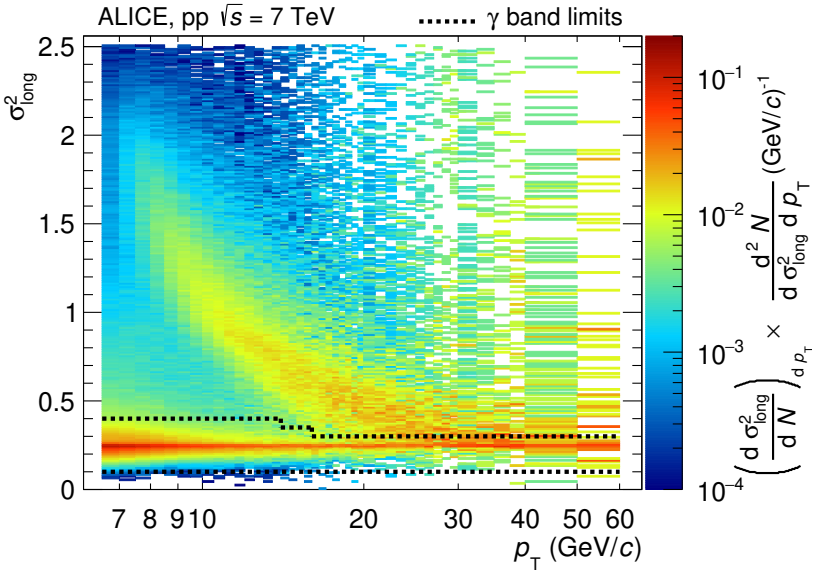

Figure 4.5: Energy dependence of cluster shape (σ^2_{long}) for photon-like clusters and clusters from merged π^0 and their corresponding bands. [ALICE|19b]

Where N represents the total number of entries in the corresponding region ($_{\mathcal{A},\mathcal{B},\mathcal{C},\mathcal{D}}$), which can be split into contributions from the signal (S) and the background (B). Due to the lack of contributions from the signal, in regions $_{\mathcal{B},\mathcal{C},\mathcal{D}}$ the number of entries equals the number of background entries. The assumption of a cluster-shape-independent distribution of background clusters yields to the following expression:

$$\frac{B_{\mathcal{A}}}{N_{\mathcal{C}}} = \frac{N_{\mathcal{B}}}{N_{\mathcal{D}}} \tag{4.4}$$

By solving formula 4.4 for $B_{\mathcal{A}}$ and substituting the result in formula 4.3 one obtains:

$$S = N_{\mathcal{A}} - \frac{N_{\mathcal{B}} \cdot N_{\mathcal{C}}}{N_{\mathcal{D}}} \tag{4.5}$$

Equation 4.5 allows for the calculation of the prompt photon yield in a data driven way, based on the aforementioned two assumptions.

For the region limits, a constant value is chosen for $E_{\text{T}_{\text{iso}}}$ and a value shifting with p_{T} is selected for σ^2_{long}. The shifting limit is necessary as the opening angle of particle decays changes with the energy of the mother particle. The borders for σ^2_{long} are adapted accordingly. In figure 4.5, the change of the cluster parameter σ^2_{long} with increasing energy is visible. In the lower region, the constant band corresponds to single photons. The curved trend of the upper band arises from the energy dependence of the opening angle of decay photons. In EMCal the cluster merging for π^0 starts at energies of approximately 8 GeV. With increasing energy, the cluster shape alters and

appears more like single photons. As such, it gets more difficult to distinguish the two cluster types and the σ^2_{long} criterion needs to be adapted with increasing energy, indicated by the dotted lines.

4.2.3.3 Purity estimation

The results from the signal extraction can be used to calculate the purity (p) of the signal region.

$$p = \frac{S_{\mathcal{A}}}{N_{\mathcal{A}}} = 1 - \frac{B_{\mathcal{A}}}{N_{\mathcal{A}}} \tag{4.6}$$

$S_{\mathcal{A}}$ in the purity definition for region $\mathcal{A}$ can be replaced by the results of equation 4.5 to achieve the following result:

$$p = 1 - \frac{N_{\mathcal{B}} \cdot N_{\mathcal{C}}}{N_{\mathcal{A}} \cdot N_{\mathcal{D}}} \tag{4.7}$$

4.2.3.4 Purity correction

The assumption of identical isolation probabilities, described in the beginning of this section, does not withstand a closer investigation due to two effects. In the low energetic regime, two photons from a π^0 decay can either produce an elongated cluster with no contribution to the isolation cone or produce a γ-like cluster with a contribution to the isolation cone energy from the second decay photon. Thus, the isolation probability differs for signal and background clusters.

While this is negligible for high-energetic photons, clusters with multiple contributions (MCC) show an additional p_{T} dependent behaviour. These clusters are generally produced in a jet like environment that produces clusters with large elongated shapes. The origin of these clusters entails an additional contribution to the energy inside the isolation cone from the correlated jet. Thus, background clusters at high energies have a lower isolation probability compared to signal clusters at the same energy.

To correct for these effects, a correction factor α is multiplied to equation 4.7.

$$p = 1 - \left(\frac{N_{\mathcal{B}} \cdot N_{\mathcal{C}}}{N_{\mathcal{A}} \cdot N_{\mathcal{D}}}\right) \cdot \alpha \tag{4.8}$$

By expanding equation 4.8 with $\frac{B_\mathcal{A}}{B_\mathcal{A}}$ the purity can be rewritten as:

$$p = \overbrace{1 - \frac{B_\mathcal{A}}{N_\mathcal{A}} \cdot \underbrace{\frac{N_\mathcal{B} \cdot N_\mathcal{C}}{B_\mathcal{A} \cdot N_\mathcal{D}} \cdot \alpha}_{\Rightarrow 1}}^{p} \tag{4.9}$$

The new purity definition consist of two parts. The first part matches the purity definition from equation 4.6. Accordingly, the second part has to be equal to 1 for the formula to remain valid. Consequentially, α can be defined with the reciprocal value:

$$\alpha = \left(\frac{1}{\frac{N_\mathcal{B} \cdot N_\mathcal{C}}{B_\mathcal{A} \cdot N_\mathcal{D}}} \right) = \left(\frac{B_\mathcal{A} \cdot N_\mathcal{D}}{N_\mathcal{B} \cdot N_\mathcal{C}} \right) \tag{4.10}$$

As $B_\mathcal{A}$ cannot be measured in data, the correction factor can be extracted from MC as long as the assumption

$$1 = \frac{\alpha_{\text{MC}}}{\alpha_{\text{data}}} \tag{4.11}$$

holds.

Replacing α in equation 4.8 with the definition from equation 4.10, one gets the final definition of the corrected purity:

$$p = 1 - \left(\frac{N_\mathcal{B} \cdot N_\mathcal{C}}{N_\mathcal{A} \cdot N_\mathcal{D}} \right)_{\text{data}} \times \left(\frac{B_\mathcal{A} \cdot N_\mathcal{D}}{N_\mathcal{B} \cdot N_\mathcal{C}} \right)_{\text{MC}} . \tag{4.12}$$

A caveat of this method is the dependency on the reliability of the simulations and especially of the MC mixing. While the simulations are improved continuously, the mixing uses a rather simplistic approach. As it will be shown in the systematic calculation for the mixing ratio in section 4.5.6, the mixing ratio contributes only a small part to the total systematic uncertainty. Therefore, there is no need to modify the mixing technique any further.

Due to differences between recorded data and simulations additional corrections are needed. These will be discussed in section 4.3.8.1.

4.2.4 MC truth information

The MC truth information is required to calculate the efficiency ϵ of the measurement process. For this purpose, the dedicated MC production of pp collisions with γ-jet events is used. The only background in these events originates from the underlying

event. Accordingly, the signal in region A is not contaminated with background from jets. For the efficiency calculation, the signal in region A is calculated twice. Once with the reconstructed values of the MC production ($N_{\mathcal{A}}^{\text{rec}}$) and once with values from the generator level ($N_{\mathcal{A}}^{\text{gen.}\gamma}$). For the latter case, only clusters which originate from an isolated photon are taken into account as signal, resulting in

$$\epsilon = \frac{N_{\mathcal{A}}^{\text{rec}}}{N_{\mathcal{A}}^{\text{gen.}\gamma}}. \tag{4.13}$$

4.3 Analysis Results

After the explanation of the analysis strategy in section 4.2, in the following section this strategy is applied on the selected data sets. The results of the intermediate steps, as well as the final result are presented. Additionally, adaptions to the analysis strategy resulting from the intermediate results are discussed.

4.3.1 Run selection

Apart from the beam conditions and the EMCal performance also the TPC conditions play a crucial role for the analysis. Non stable TPC conditions in the vicinity of the EMCal would affect the charge particle veto as well as the energy calculation in the isolation cone. During the TPC QA only one parameter was found to be unstable in the two periods. In 15 runs not all sectors of the TPC were active. The two figures in figure 4.6 show two exemplary runs, with all sectors active (a) and with inactive sectors (b). Due to the location of the inactive channel in front of the EMCal acceptance all runs with inactive channels were rejected from the further analysis.

4.3.2 Event selection

From the three different event cuts (vertex cut, pile-up rejection and the minimum requirement of one track) only the vertex cut significantly rejects events. About 9 % of the events are discarded by the vertex cut, as shown in figure 4.7. The other two cuts only have a marginal effect. In total 6.78×10^6 events pass all cuts and are further used in the analysis.

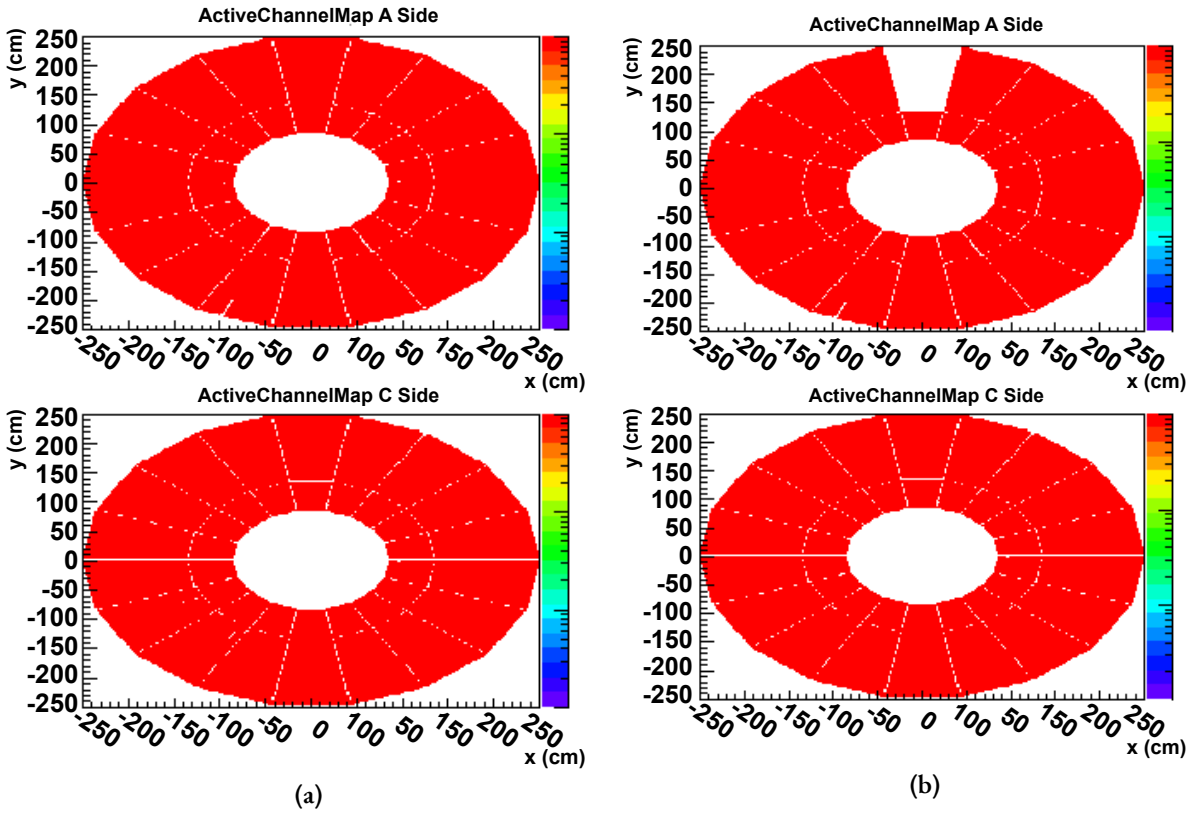

Figure 4.6: Active channels in the TPC for run 159582 (a) and run 158285 (b).

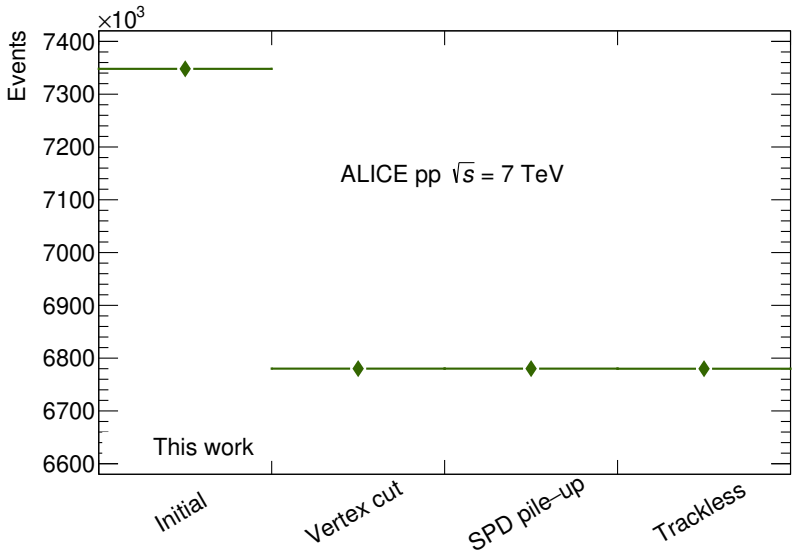

Figure 4.7: Number of events after each step of event cuts.

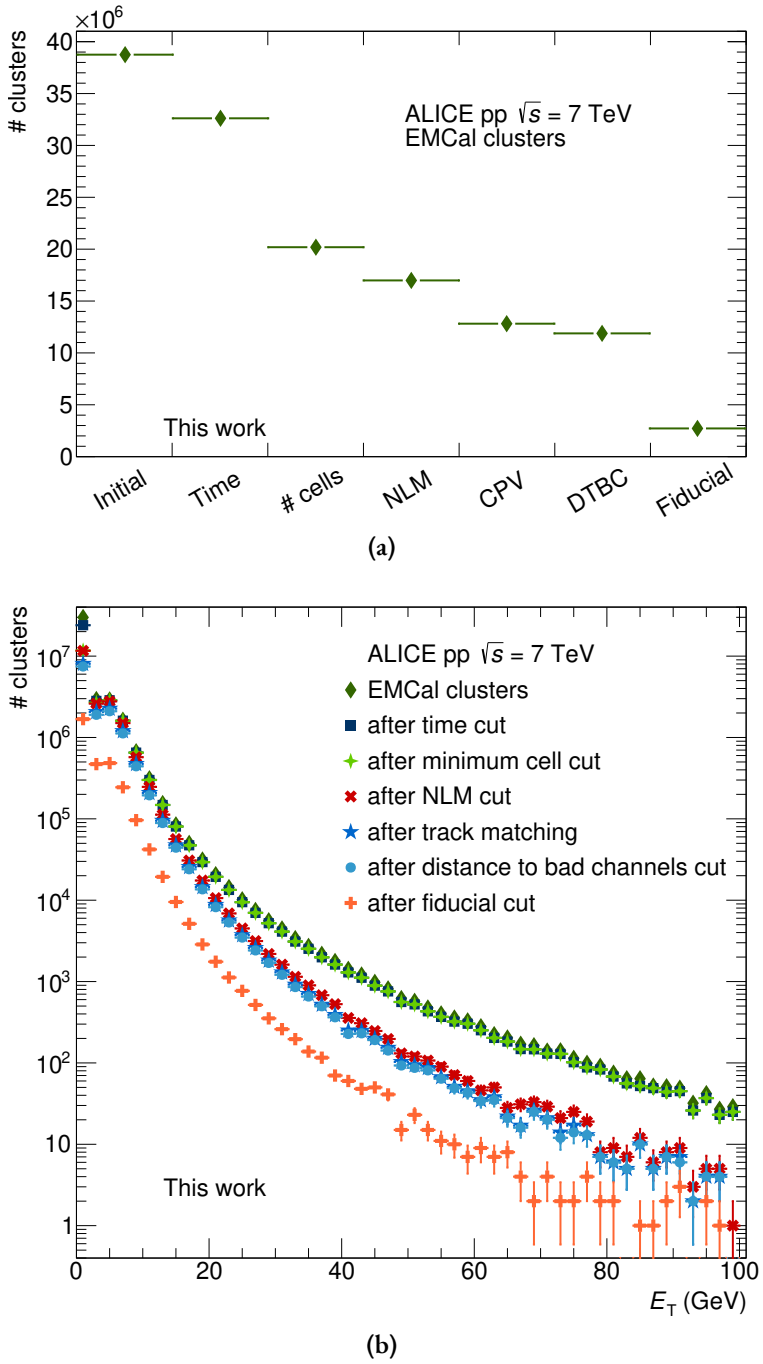

Figure 4.8: Number of clusters after each cluster cut (a) and the corresponding cluster spectra (b).

4.3.3 Cluster selection

In comparison to the event cuts, cluster cuts not only change the number of clusters, but also modify the E_T spectrum of the clusters. The results of the cluster selection are shown in figure 4.8. Figure 4.8a shows the total rejection for all cuts, while in figure 4.8b also the modification of the E_T spectrum is shown. Overall nearly 90 % of all clusters are rejected by the different cuts. Even if only clusters above 10 GeV are taken into account as potential isolated photon candidates, also clusters below are relevant as contributors to the energy in

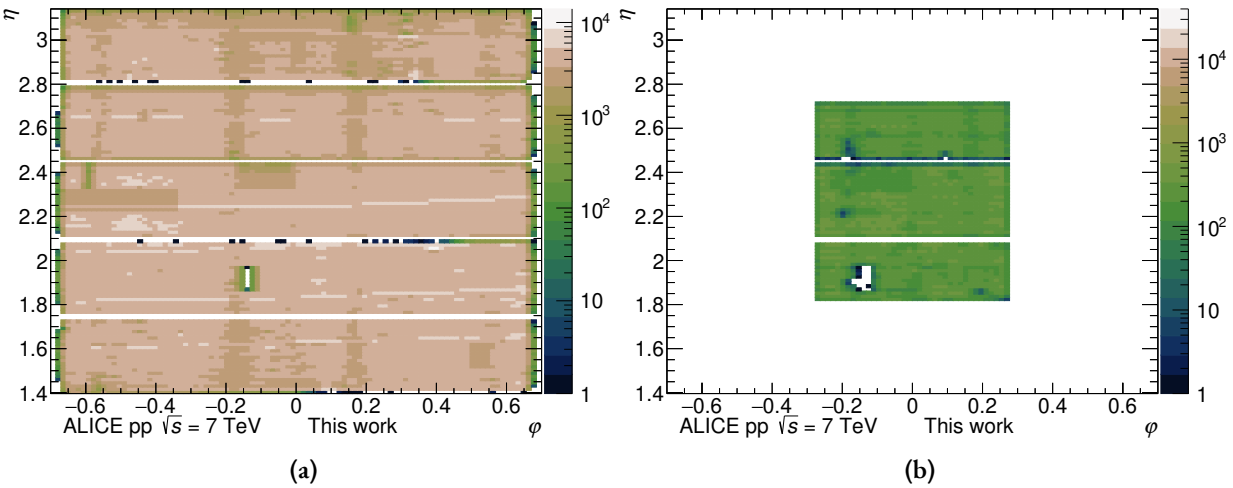

Figure 4.9: Cluster distribution of all clusters on EMCal before (a) and after all cluster cuts (b).

the isolation cone. The cut on the cluster time together with the cut on the minimum number of cells reject nearly half of all clusters. While the time cut effects clusters of all energies, the requirement on the number of cells predominantly effects clusters at low energies. The opposite behaviour regarding the energy dependence can be observed at the selection on the number of local maxima (NLM). This correlation is expected as clusters with many NLM are correlated to high-energetic particle jets. The charge particle veto (CPV) influences the spectrum over the whole energy, while the effect of the distance to bad cells (DTBC) is nearly negligible. Finally, the fiducial cut reduces the number of clusters by ~ 75 %. As shown on the E_{T} spectrum, the number of high energetic clusters is drastically reduced. Due to the limited statistics only clusters with less than 60 GeV are further taken into account for the analysis. In figure 4.9, the cluster distribution over the complete EMCal surface is shown, before (a) any cuts and after all aforementioned cuts are applied (b). Apart from the fiducial cut, also the reduction of the number of clusters in the selection region is clearly visible (scale on the z-axis is identical in both plots). The horizontal stripes correspond to the edges of the EMCal supermodules. The patterns in the active area originate from runs where certain regions of EMCal did not work properly and are marked as bad. All clusters passing all selection criteria are handled as photon candidates, while clusters which are rejected by the NLM or the fiducial cut are contributing to the energy in the isolation cone.

	signal σ^2_{long} region limits		background region limit	
p_{T} range	lower σ^2_{long}	upper σ^2_{long}	lower σ^2_{long}	upper σ^2_{long}
10 - 12	0.1	0.4	0.55	1.75
12 - 14	0.1	0.4	0.5	1.7
14 - 16	0.1	0.35	0.45	1.65
16 - 18	0.1	0.3	0.4	1.6
18 - 20	0.1	0.3	0.4	1.6
20 - 25	0.1	0.3	0.4	1.6
25 - 30	0.1	0.3	0.4	1.6
30 - 40	0.1	0.3	0.4	1.6
40 - 60	0.1	0.3	0.4	1.6

Table 4.3: p_{T} binning used for the analysis with the corresponding σ^2_{long} thresholds.

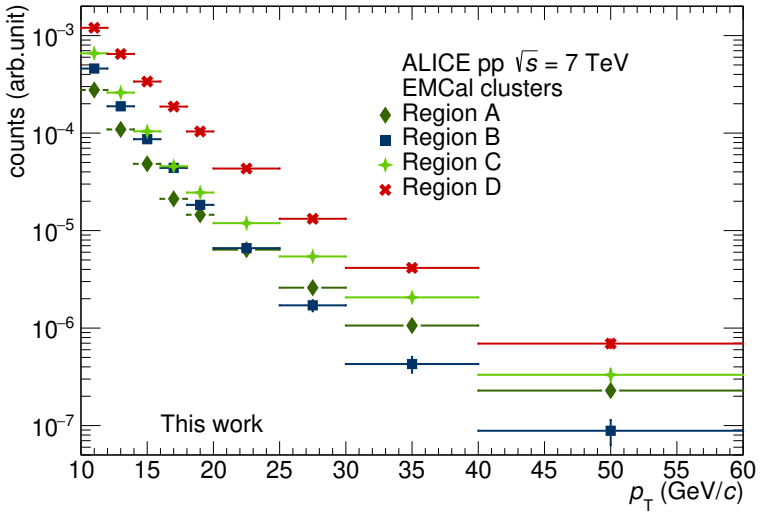

Figure 4.10: p_{T} spectra for all four regions of the $\mathcal{ABCD}$ method.

4.3.4 Raw signal

The thresholds to define the regions of the $\mathcal{ABCD}$ method are chosen to provide stable conditions for the differentiation of the four regions over the full p_{T} range. For the isolation criteria a gap from 2 GeV to 3 GeV is selected as energy threshold to distinguish between isolated and non-isolated clusters. In table 4.3 the changing values for the σ^2_{long} cut and the related gap are shown.

With the above mentioned specifications of cut values in the parameter space, the content of the regions $\mathcal{A}$, $\mathcal{B}$, $\mathcal{C}$, and $\mathcal{D}$ can be calculated. In figure 4.10 the p_{T} distribution for all four regions is plotted. The four spectra show a similar behaviour with a strong decrease over the full p_{T} range.

Additionally, the spectrum of the signal region $\mathcal{A}$ solely is shown in figure 4.11. For the low p_{T} part an exponential behaviour is visible and a power law dependency for the high p_{T} part. The transition occurs between 15 GeV/c and 20 GeV/c.

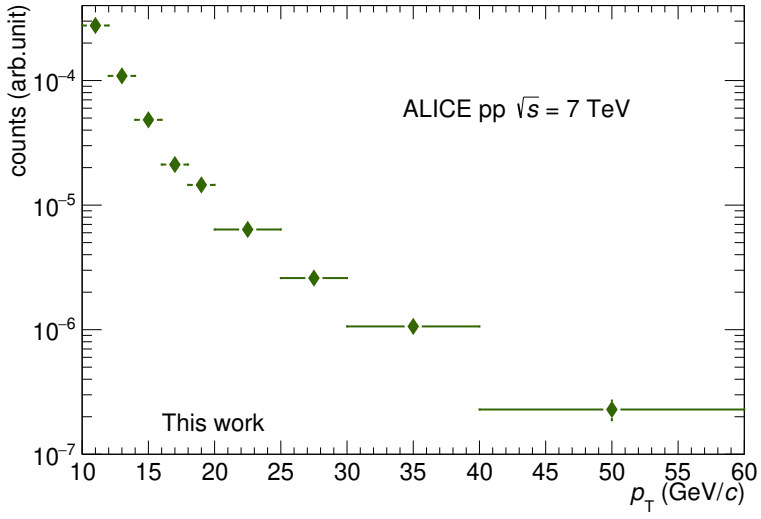

Figure 4.11: p_T spectrum of region $\mathcal{A}$, containing signal and background contributions.

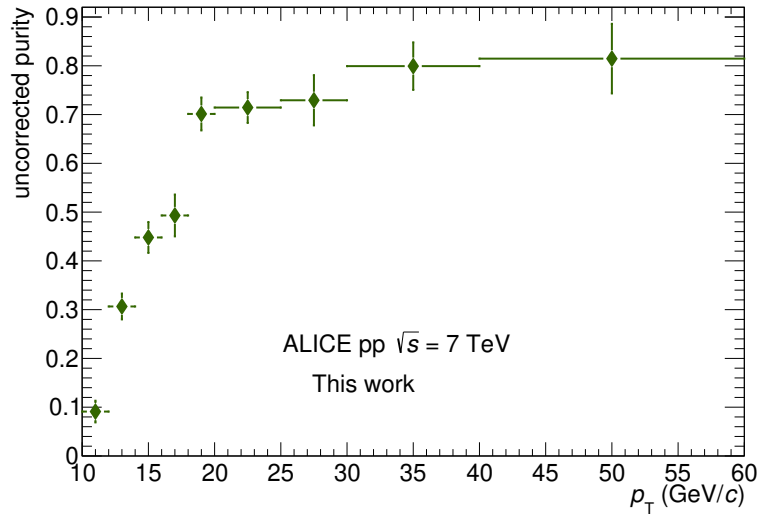

Figure 4.12: Uncorrected purity.

4.3.5 Purity

The data-driven purity extracted by applying equation 4.7 is shown in figure 4.12. It increases from 7 % for the lowest p_T bins to ~ 70 % at intermediate p_T and further to 80 % in the high momentum region.

This increase can be explained by a combination of physics and detector effects. Physics-wise the probability to find a high energetic isolated cluster decreases with E_T, due to the increasing probability of accompanying particles. Additionally, the detector layout limits the determination of photons from high-energetic π^0 and single photons, as the cluster shape gets indistinguishable above 40 GeV/c. The same effect is responsible for the high contamination at low p_T and confines the lower p_T limit of the analysis.

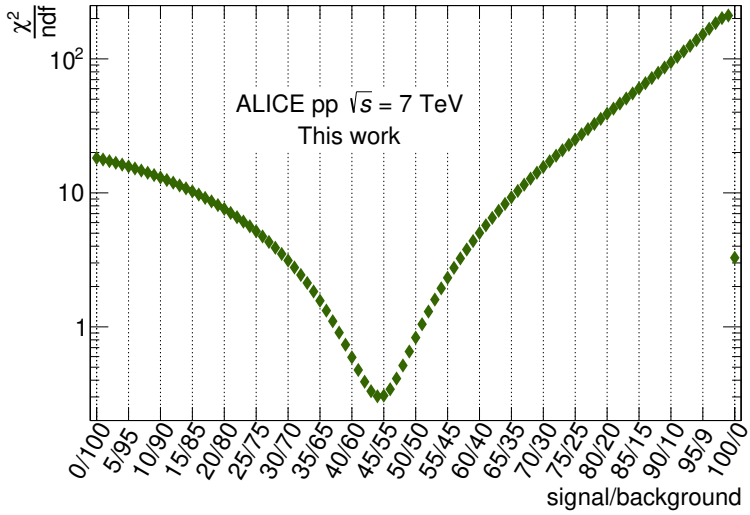

Figure 4.13: χ^2 distribution for different mixing ratios.

4.3.6 Corrected purity

For the reasons described in section 4.2.3.4 a correction is required for the purity described above. The correction factor α needed for the purity correction is extracted from simulations as shown in equation 4.12. As mentioned before, background and signal simulations are produced in separate steps and are mixed for the analysis. For the mixing, each simulation is scaled with an individual factor and the sum of both factors is fixed to 1. To determine the appropriate factors for the two MC productions, the purity for different mixing ratios is calculated and compared to the purity calculated in data. The χ^2 value of each variation is shown in figure 4.13. The best agreement is found for a mixing ratio of 0.44 for the signal simulation and 0.56 for the background simulation.

The corresponding correction factor α is plotted in figure 4.14a. It shows a near linear rise from ~ 0.8 for the lowest momentum to 1.8 for the highest momenta. The resulting corrected purity shows a higher purity of about 0.25 for the low p_T region and a plateau of about 0.68 above 18 GeV/c, as depicted in figure 4.14b. Compared to the uncorrected spectra, the trend has not changed but the spread over the whole p_T range is reduced.

4.3.7 Efficiency

Compared to the purity the efficiency in figure 4.15 shows no clear p_T dependence and varies by 4 %. For the lowest and highest bins, the efficiency is about 0.61. In between, the efficiency decreases to 0.575.

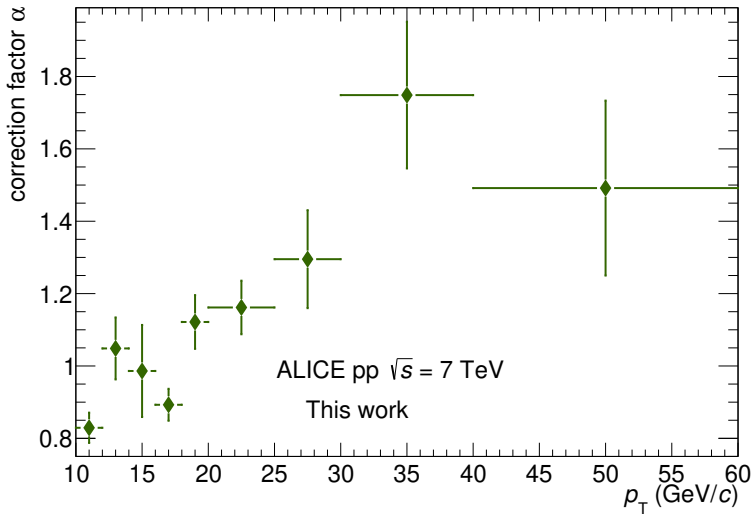

(a)

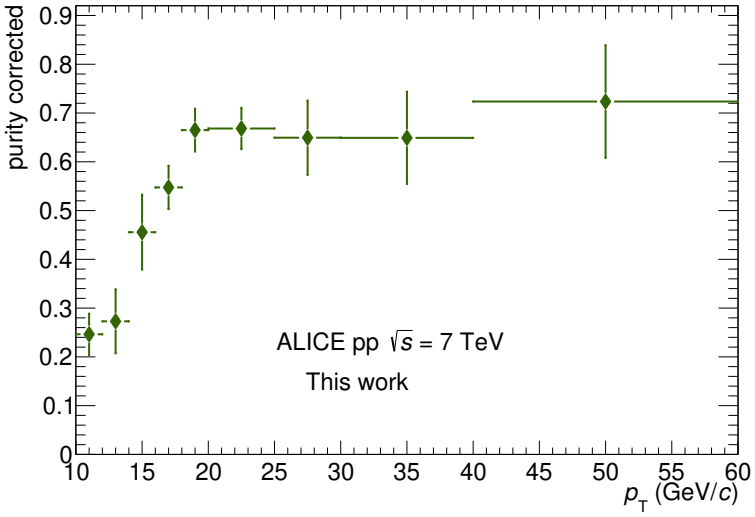

(b)

Figure 4.14: Correction factor α (a) and the resulting corrected purity (b).

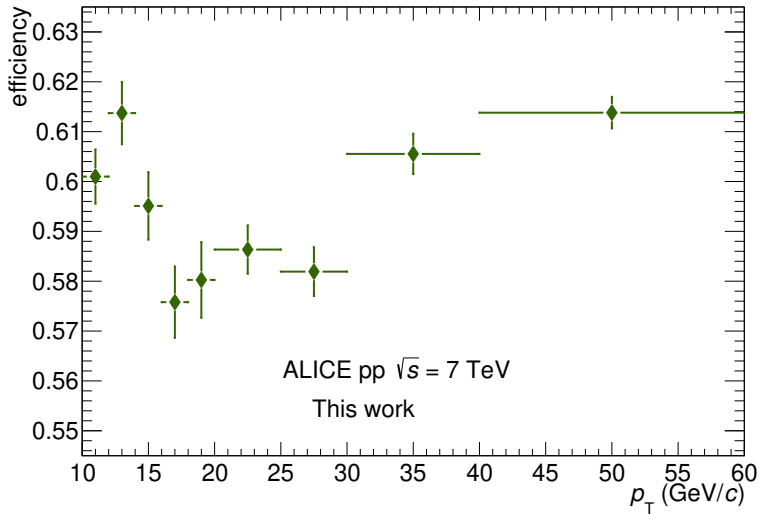

Figure 4.15: Efficiency extracted from the MC on the generator level of the γ-jet simulation.

4.3.8 Further corrections

4.3.8.1 Simulation bias

By using simulations for corrections an additional source of uncertainty is introduced to the data-driven purity estimation. If the assumption in equation 4.11 is not fulfilled, an additional bias is introduced into the corrected purity. By comparing the σ^2_{long} ratio of isolated and non-isolated distributions between recorded data and simulations the difference between simulation and recorded data can be estimated. The comparison can be described by the function

$$f\left(\sigma^2_{\text{long}}\right) = \frac{\left(\frac{N_{\text{iso}}}{N_{\overline{\text{iso}}}}\left(\sigma^2_{\text{long}}\right)\right)_{\text{data}}}{\left(\frac{N_{\text{iso}}}{N_{\overline{\text{iso}}}}\left(\sigma^2_{\text{long}}\right)\right)_{\text{MC}}}. \tag{4.14}$$

Due to the statistical limitations the comparison is performed only in two p_{T} regions: One, where γ-like clusters and clusters from merged π^0 are still distinguishable ($p_{\text{T}} < 16\,\text{GeV/c}$) and one, where the clusters are fully merged ($p_{\text{T}} \geq 16\,\text{GeV/c}$).

To estimate a possible σ^2_{long} discrepancy of background clusters between data and MC, multiple fits are performed in the background region of the double ratio. The results of the fits for a linear and an exponential function and their confidence intervals are compared to a constant fit. A constant offset would not require an additional correction, as the correction factors would cancel each other.

The results for all three functions are shown in figure 4.16. The bold part of the different functions represents the fitting range and the patterns in the same colour the corresponding confidence intervals. For the lower p_{T} region the linear and the exponential function have a small slope and are in agreement with the constant fit. In the higher p_{T} regime, the linear and the exponential function show a gradient different from the constant fit. Even so, the confidence interval of the constant function is completely covered by the confidences intervals of the other two functions. Hence, no correction is applied to the standard procedure, but the correction by the linear and the exponential function are taking into account as contributions to the total systematic uncertainties (details can be found in section 4.5.5).

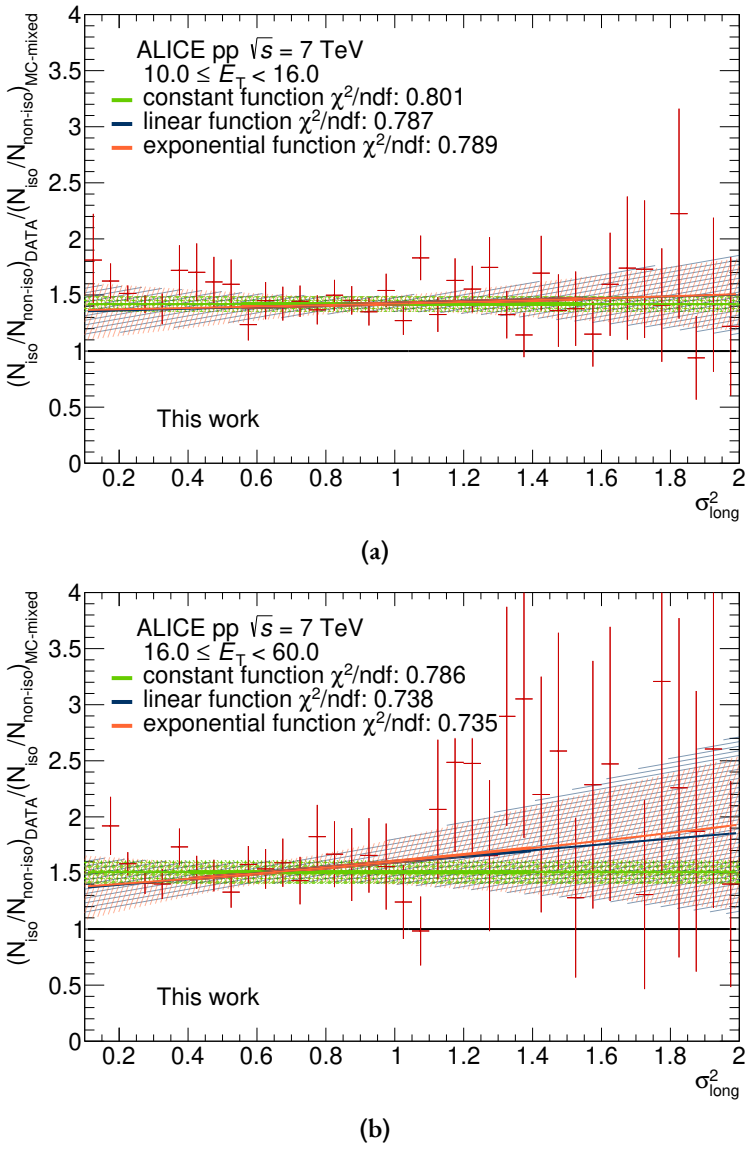

Figure 4.16: Double ratio of isolated over non-isolated photons in recorded data and MC simulations, for the low p_T region (a) and the high p_T region (b).

4.3.8.2 Trigger timing

During the clusterizing process for each cluster a time information is stored. The time of the highest energetic cell in the cluster is taken as time for the whole cluster. For both periods the timing of the clusters was not fully synchronised with the timing of the bunch crossing. As a result, the time information in some clusters is about 50 ns off from the calibrated time. The corresponding timing distribution against the cluster energy is shown in figure 4.17. The time distribution consists of two distinct peaks: One around 0 ns and one at 50 ns. For both peaks no energy dependence in the time distribution is visible.

Due to the timing cut of ±30 ns, described in section 4.2.2, the clusters in the 50 ns peak are rejected. To correct for the missing

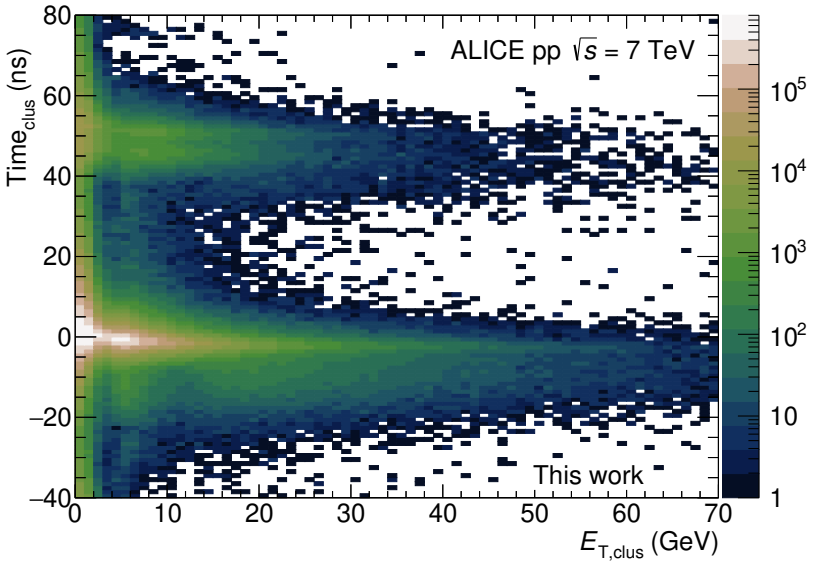

Figure 4.17: Time distribution of EMCal clusters as a function of cluster energy.

clusters, the correction factor $\mathscr{C}$ is used. It is defined as ratio of all clusters within the analysis timing cut over all cluster within a timing cut of −30 ns to 70 ns:

$$\mathscr{C}(p_{\mathrm{T}}) = \frac{N_{\mathrm{clust}}\,(-30\,\mathrm{ns}, +30\,\mathrm{ns})}{N_{\mathrm{clust}}\,(-30\,\mathrm{ns}, +70\,\mathrm{ns})} \tag{4.15}$$

The correction factor is calculated in the p_{T} ranges used for the analysis. $\mathscr{C}$ has a clear p_{T} dependence from low p_{T} to high p_{T} with values of 0.96 to 0.92, respectively.

4.3.8.3 Trigger efficiency

Even though the clusters used in the analysis are not affected by the trigger turn-on, the efficiency can be influenced by other effects of the EMCal. [1] To study the general trigger efficiency, the number of clusters with more than 10 GeV are counted in the minimum bias triggered data as well as the EMCal triggered data sample. The resulting trigger efficiency $\epsilon^{\mathrm{trigg}}$ is calculated as the ratio of both values, using the minimum bias sample as denominator. The resulting efficiency is found to be 0.90 ± 0.06. A value smaller 1 is expected, because the trigger acceptance is smaller than the full EMCal acceptance.

1: As the trigger does not use the fully calibrated readout signal, the turn-on has a continuous onset around the trigger threshold. Thus, only clusters with a certain energetic gap to the trigger threshold can be assumed as unaffected by the turn-on.

4.3.9 Luminosity calculation

The integrated luminosity for the data sample is needed to calculate the isolated photon cross-section. The luminosity for EMCal L0

triggered data can be expressed in the following way:

$$\mathscr{L} = \frac{N_{\text{evt}} \cdot P_{\text{EMC-L0}}}{\sigma_{\text{EMC-L0}}} \tag{4.16}$$

with the number of recorded events N_{evt}, pile-up correction factor $P_{\text{EMC-L0}}$ and the cross-section for the triggered data $\sigma_{\text{EMC-L0}}$. Due to the rareness of the EMC-L0 trigger, pile-up correction $P_{\text{EMC-L0}}$ can be assumed to be unity. In the modified formula

$$\mathscr{L} = \frac{N_{\text{evt}}}{\sigma_{\text{EMC-L0}}} \tag{4.17}$$

only $\sigma_{\text{EMC-L0}}$ is not known. In the periods LHC11c and LHC11d, no cross-section was measured for the EMCal triggered subsets and must be derived from the known cross-section of INT7 triggered data, using

$$\sigma_{\text{EMC-L0}} = \frac{\sigma_{\text{INT7}} \cdot R_{\text{EMC-L0}}}{P_{\text{INT7}}}, \tag{4.18}$$

where σ_{INT7} is the INT7 cross-section, $R_{\text{EMC-L0}}$ the rejection factor of the EMC-L0 trigger, and P_{INT7} the pile-up correction factor. The pile-up correction can be calculated from the probability that two protons have a collision in a bunch crossing. This probability is given by a Poisson law, because the probability for each collision in a bunch crossing is independent of each other, accordingly the probability for n collisions in a bunch crossing can be described as

$$P(X = n) = e^{-\mu} \cdot \frac{\mu^n}{n!}. \tag{4.19}$$

With μ as the average number of collisions in a bunch crossing. The average number of collisions corresponds to P_{INT7} and can be calculated as:

$$P_{\text{INT7}} = \frac{\sum_{n=1}^{\infty} n \cdot P(X = n)}{P(X \geq 1)}. \tag{4.20}$$

The probability for at least one collision $P(X \geq 1)$ can be computed with:

$$P(X \geq 1) = 1 - P(X = 0) = 1 - e^{-\mu}. \tag{4.21}$$

Equation 4.20 and 4.21 combine to:

$$P_{\text{INT7}} = \frac{\mu}{1 - e^{-\mu}} \tag{4.22}$$

$P(X \geq 1)$ can be further determined by the L0b trigger rate of the INT7 trigger $\left(R_{\mathrm{L0_b^{INT7}}}\right)$, the number of not-masked bunch crossings per orbit of the LHC (nBC_{orbit}), and the LHC frequency (ν_{LHC}):

$$P(X \geq 1) = \frac{R_{\mathrm{L0_b^{INT7}}}}{nBC_{\mathrm{orbit}} \times \nu_{\mathrm{LHC}}} \tag{4.23}$$

Now μ can be calculated by setting equation 4.21 and 4.23 equal.

$$\mu = -\ln\left(1 - \frac{R_{\mathrm{L0_b^{INT7}}}}{nBC_{\mathrm{orbit}} \times \nu_{\mathrm{LHC}}}\right) \tag{4.24}$$

Furthermore, the rejection factor $R_{\mathrm{EMC-L0}}$ can be extracted from the data for each period. With the knowledege of the luminosity, the differential cross-section for isolated photons can be calculated as:

$$\frac{d^2\sigma_{\gamma_{\mathrm{iso}}}}{dE_{\mathrm{T}}d\eta} = \frac{N_{\mathrm{evt}}}{\mathscr{L} \cdot \epsilon^{trigg}} \cdot \frac{d^2N^{\mathrm{iso}}}{N_{\mathrm{evt}}dE_{\mathrm{T}}d\eta} \cdot \frac{p\,(E_{\mathrm{T}})}{\epsilon\,(E_{\mathrm{T}})} \tag{4.25}$$

For the luminosity calculation N_{evt} and $\sigma_{\mathrm{EMC-L0}}$ are needed. The latter can be calculated following equation 4.18. A value of (53.7 ± 1.9) mb is measured for σ_{INT7} for the 2011 data [ALICE|14] and the averaged value for $\frac{R_{\mathrm{EMC-L0}}}{P_{\mathrm{INT7}}}$ over both periods is found to be $3.4 \pm 0.2^{stat} \times 10^{-4}$ [GL$^+$|18]. With the number of events from section 4.3.2 this results in a final luminosity of

$$\mathscr{L} = 371 \pm 22^{\mathrm{stat}} \pm 13^{\mathrm{syst}}\,\mathrm{nb}^{-1}. \tag{4.26}$$

4.3.10 Cross-section

The calculation of the cross-section consists of three parts, the calculation of a corrected spectrum, the luminosity calculation and the final calculation. In the last step the previous results are combined with additional correction factors.

Applying the purity (section 4.2.3.4) and efficiency (section 4.3.7) correction on the raw spectrum results in the corrected spectrum

$$\frac{d^2N_{\gamma_{\mathrm{iso}}}}{N_{\mathrm{evt}}dE_{\mathrm{T}}d\eta} = \frac{1}{N_{\mathrm{evt}}} \cdot \frac{d^2N^{\mathrm{iso}}}{dE_{\mathrm{T}}d\eta} \cdot \frac{p\,(E_{\mathrm{T}})}{\epsilon\,(E_{\mathrm{T}})}. \tag{4.27}$$

Taking the luminosity and additional correction factors for trigger efficiency and trigger timing into account and using the corrected

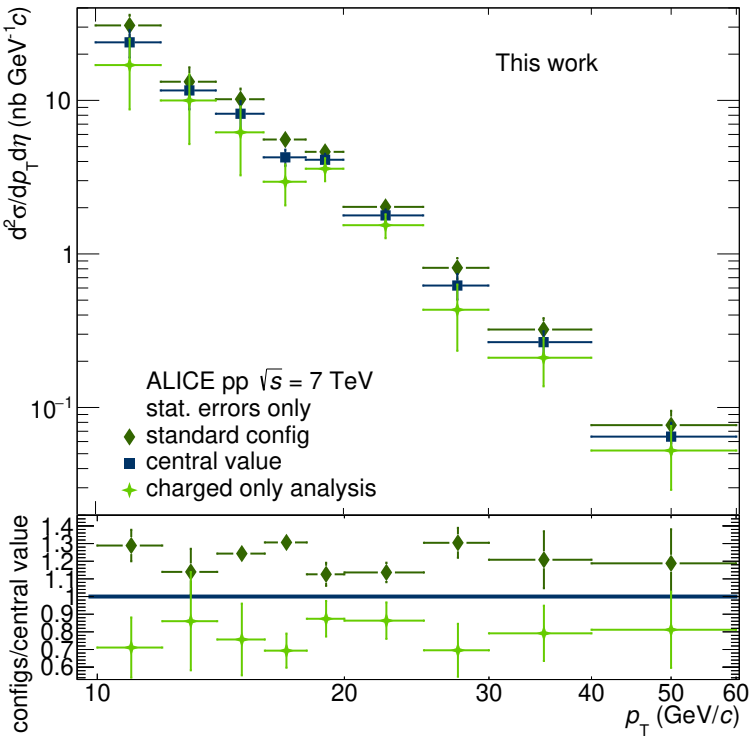

Figure 4.18: Cross section for the standard configuration, charged-only setup and resulting central value.

spectrum, equation 4.25 modifies as:

$$\frac{d^2\sigma_{\gamma_{\text{iso}}}}{dE_T d\eta} = \frac{N_{\text{evt}}}{\mathscr{L}} \cdot \frac{d^2N_{\gamma_{\text{iso}}}}{N_{\text{evt}} dE_T d\eta} \cdot \frac{1}{\epsilon^{\text{trigg}} \cdot \mathscr{C}}. \tag{4.28}$$

The resulting cross-section is shown in figure 4.18 as dark green diamonds. The behaviour in the high p_T regime can be described by a power law, while the lower p_T part can be described by an exponential trend. The results show only statistical uncertainties, the results with the statistical and systematic uncertainties is shown in figure 4.31.

4.3.11 Central value

As mentioned before, the calculation highly depends on the energy in the isolation cone. To evaluate possible biases of the isolation cone energy, the analysis is repeated with a different measurement of the energy in the isolation cone. Instead of taking neutral clusters and charged particles into account, only charged particles contribute to the energy in the isolation cone. To compensate the missing energy of neutral particles, the isolation criteria is reduced to 1 GeV/c.[2]

The mean value from both analyses is calculated and referred to as central value. The central value is considered as final cross-section

2: The theoretical limit due to isospin symmetry would be 1.33 GeV/c, but only a very weak change in signal was found in [Lod|18], so no large influence from the deviation is expected.

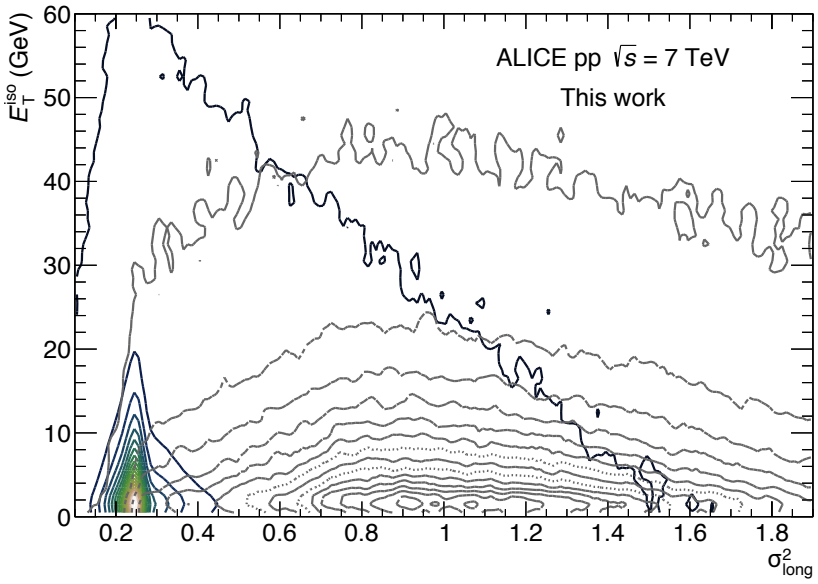

Figure 4.19: Distribution of NLM = 1 (coloured isolines) and NLM = 2 (grey isolines) in the σ^2_{long}-$E_{\text{T}_{\text{iso}}}$ space.

and together with the two input cross-sections it is depicted in figure 4.18. The deviation from the charged + neutral analysis and the charged-only analysis are taken into account as systematic uncertainty, as shown in figure 4.27 and are discussed in section 4.5.7.1.

4.4 Clusterizer Studies

4.4.1 Study of different clusterizer options

Apart from the standard cluster selection (v1 clusterizer, NLM ≤ 2) in this section other possible clusterizer settings are investigated and discussed. The study with different technical adjustments can help to understand the influence of the chosen default configuration on the analysis. As starting point, in figure 4.19 the different cluster distributions for NLM = 1 and NLM = 2 in the σ^2_{long} - $E_{\text{T}_{\text{iso}}}$ space are shown. The combination of both cluster distributions corresponds to the standard cluster selection. The different contours of the data points represent the origin of the clusters depending on the number of local maxima. Clusters with one local maximum are represented by the coloured contour lines, while clusters with two local maxima are shown as grey lines.

In the following, the case of using the v1 clusterizer with NLM = 1 (section 4.4.1.1) and performing the analysis with the v2 clusterizer instead of v1 (section 4.4.1.2) are scrutinised. For all variations, the complete analysis as described in chapter 4 is repeated. If not explicitly mentioned, no adaptions to the configuration are performed.

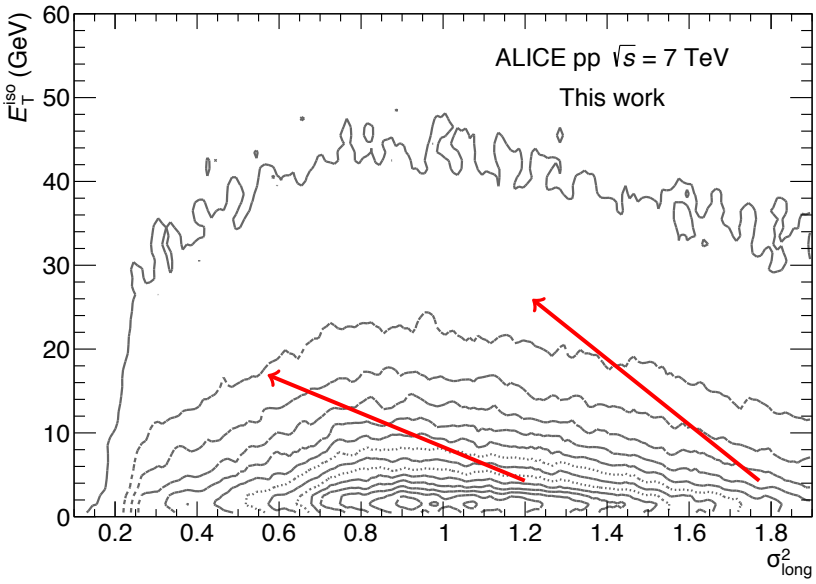

Figure 4.20: Distribution of NLM = 2 clusters and indication where the clusters will be positioned with the v2 clusterizer.

4.4.1.1 Variation of number of local maxima

As described in section 4.2.2, the NLM is limited to two to reject jet-like events. The inclusion of clusters with more local maxima only changes the results at maximum by approximately 5 % as shown in firgure 4.29. The deviation is taken into account as systematic uncertainty and discussed in section 4.5.14. Another variation is to limit NLM = 1. In this case, only clusters represented by the coloured contours in figure 4.19 are used for the analysis. With this change in the cluster distribution, especially clusters in the background region are rejected. Through this rejection, the assumptions for the $\mathcal{ABCD}$ method (see section 4.2.3.1) are no longer fulfilled, as a significant background is needed. Consequentially, the $\mathcal{ABCD}$ method does not work and the analysis cannot be performed with this clusterizer setting.

4.4.1.2 Using v2 clusterizer

Unlike for NLM = 1 with the v2 clusterizer, no clusters are rejected, instead clusters with multiple local maxima are split into new clusters. Each split cluster creates at least two new clusters. In the σ^2_{long}-$E_{\text{T}_{\text{iso}}}$ phase space, the splitting reduces the number of clusters with elongated shape, but simultaneously newly created clusters have a higher $E_{\text{T}_{\text{iso}}}$ value. In figure 4.20, the change in the cluster distribution for NLM = 2 is indicated. Because the cluster selection runs after the clusterizer, also clusters with NLM > 2 are taken into account for this analysis.

Due to the changed cluster distribution, the assumption of a background cluster distribution independent of the cluster shape does not apply any more. Fortunately, an alternative assumption can be formulated. By transposing the σ^2_{long}-$E_{\text{T}_{\text{iso}}}$ phase space to an $E_{\text{T}_{\text{iso}}}$-$\sigma^2_{\text{long}}$ phase space the second assumption can be reformulated to: the distribution between circular and elongated cluster shapes for background clusters is independent of the isolation energy. This reformulation does not change the calculation, as only region $\mathcal{B}$ and $\mathcal{C}$ were changed and as visible in equation 4.7 these two values are multiplied by each other.

The analysis is performed in the same steps as described in sections 4.2 and 4.3 with the exception of using only the charged + neutral isolation criterion. As described above, the splitting produces non-elongated clusters with higher values in the isolation cone. If only charged contributions to the isolation cone are taken into account, the additional contributions by the split clusters are ignored. By ignoring these contributions, all clusters are just moved to lower σ^2_{long} values and the distribution is no longer reliable to be used in the $\mathcal{ABCD}$ method, like in the NLM = 1 case. For this reason the v2 analysis solely relies on charged + neutral contributions to the isolation cone and the comparison between the standard and the v2 setting is performed for charged + neutral contributions only.

In figure 4.21 the difference of the number of clusters using the v2 clusterzier to the standard clusterizer setting in the four regions $\mathcal{A}$, $\mathcal{B}$, $\mathcal{C}$, and $\mathcal{D}$ is compared. The results fit to the assumption on the change in the distribution as discussed before: Only a small amount of clusters is added to region $\mathcal{A}$ (figure 4.21a) through the v2 clusterizer. The number of clusters in region $\mathcal{B}$ (figure 4.21b) is reduced to a large amount. Especially in the low p_{T} region with a high splitting probability nearly 90 % of the clusters are shifted to regions with higher $E_{\text{T}_{\text{iso}}}$. A similar trend can be observed in region $\mathcal{D}$ (figure 4.21d). At low p_{T} a strong suppression of clusters is visible, while at high cluster p_{T} even an increase of clusters can be observed. This increase originates from clusters with an E_{T} of more then 60 GeV, which are excluded by the standard analysis cuts. During the splitting the momentum is distributed to multiple clusters, which pass the analysis cuts. As indicated in figure 4.21c most clusters are shifted to region $\mathcal{C}$. The increase appears over the whole p_{T} range without a p_{T} dependency.

The resulting outcome of the analysis with selected intermediate results is shown in figure 4.22. The efficiency (figure 4.22a) for the low p_{T} region is nearly identical. With increasing p_{T} the efficiency of v2 decreases until it reaches a plateau approximately

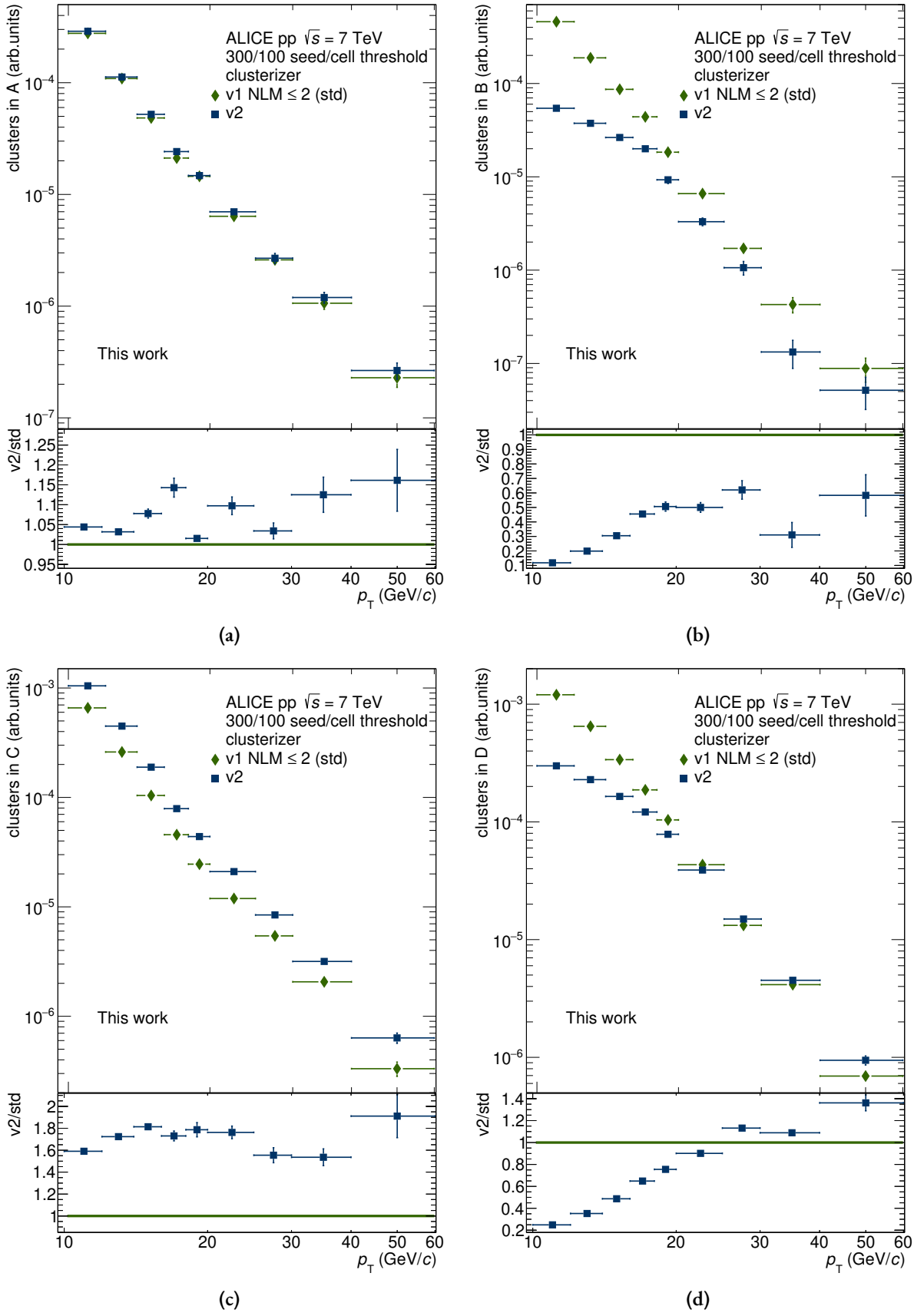

Figure 4.21: Number of clusters in the four regions of the $\mathcal{ABCD}$ method for v2 and v1 with NLM ≤ 2 clusterizer.

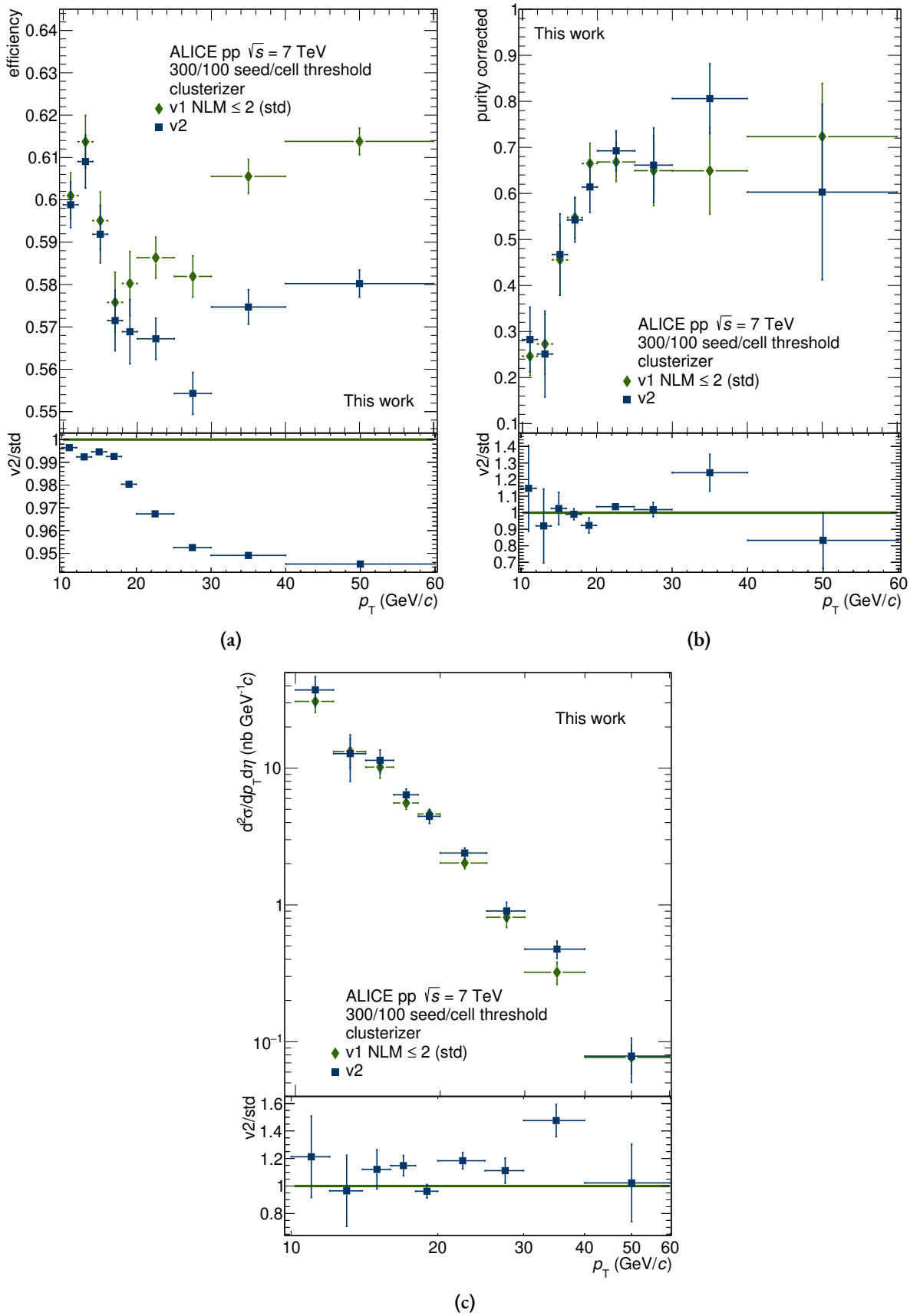

Figure 4.22: Efficiency (a), corrected purity (b), corrected spectrum (c) for v2 and v1 with NLM ≤ 2 clusterizers.

5 % below the standard values. For the corrected purity (figure 4.22b) the differences between the two analyses flucatuate around unity without a trend. The comparison of the cross-sections (figure 4.22c) shows that most of the v2 values are about 15 % higher and fluctuate around this value. For the most bins the values are also in agreement with unity within their uncertainties. Nevertheless the results of using the v2 clusterizer reveals the same behaviour as the standard analysis. Taking the different clusterizers and the different assumptions for the $\mathcal{ABCD}$ method into account, the v2 result supports the results of the default analysis and also backs the reliability of the $\mathcal{ABCD}$ method. The results of the v2 analysis could also be used as additional contributor to the central value. Similar to the difference in the isolation energy between the default analysis and the charged-only analysis, the v2 analysis treats the cluster shape dependency in a different way. It also includes clusters rejected before by the NLM cut. An inclusion to the central value would cover the uncertainties correlated to the clustering process and the NLM cut. A study of the differences in the statistical and systematic uncertainties can be found in section 4.5.16.

4.4.2 Threshold Variations

After studying the effect of different clusterizer settings, in the following, the influence of the energy thresholds for the clusterizer is analysed. The two thresholds described in section 2.3 are varied from their nominal values of 300 MeV and 100 MeV for seed and cell threshold, respectively. The seed threshold is varied to 100 MeV and 500 MeV. With these variations the influence of low energetic clusters, which have a worse energy resolution, can be studied. The purpose of the cell threshold variation is to study the influence of cell noise on the analysis. By choosing a low threshold, potentially noisy cells are included in the clustering process. Whereas the energy added to the cluster is rather small, the cluster shape is affected by the additional clusters and consequentially σ^2_{long}. Because the standard cell threshold of 100 MeV is selected as safe choice, only variations to lower values of 75 MeV and 50 MeV are studied. Additionally to the cell threshold study performed with the nominal seed threshold of 300 MeV an extra study is performed with a combination of 100/50 MeV for seed and cell threshold. This combination is selected because in the beginning of this isolated photon analysis the setting was used as default value, before switching to the new set of thresholds.

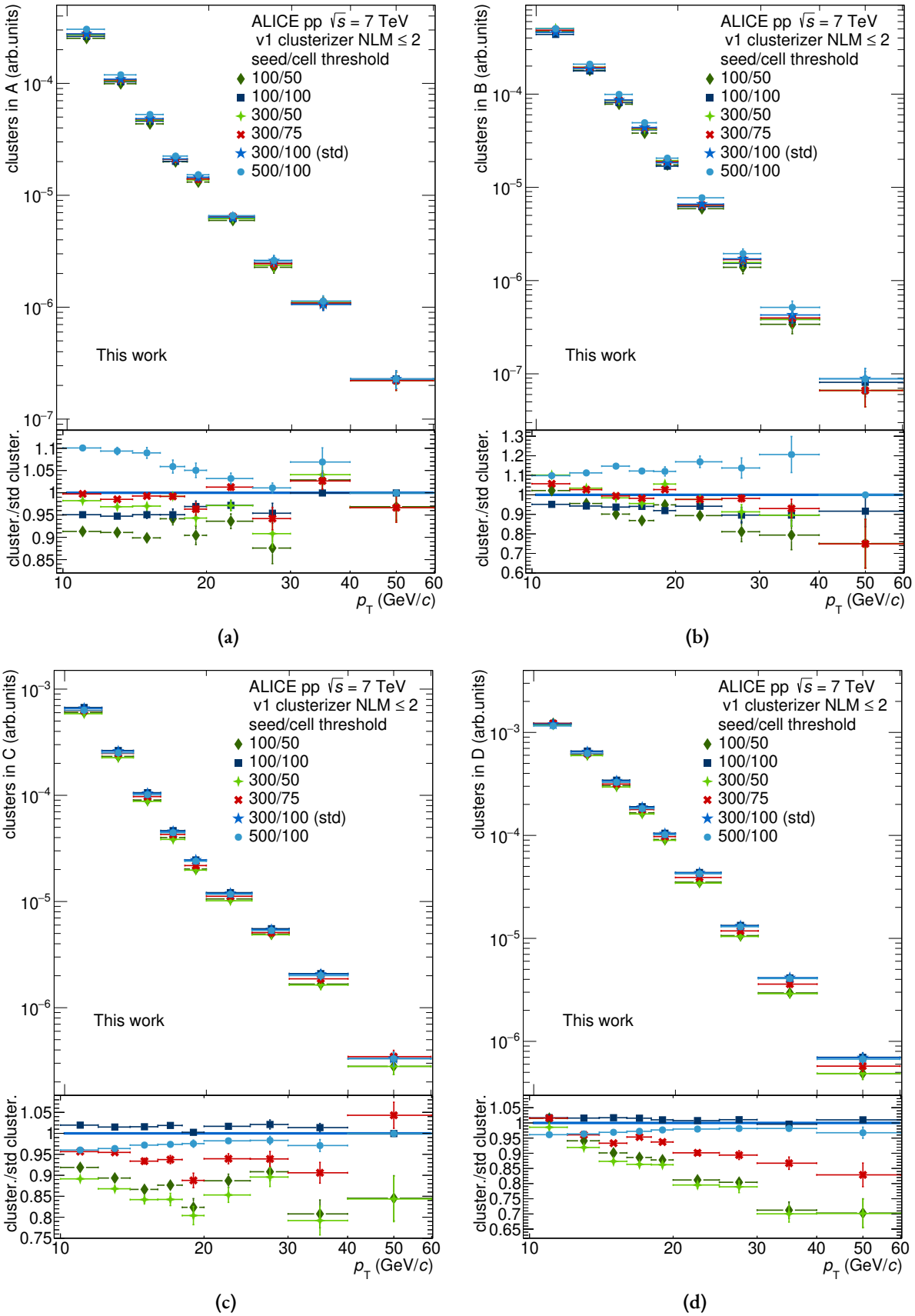

Figure 4.23: Number of clusters in the four regions of the $\mathcal{ABCD}$ method for six different clusterizer energy settings for NLM ≤ 2.

Like in the previous clusterizer study first the influence of the different thresholds on the four regions $\mathcal{ABCD}$ are analysed (figure 4.23). For region $\mathcal{A}$ (figure 4.23a) and $\mathcal{B}$ (figure 4.23b) a dependency on the seed threshold can be observed. The 500 MeV seed (dot) has higher values than the other seed values. All three variations with a seed of 300 MeV (crosses and stars) lie close to each other and between the two other seed thresholds. The number of clusters in the two regions is the smallest for seed values of 100 MeV (quadrangles). The ordering of the clusters by seed threshold indicates that the energy in the isolation cone largely depends on the seed threshold, as $\mathcal{A}$ and $\mathcal{B}$ represent isolated clusters. In regions $\mathcal{C}$ (figure 4.23c) and $\mathcal{D}$ (figure 4.23d) an ordering depending on the cell threshold can be observed. All clusterizers with a cell threshold of 100 MeV (blueish) have similar values. The values with cell thresholds of 75 MeV (red) are lower, but still higher then the 50 MeV (greenish) clusters. Within clusterizers with the same cell threshold an ordering dependent on the seed threshold can be found. This sub-order is opposite to the ordering in regions $\mathcal{A}$ and $\mathcal{B}$ and can be related to a general decrease of clusters with higher seed thresholds. In region $\mathcal{D}$ the ordering also shows a p_{T} dependence with stronger suppression for higher p_{T} values. This effect hints to a possible cluster merging due to the increased cluster size and can also explain the general decrease with lower cell thresholds.

In figure 4.24 the cross-sections and the intermediate results are shown. For the efficiency (figure 4.24a) a ordering depending on the cell threshold and a sub-ordering on the seed threshold can be observed. Smaller cell thresholds increase the efficiency, while lower seed threshold decrease the efficiency. The effect of the cell threshold on the different observables is by far larger than the effect of the seed threshold. The origin of these effects are the increased number of clusters created by the lower cell threshold and the increased number of clusters in the background for lower seed thresholds. Generally, the variation on the efficiency is quite small compared to other variations. For the purity (figure 4.24b) no ordering can be observed, except of the variation with a seed of 500 MeV, all purity values fluctuate around the standard value. In the high p_{T} region the purity for seed thresholds of 500 MeV reaches unrealistic values of over 90 %. Similar results can be observed for the cross-section (figure 4.24c), where the 500 MeV data set run away. All other results for the cross-section fluctuate around the standard setting within approximately 10 % and in the most cases agree within their statistical uncertainties. In section 4.5.16 the statistical and systematic uncertainties for the clusterizer thresholds are discussed.

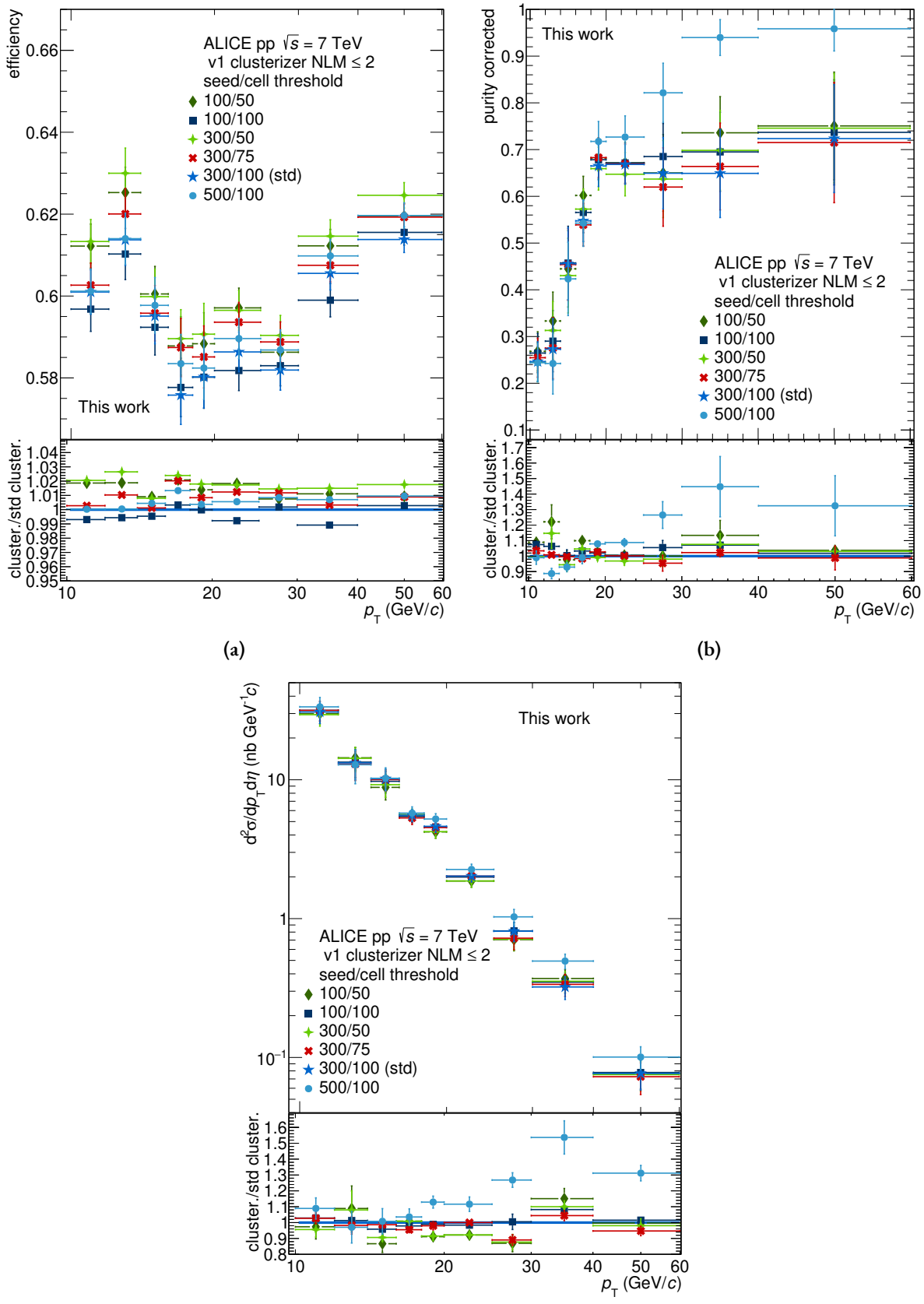

Figure 4.24: Efficiency (a), corrected purity (b), cross-section (c) for different cluster thresholds with clusterizer NLM ≤ 2.

The comparison of the different clusterizer thresholds reveal consistent results, apart from a seed threshold of 500 MeV. The agreement nicely shows that different cluster selections only have a small effect on the results with the $\mathcal{ABCD}$ method. The change from the 100/50 MeV clusterizer setting to a setting of 300/100 MeV does not have a large effect on the final results. The cluster distribution in the four regions show that the cluster shape is influenced by the clusterizer setting and noisy clusters could have an influence on the result. On the other hand the result for the 500/100 MeV clusterizer setting indicates that higher thresholds reject too many background clusters to allow for reliable results by the $\mathcal{ABCD}$ method.

4.5 Systematic Studies

In section 4.5.1 the general extraction of the systematic uncertainties and their combination is discussed. The different variations of the measurement to estimate the systematic uncertainty are described in section 4.5.2.

4.5.1 General procedure for systematic uncertainties

For each source of uncertainty the corresponding step of the analysis chain is varied. Each variation results in a new isolated photon cross-section. Depending on the analysis step the number of variations differs. For each variation the relative deviation to the baseline is computed. Except for the systematic uncertainties evaluated in section 4.5.7, the standard analysis described in section 4.3 with the charged + neutral energy in the isolation cone represents the baseline. To calculate the total uncertainties, the mean value of the variations for each analysis step is computed. The mean value is chosen to reduce the influence of outliers and fluctuations. In a last step the square root of the sum of the squared relative uncertainties is calculated.

4.5.2 Systematic variations

For the analysis, 13 different sources of systematic uncertainties ($\mathbb{S}1 - \mathbb{S}13$) as listed in table 4.4 are evaluated. A detailed description of the single systematic uncertainties can be found in the following sections 4.5.3 to 4.5.11. The systematic uncertainties can be roughly

§1	Signal region upper limit
§2	Background region limits
§3	Charge particle veto / track matching
§4	Isolation energy
§5	Mixing ratio
§6	Charged-only analysis
§7	MC shower shape tuning
§8	Simulation signal uncertainty
§9	Trigger efficiency and stability
§10	Pile-up correction
§11	Energy scale uncertainty
§12	Material budget
§13	NLM cut

Table 4.4: List of sources of systematic uncertainties.

split in p_T-dependent uncertainties (§1 – §7) and p_T-independent sources (§8 – §13).

4.5.3 Shower shape limits §1 & §2

The limits of the shower shape axis in the $\mathcal{ABCD}$ method are relevant for the signal and the background region. Due to the fixed lower limit of the signal region, both regions are handled differently.

4.5.3.1 §1: Signal region limits

In the signal region only the upper limit of the σ^2_{long} is varied, as the lower limit is necessary to reject non-physical clusters. The variation tests the sensitivity of including or excluding clusters on the upper edge of the single cluster distribution. With the variation also the gap to the background region varies and thus the differentiation between signal and background region. This also varies the leakage of photon clusters to the gap region and correspondingly also affects the efficiency.

The modified cut values are chosen to vary at least by 10 % from the original value. The values for all p_T bins are listed in table 4.5. The corresponding uncertainties can be seen in figure 4.25, the relative values vary between 2 % and 10 % with higher uncertainties at higher p_T.

	signal σ^2_{long} region limits		background region limit	
p_{T} range	lower variation	higher variation	lower variation	higher variation
10 - 12	0.1 – 0.35	0.1 – 0.55	0.4 – 1.6	0.7 – 1.9
12 - 14	0.1 – 0.35	0.1 – 0.5	0.4 – 1.6	0.6 – 1.8
14 - 16	0.1 – 0.3	0.1 – 0.45	0.35 – 1.55	0.55 – 1.75
16 - 18	0.1 – 0.27	0.1 – 0.4	0.3 – 1.5	0.5 – 1.7
18 - 20	0.1 – 0.27	0.1 – 0.4	0.3 – 1.5	0.5 – 1.7
20 - 25	0.1 – 0.27	0.1 – 0.4	0.3 – 1.5	0.5 – 1.7
25 - 30	0.1 – 0.27	0.1 – 0.4	0.3 – 1.5	0.5 – 1.7
30 - 40	0.1 – 0.27	0.1 – 0.4	0.3 – 1.5	0.5 – 1.7
40 - 60	0.1 – 0.27	0.1 – 0.4	0.3 – 1.5	0.5 – 1.7

Table 4.5: Variation of σ^2_{long} cuts.

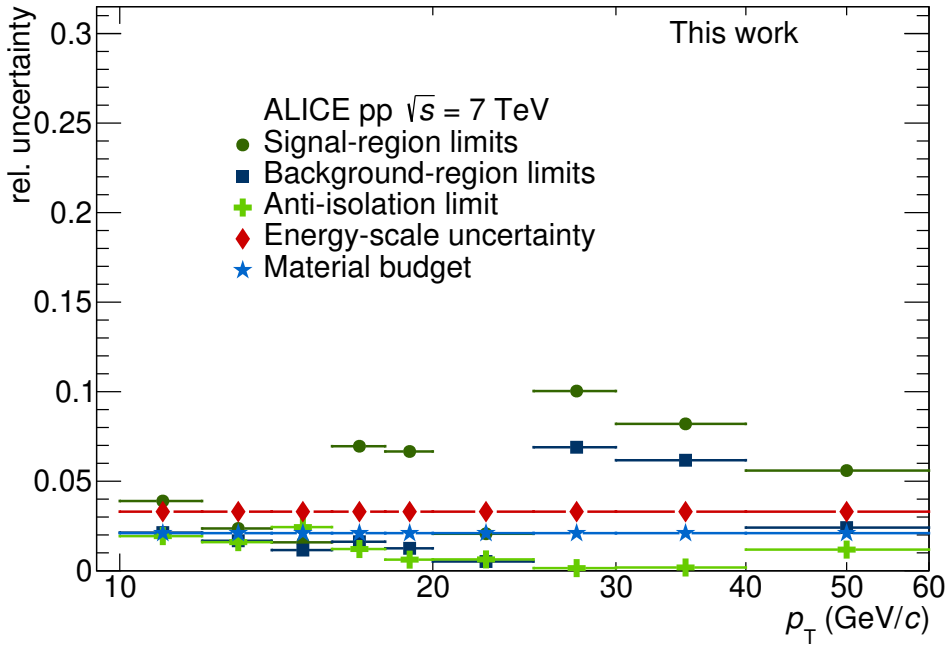

Figure 4.25: Variations related to the variations for the $\mathcal{ABCD}$ region limits and uncertainties of the energy uncertainty.

4.5.3.2 S2: Background region limits

Similarly to the signal region also the limits for background region are varied. In contrast to the signal region, both limits, the lower and the upper are varied. For each variation, the upper and lower limit are shifted in the same direction to keep the range identical for all cases. Like the variation of the signal region also the variation of the background region influences the separation between both regions and accordingly also the leakage of true photon clusters to the background region.

For the modified cut values, listed in table 4.5, the same constraints of a change of at least 10 % in the cut value are used. The resulting

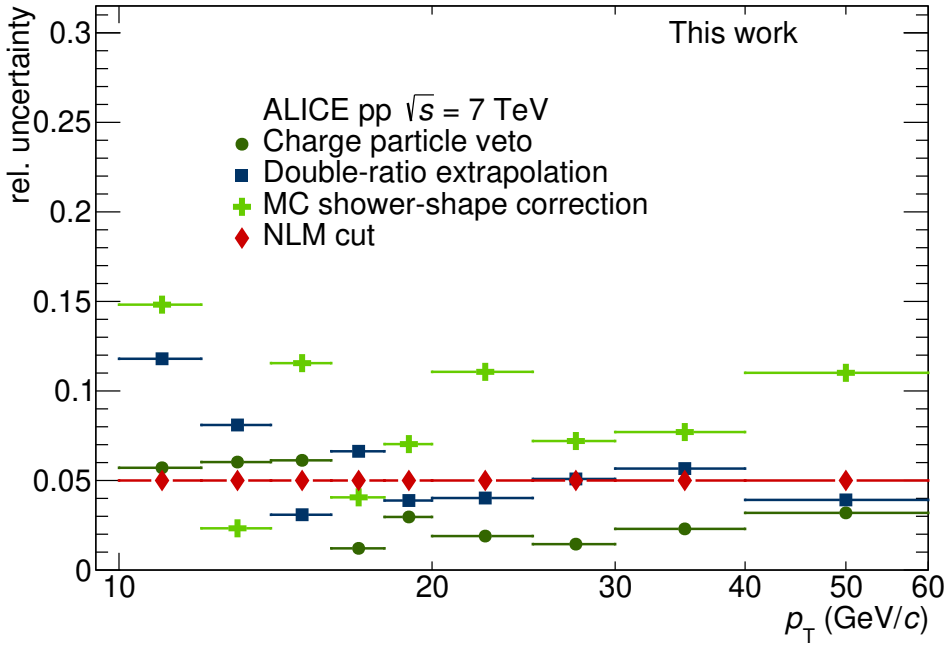

Figure 4.26: Uncertainties related to the shower shape and shower composition together with uncertainties related to the charge particle veto.

uncertainties are plotted in figure 4.25 as well. Generally, the effect is smaller than for S1, but it shows a similar trend with lower values at low p_T and higher uncertainties at higher p_T.

4.5.4 S3: Charge particle veto

To estimate the performance of the charge particle veto (CPV), the analysis is repeated with a tighter and a looser cut setting. In the more stringent scenario, the distances to match a track to a cluster are increased from $|\Delta\eta| \leq 0.1 + \left(p_T + 4.07\right)^{-2.5}$ to $|\Delta\eta| \leq 0.15 + \left(p_T + 3.46\right)^{-2.5}$ and from $|\Delta\varphi| \leq 0.15 + \left(p_T + 3.65\right)^{-2}$ to $|\Delta\varphi| \leq 0.2 + \left(p_T + 3.73\right)^{-1.75}$. While in the loose case the distances are reduced to $|\Delta\eta| \leq 0.1 + \left(p_T + 4.78\right)^{-2.5}$ and $|\Delta\varphi| \leq 0.15 + \left(p_T + 3.92\right)^{-2}$.

The CPV has a double effect on the analysis. First, the rejection of photon candidate clusters of charged origin influences the total number of photons. Second, clusters in the isolation cone correlated with a charged track contribute less to the energy in the cone than a neutral cluster plus a charged track in the cone. Accordingly, in the stringent case, the number of photons is reduced, but on average, the energy in the isolation region is reduced as well. In the loose case, more photon candidates pass the CPV, but the probability to define them as isolated photon is decreased.

The resulting uncertainties are shown in figure 4.26 and show uncertainties of about 6 % for low p_T values, which decrease to 3 % with increasing p_T.

4.5.5 §4: Isolation energy modelling

The description of the underlying event in the simulations has a discrepancy with the recorded data and accordingly also describes the energy in the isolation cone only partially. To estimate and correct for this deviation, two different approaches are used, which are described in the following. Both approaches are handled as individual contributions to the total systematic uncertainties and are not mixed, as they focus on different discrepancies.

4.5.5.1 §4*a*: Double ratio

As described in section 4.3.8.1 the calculation of a double ratio can be used to describe a σ^2_{long} discrepancy between simulation and recorded data. The fits of a linear function and an exponential function to the double ratio performed in the double ratio analysis and shown in figure 4.16 agree within their uncertainties with a constant function. For the estimation of the uncertainties, the previously fitted functions are used to calculate an additional correction factor. The combination of the new correction factor β with the existing correction α results in a new total correction factor α'. Thereby, β is defined as the ratio of the function values for clusters in the signal region (x_s) and clusters in the background region (x_b).

$$\alpha' \rightarrow \alpha \cdot \beta \tag{4.29}$$

$$\beta_{\text{lin}} = \frac{x_s \cdot p_1 + p_2}{x_b \cdot p_1 + p_2} \tag{4.30}$$

$$\beta_{\text{exp}} = \frac{p_1 \cdot e^{p_2 \cdot x_s} + p_3}{p_1 \cdot e^{p_2 \cdot x_b} + p_3} \tag{4.31}$$

The x values are defined as the median values of the clusters in the signal and the background region. For the linear and the exponential function, the analysis is performed with α' as correction instead of α. The resulting uncertainty varies between 3 % and 12 % and is shown in figure 4.26.

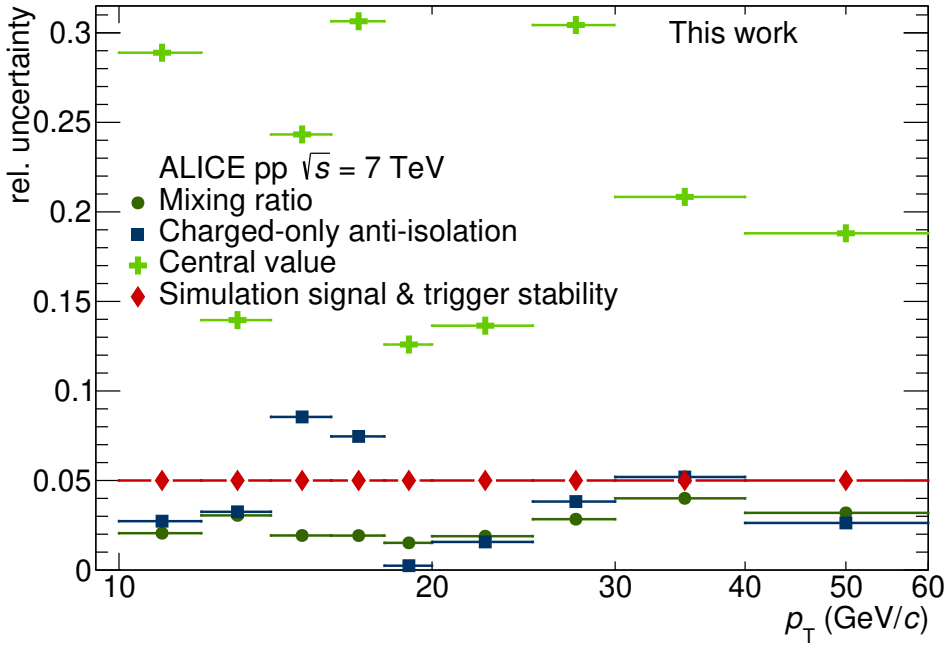

Figure 4.27: Uncertainties related to the charged-only analysis, simulation properties, and trigger properties.

4.5.5.2 §4*b*: Anti-isolation limit

Another possibility is to change the anti-isolation criterion, defining the lower limit of the non-isolation region. Similar to the systematic on the background region limit (section 4.5.3.2), the upper limit of the gap between isolated and non-isolated clusters is varied. The lower gap limit is not varied, as this would implicate a change in the definition of isolated photons. The upper limit of the anti-isolation region is also not shifted according to the gap variation. For the systematic uncertainty, the upper limit if the gap is once reduced from 3 GeV to 2 GeV and once increased to 4 GeV. Except from one outlier, the related uncertainty lies below 2 % and is shown in figure 4.25.

4.5.6 §5: Mixing ratio

As mentioned before, the uncertainty of the mixing ratio plays an important role for the purity correction. Starting from the best mixing ratio evaluated in section 4.3.6, the weighting factor of signal and background are individually doubled. For the resulting signal-to-background mixing ratios of 0.88 to 0.56 (~ 0.61/0.39) and 0.44 to 1.12 (~ 0.28/0.72), a significant change in the χ^2 values can be observed in figure 4.13. Despite the large change in agreement, the uncertainty is only between 2 % and 4 % and depicted in figure 4.27.

4.5.7 §6: Charged-only analysis

The charged-only analysis has two contributions to the total systematic uncertainties, the central value and the anti-isolation limit in the charged-only analysis. Both contributions are plotted in figure 4.27.

4.5.7.1 §6*a*: Central value

As described in section 4.3.11, a central value from combined results is used as final result. The difference between the two input spectra and the central value is accounted as systematic uncertainty. The uncertainty varies between 13 % and 31 %, with no clear p_{T} dependence.

4.5.7.2 §6*b*: Anti-isolation limit in charged-only

Additionally, the lower energy limit for non-isolated clusters is varied in the charged-only analysis similar to contribution §4*b*. For the lower case it is decreased to 1 GeV and for higher case increased to 3 GeV. The resulting uncertainty varies between 0.5 % and 9 %. This contribution is taken into account independently from the uncertainty of the central value.

4.5.8 §7: MC shower shape correction

The description of cluster shapes for the EMCal disagrees between recorded data and simulations. In parallel to the isolated photon analysis detailed studies on the cluster shape were performed. The studies revealed cross-talk in the read-out electronics as origin [CB|18] of the difference. For a better agreement between recorded data and simulations, a mimicking of the cross-talk was implemented in the post-processing of the simulations. The shower shape distributions for recorded data, before and after the mimicking are compared in figure 4.28. For all three energy ranges, a clear improvement of the modified distribution (red) can be found compared to the original one (blue). In the default analysis procedure, only the mimicked clusters are used. To estimate the uncertainty of the mimicking, the results are compared to those without any modification of the cluster shape. Though the usage of the unmodified clusters represents a change for the worse, it allows for a good estimate of the possible uncertainties of the mimicking procedure. The uncertainties of the shower shape correction, shown in figure

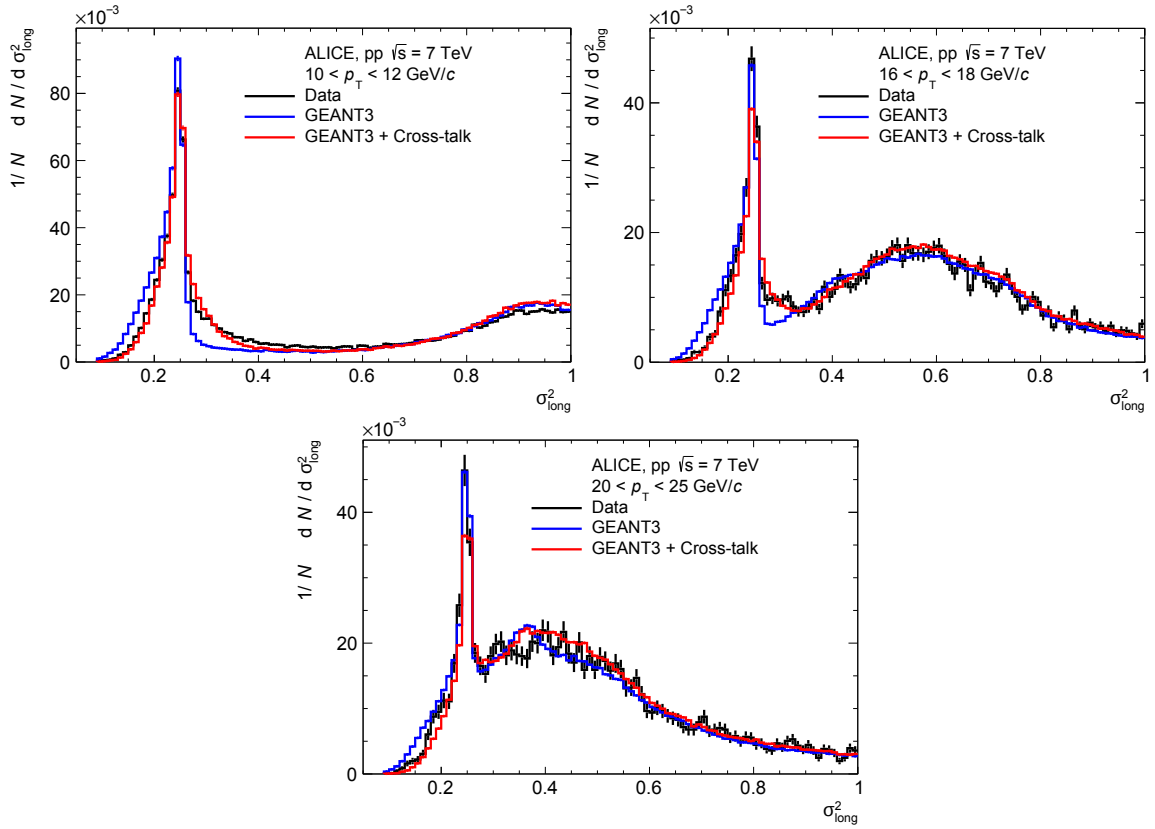

Figure 4.28: Shower-shape distributions of data and simulations for three different energies. [CB|19]

4.26, vary for most p_T bins between 7 % and 11 %, but have outliers to 2 % and 15 % in the low p_T region.

4.5.9 §8: Simulation signal uncertainty

The limited run selection for MC productions may bias the efficiency calculated from these productions. To correct for the bias in the recorded data, the number of high energetic clusters in the sub-samples are compared with the number of clusters in the appropriate period. As this correction is not perfect and can still contain an undistinguishable bias by the trigger efficiency and stability (§9), these uncertainties are evaluated as combined uncertainty.

4.5.10 §9: Trigger efficiency and stability

While the trigger threshold for the whole data set is fixed, it can vary slightly due to changing conditions in the detector and readout electronics. These fluctuations influence as well the trigger properties as the correction of the simulation uncertainty described in section 4.5.9. To estimate the uncertainty of both effects, the number of

clusters with more than 10 GeV per event is calculated for each run. The RMS of the distribution over all runs is about 5 %, which is also assigned as contribution to the total systematic uncertainty. The combined systematic uncertainty for S8 and S9 are plotted in figure 4.27.

4.5.11 S10: Pile-up correction

For each bunch crossing the probability exists, that more than one pp collision takes place. A possible second collision would increase the probability of a photon candidate. At the same time any additional collision would increase the energy in an isolation cone, as it is not possible to specify the source of neutral particles. Due to the beam conditions during data taking the possibility of pile-up collisions is rather low and therefore the contribution to the total uncertainty is negligible.

4.5.12 S11: Energy scale

The energy scale uncertainty is estimated by different techniques which allow for the comparison of particle properties measured with the EMCal. During the test beam campaign the EMCal modules were tested with electron and hadron beams at Fermilab and CERN [EMCal|10]. For the analysis [ALICE|17b], the energy-to-momentum ratio of electrons was compared between simulations and recorded data. In total, an uncertainty of 0.8 % was determined, which accounts for an uncertainty of 3.3 % in the cross-section measurement and is shown in figure 4.25.

4.5.13 S12: Material budget

The material budget inside ALICE is only known to a certain degree and can accordingly only be modelled with uncertainties. Depending on the deviation the number of expected conversions can be either reduced or increased. Additionally, the place were the conversion happens also influences the effect. The produced electron-positron pair either produces a π^0-like cluster or creates a charged contribution to an isolation or misses the calorimeter due to curvature of the propagation. From previous studies [ALICE|19a], the uncertainty is estimated to be 2.1 % over the complete p_{T} range. The uncertainty is plotted in figure 4.25.

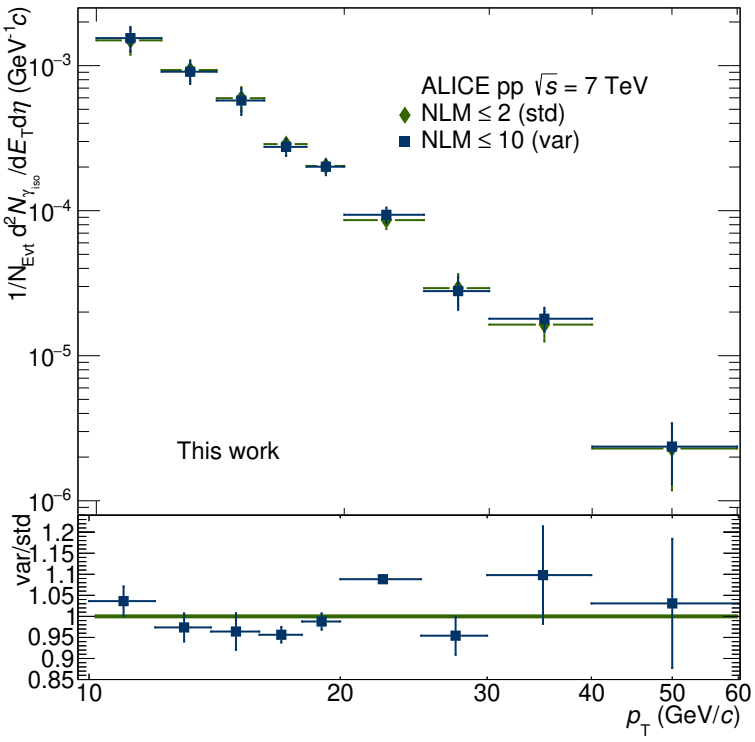

Figure 4.29: Comparison of the corrected spectrum between NLM ≤ 2 (standard) and NLM ≤ 10.

4.5.14 §13: NLM cut

As described in section 4.2.2, a cluster cut on the number of local maxima (NLM) is performed, primarily to reject clusters which very likely originate from jets. With the wider cut, the number of clusters in the background regions is increased. In figure 4.29 a comparison of the corrected p_T spectrum to a cut value of NLM ≤ 10 is shown. For the differences an uncertainty of 5 % is accounted over the whole p_T range. The contribution is depicted in figure 4.26.

4.5.15 Total systematic uncertainty

In figure 4.30 the total systematic uncertainties are plotted in comparison to the statistical uncertainties. For most of the bins, the systematic uncertainties are significantly higher than the statistical ones. The maximum systematic uncertainty is about 37 % and the minimal one 18 %.

The results for the central value, the statistical uncertainty and the systematic uncertainties are combined in the cross-section in figure 4.31.

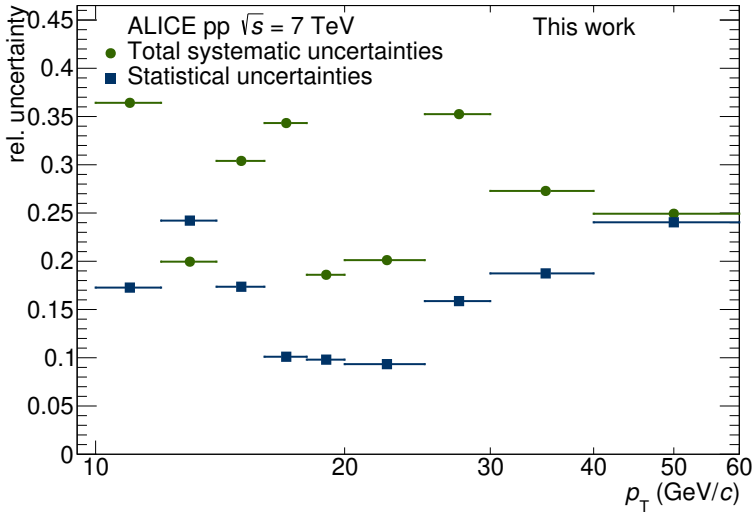

Figure 4.30: Comparison of the total systematic uncertainties to the the statistical uncertainties.

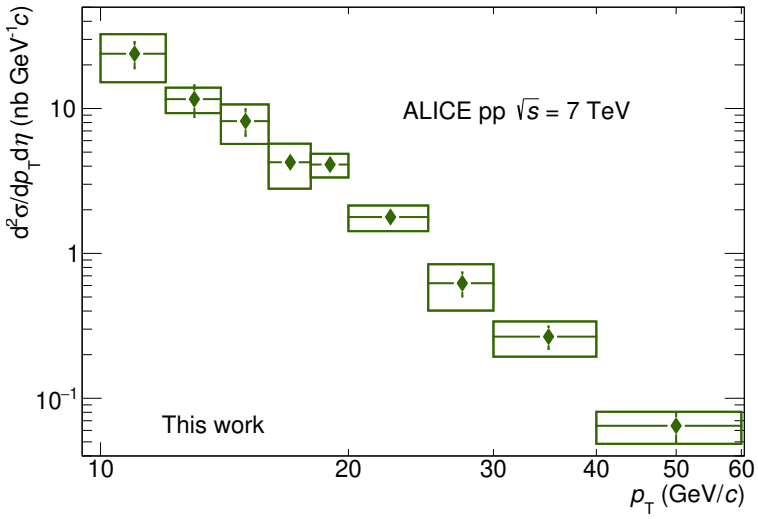

Figure 4.31: Final cross-section for the central value with statistical (bars) and systematic (boxes) uncertainties.

4.5.16 Total systematic uncertainties for clusterizer studies

Apart from the default analysis, the systematic uncertainties are also calculated for the different clusterizer settings as described in section 4.4.

A comparison of the statistical and total systematic uncertainties of the v2 clustetrizer settings described in section 4.4.1.2 with the default v1 clusterizer is shown in figure 4.32. Both statistical uncertainties (lines) have a similar trend over the complete p_T range and for the most bins are lower than the systematic uncertainties. The statistical uncertainties for the v2 clusterizer are higher in the low and the high p_T region compared to the v1 clusterizer. For the calculation of the total systematic uncertainties for the v2 settings, two contributions are not taken into account in contrast to the standard approach. The analysis of the v2 clusterizer with charged-only

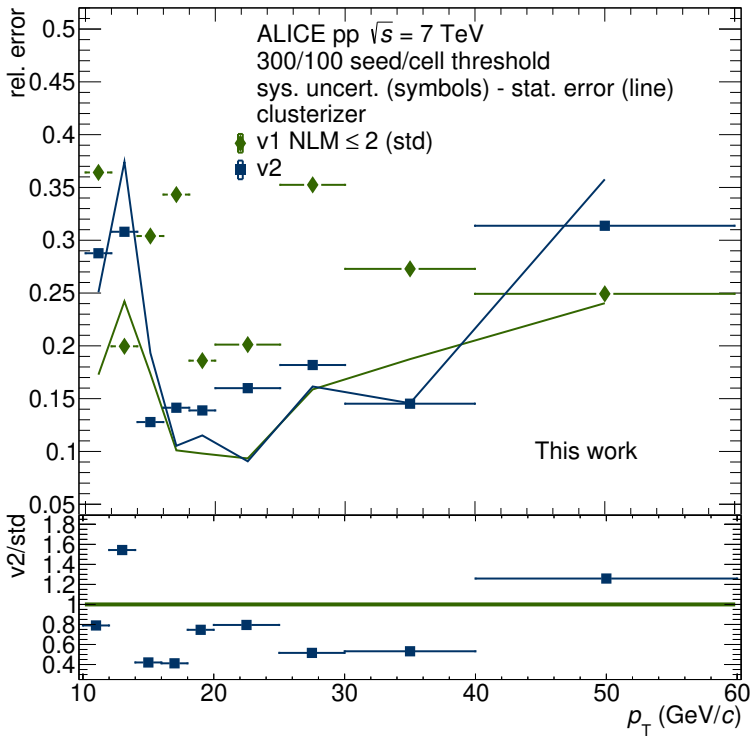

Figure 4.32: Comparison of uncertainties for v2 and v1 with NLM ≤ 2 clusterizers.

particles in the isolation cone does not work and no central value is calculated. Accordingly, no S6 is computed and not taken into account. Also the shift of clusters reduces the number of elongated clusters significantly. This results in large uncertainties for the fitting procedure and extrapolation on double ratios for S4*a*. To prevent contributions dominated by statistical fluctuations S4*a* is not included in the total systematic uncertainties. Like the statistical uncertainties, also the systematic uncertainties have a similar trend for both clusterizers. In the most cases the systematic uncertainties for the v2 clusterizer are smaller then the ones for the v1 case. For the v2 clusterizer a correlation between the statistical and systematic uncertainties is visible.

In figure 4.33 the statistical and systematical uncertainties are compared for different clusterizer thresholds. The statistical uncertainties (lines) show a nearly identical behaviour over the full p_T range for all threshold variations. This is not the case for the systematic uncertainties. While most variations have single outliers compared to the standard setting, the 500/100 setting starts to deviate from 20 GeV/c onwards. Remarkably, for all other threshold variations the deviation above 20 GeV/c is rather stable and fluctuate less, than in the lower p_T region.

The results for different clusterizer thresholds and a different clusterizer show a similar behaviour for the cross-section, as well as the uncertainties.

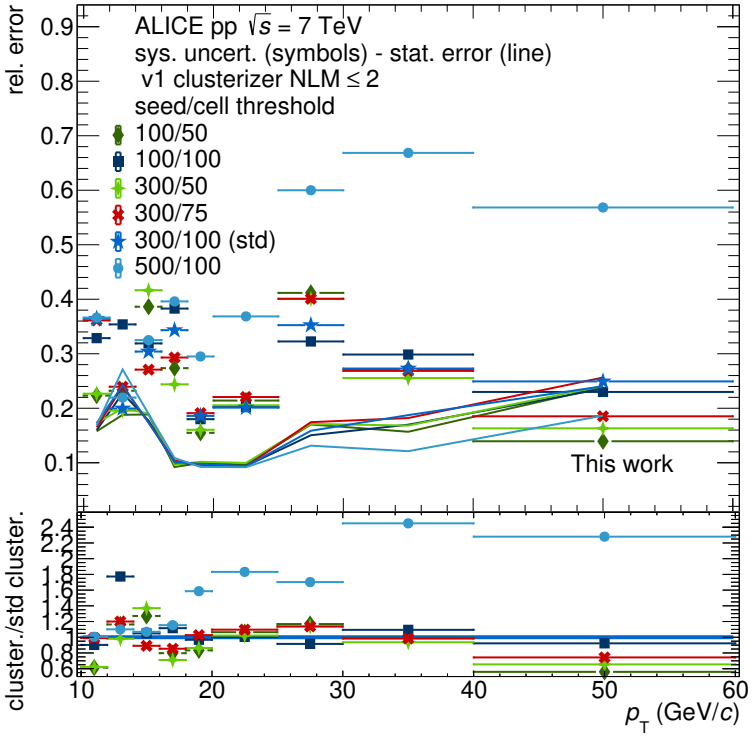

Figure 4.33: Comparison of uncertainties for different cluster thresholds with clusterizer NLM ≤ 2.

4.6 Comparison to published results

In figures 4.34 and 4.35 the result of the default analysis setting and the central value is compared with the corresponding published results. The settings for the default approach of the two analyses are identical in large parts. Differences can be found for the run selection, in this work runs with a non-working TPC sector in front of EMCal were rejected, while they were used for the published result. The rejected runs account for approximately 23 % of the events used for the published result. The decision of taking these runs into account or not is a trade-off between higher statistics and more homogeneous results and in this work the homogeneity was preferred. Additionally, the mixing ratio differs by a few percent, due to slight different inputs. The (anti-)isolation criteria for charged particle could not be matched with the published results, due to the usage of different analysis frameworks. As already mentioned in section 4.3.11, a deviation of these criteria is expected to have only a small effect on the results.

The difference of the cross-section shown in figure 4.34 between the two analyses shows good agreement within their statistical uncertainties for all results above 16 GeV/c. The three bins for the lowest momenta show a deviation of up to 25 %. The reason of the discrepancy may originate from a different handling of the low threshold background MC production, which is used for these bins.

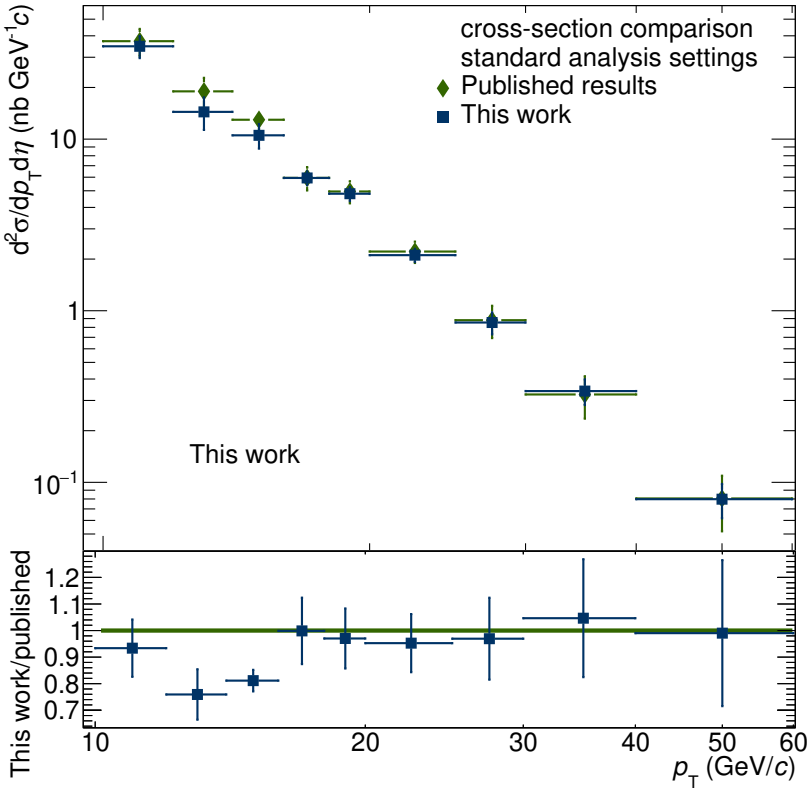

Figure 4.34: Comparison of results from this work to published results from [ALICE|19b] for standard analysis settings.

The different behaviour of the first three bins is not visible in the comparison of the central values in figure 4.35. The results of this work lie between 10 % and 30 % lower compared to the published result. This difference originates from different results taking into account for the central-value calculation. In this thesis only the results of the default setting and the results from the charged-only analysis are taken into account for the central value. In the published analysis additionally uncertainties for the isolation energy modelling are included in the calculation. The additional contributions are dominated by results close to the default settings and thus the central value is closer to the results from the default settings. For this analysis it was decided to take only the result from the charged-only analysis into account for the central value calculation to limit the contributions, which probe the isolation criteria with an additional approach. The additional contributions used in the published results for the central value calculation are included in the systematic uncertainties for this analysis.

The systematic uncertainties (boxes) for this work are larger compared to the published ones and cover the published results for the most bins. In contrast to the published systematic uncertainties, the single contributions to the total systematic uncertainties are not smoothed. This leads to the inclusion of outliers and more bin-to-bin fluctuations.

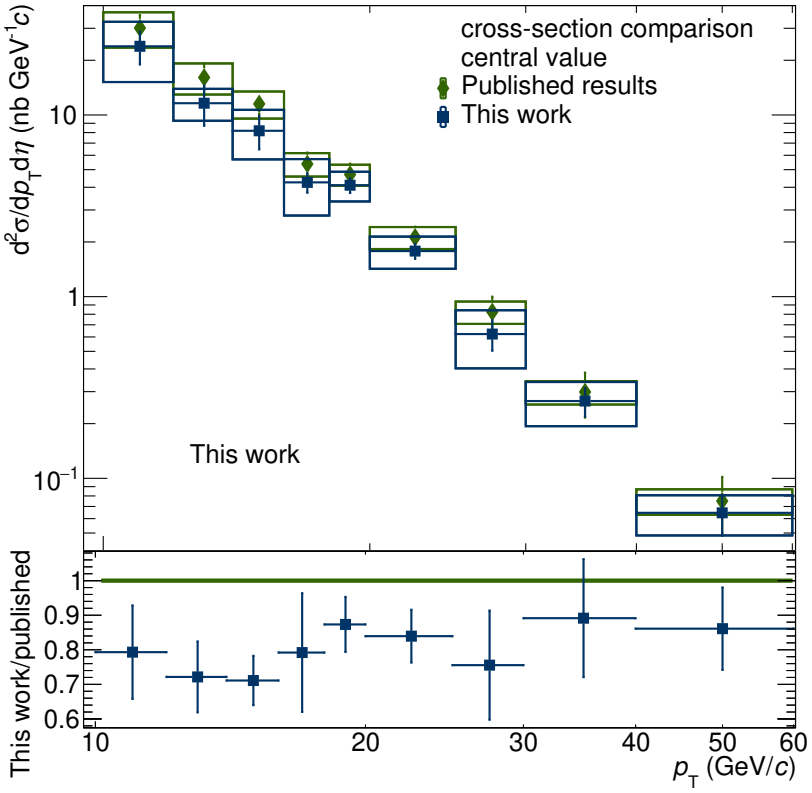

Figure 4.35: Comparison of results from this work to published results from [ALICE|19b] for the central value.

The difference in the analysis chain between the two results lead to deviations in the final results. Despite the differences the results can be considered as equivalent, as the majority of the deviations can be correlated to and explained by different choices in the analysis.

For the following comparison to other measurements and theory calculations the published results are taken into account.

5 Published results

5.1 Theory comparison

As baseline for the theory comparison a next to leading order (NLO) pertubative QCD (pQCD) calculation is used. The theory simulations also imply an isolation criterion with an isolation energy of 2 GeV. To achieve a good comparison, the results of the calculation use the same binning as in data. Uncertainties related to the theory calculation are grouped either to be PDF related or to be scale uncertainties. The resulting uncertainties are shown as independent sources.

The comparison of the spectra and the related ratio are shown in figure 5.1 and figure 5.2, respectively. In general, a good agreement between data and theory can be observed. Apart from the p_{T} bin from 18 GeV/c to 20 GeV/c all bins agree within their systematic uncertainties. While for the afore mentioned bin the uncertainties for data and theory overlap.

5.2 Comparison to previous measurements

The previous measurements of the isolated photon cross-section at $\sqrt{s} = 7\,\mathrm{TeV}$ performed by ATLAS [ATLAS|11a] and CMS [CMS|11] use a different energy threshold for the isolation criterion. Due to this difference, a direct comparison would compare different physics cases and is not performed. Instead, the ratios of the previous measurements to the corresponding simulations are compared, shown in figure 5.3. Since the isolation criteria in the simulations match the ones used in the analyses, the difference in the isolation criteria no longer play a role. The comparison only contains measurements relevant to the p_{T} range of ALICE. Within their overlapping region, all three ratios agree. Also the p_{T} region below 15 GeV/c only covered by the ALICE measurement is visible.

An additional way to compare the result to previous measurements is shown in figure 5.4. As described in section 1.5.2, the scaled cross-section is plotted against x_{T}. In contrast to figure 1.15b only previous measurements taken at central rapidity are shown. The results of the ALICE isolated photon measurement clearly extends the

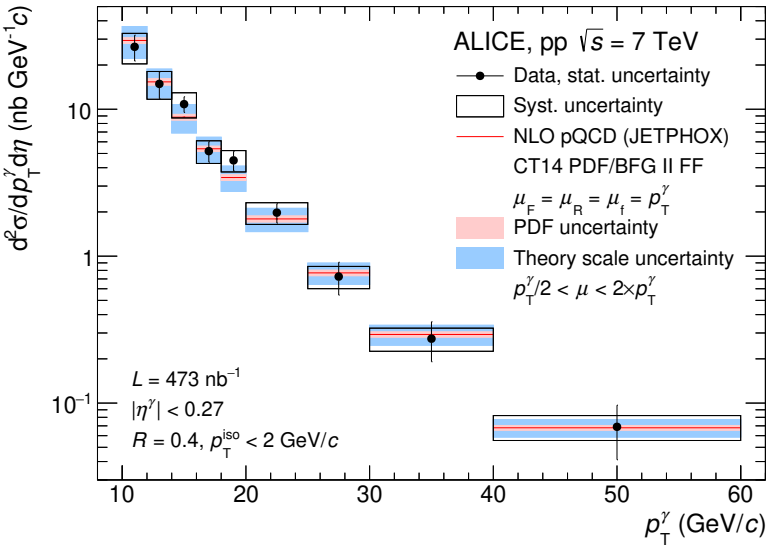

Figure 5.1: Isolated photon spectrum compared to a theory calculation [ALICE|19b].

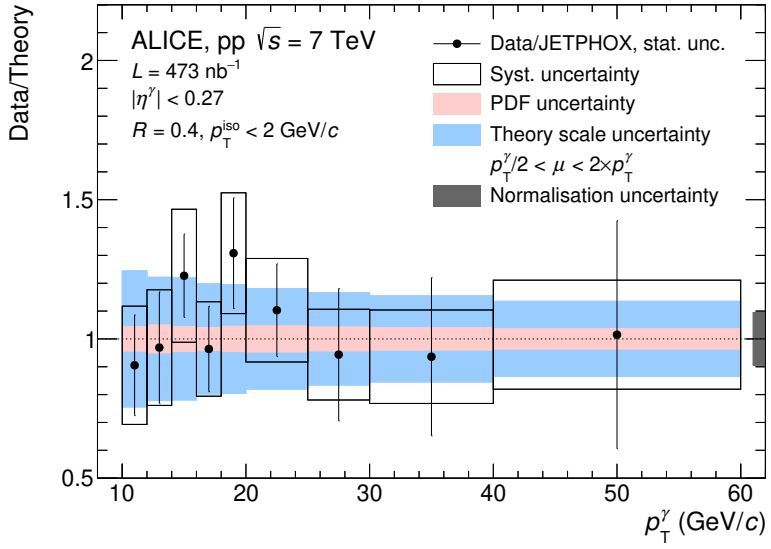

Figure 5.2: Ratio of isolated photon spectrum to a theory calculation [ALICE|19b].

measurements to lower x_T values. They also align to the previous measurements as far as it can be estimated on a double log plot. The extended reach to lower x_T values can be used to further constrain PDF functions for protons ([CC$^+$|13]), as well as the nuclear parton distribution function ([AE$^+$|11]) with future measurements in nuclear collisions.

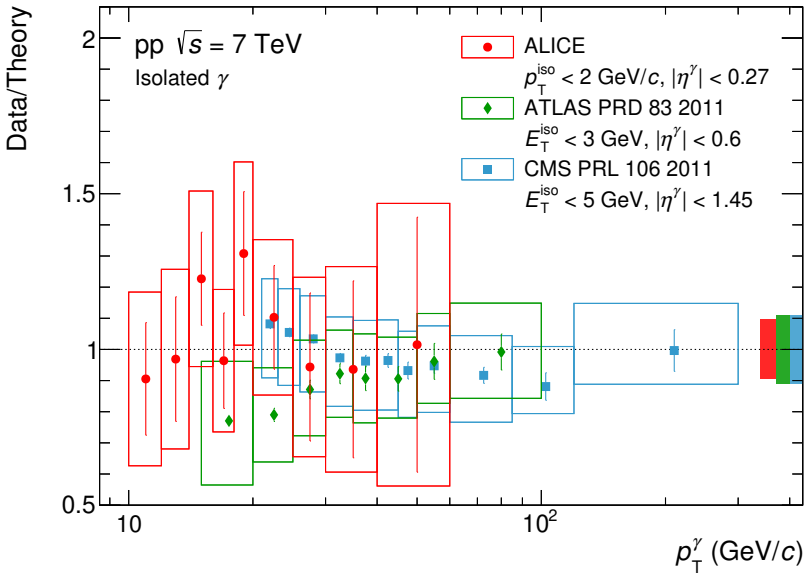

Figure 5.3: Comparison of ratios of isolated photon spectra to theory calculations, for results from ALICE, ATLAS and CMS [ALICE|19b].

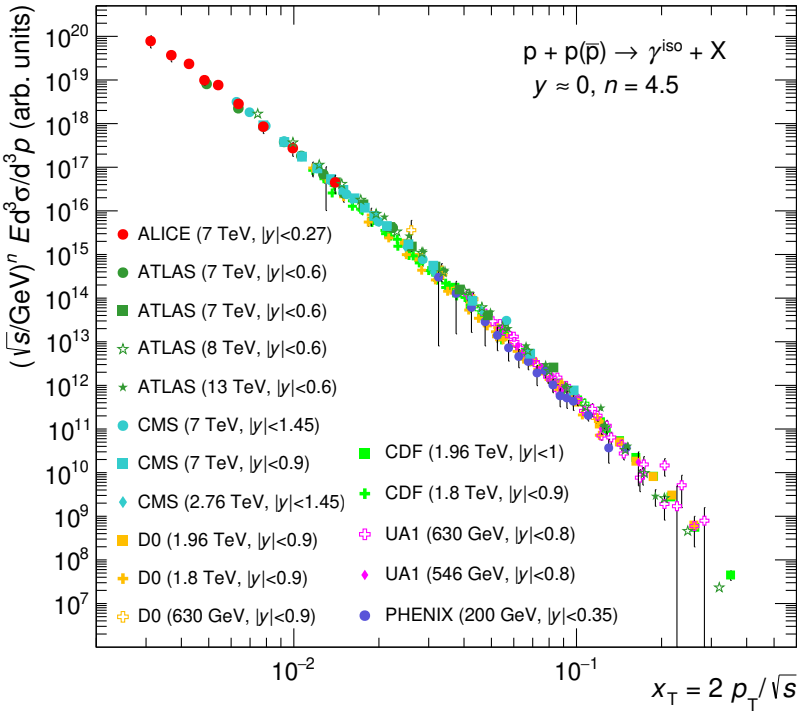

Figure 5.4: Isolated photon measurements for different experimental results as a function of x_T [ALICE|19b].

Summary & Outlook 6

In this thesis two observables are used to analyse particle collisions. Both analyses contributed to the successful publication of the related papers [ALICE|13d, ALICE|19b]. The two observables represent different cases regarding their usage to study heavy-ion collisions in ALICE. The analysis of $\langle p_{\mathrm{T}} \rangle$ of charged particles is an established analysis and is used to compare the results of three collision systems, these are pp, p–Pb, and Pb–Pb. In contrast, the focus of the isolated photon analysis was the creation, validation, and establishment of a reliable analysis technique and the publication of the first results with ALICE.

Direct comparison of $\langle p_{\mathrm{T}} \rangle$ in pp, p–Pb, and Pb–Pb collisions is performed in multiplicity bins and is limited to a maximum multiplicity of $n_{\mathrm{ch}} = 100$ as only for Pb–Pb collisions higher multiplicities are recorded in the analysed data sets. As already shown by other experiments ([EHS/NA22|88, CMS|13]) for all three collision systems the $\langle p_{\mathrm{T}} \rangle$ rises with increasing multiplicities. Despite the different slopes for the collision systems they show notable similarities. In all three cases the slope changes at a true multiplicity of $n_{\mathrm{ch}} = 14$. For higher multiplicities the slope reduces further. This effect is most pronounced in Pb–Pb collisions. The slope reduction can be further investigated for the pp and the p–Pb cases by analysing new data sets recorded with high-multiplicity triggers. The triggered data sets should provide smaller statistical uncertainties and a higher multiplicity reach. Data sets from additional collision systems and collision energies can round the picture of collision energy and system size off. They also provide the possibility to reduce a possible energy dependence of $\langle p_{\mathrm{T}} \rangle$, as for all collision systems recorded so far (pp, p–Pb, Pb–Pb, and Xe–Xe) a data set with a collision energy of approximately 5 TeV [1] exists. In addition, future $\langle p_{\mathrm{T}} \rangle$ analyses will profit from smaller uncertainties due to improvements in reconstruction and correction and especially from a Bayesian unfolding procedure to determine $\langle p_{\mathrm{T}} \rangle$ as function of n_{ch} ([ALICE|18]). For heavy-ion collisions a centrality-dependent analysis in multiplicity bins can provide further insight into the QGP, since centralities correspond to different overlaps and thus can be used to test the predictions made in [VH|82]. With the Xe-Xe data also a system-size dependent study is possible.

The results of the isolated photon measurement provides new values to test pertubative QCD calculations and further improve par-

1: For pp, p–Pb, and Pb–Pb data sets with a collision energy of 5.02 TeV were recorded, while the recorded data sets for Xe–Xe have a collision energy of 5.44 TeV.

ton distribution functions at low x_T values. Furthermore, the results represent the first isolated photon measurement by ALICE and probe a before uncharted x_T range. The method as well as the results are tested in multiple ways and include a evaluation of systematic uncertainties. To probe the influence of clusterizer settings, the analysis is repeated with different settings for clusterizer and clusterizer thresholds. The resulting comparison to the standard settings indicate stable and comparable outcome and support the final result. The cross-section as function of x_T surpass previous results in the low x_T regime (as indicated in figure 5.4). This reach can be extended by probing the same p_T range with data from higher collision energies, especially the $\sqrt{s} = 13\,\text{TeV}$ data set. With additional statistics also the overlap with results from CMS and ATLAS can be extended to provide additional cross-checks. Apart from further studies in pp, the $\mathcal{ABCD}$ method can be adapted with an additional background estimation for the underlying event, to be used in p–Pb and Pb–Pb analyses. The first studies for p–Pb collision are presented in [Mas|19]. The identification of isolated photons also provide the possibility to study γ-jet correlations to study medium properties in the future.

For both analyses, possibilities for additional studies are presented above. These studies will provide a better understanding of the observables, aside from the results presented in this thesis and may also reveal additional information about the QGP.

Appendices

Runs used for $\langle p_{\mathrm{T}} \rangle$ analysis A

Table A.1: Run list used for the $\langle p_{\mathrm{T}} \rangle$ analysis and the corresponding number of events after event selection for the centrailty selection 0 % - 100 %.

LHC10h		LHC10h		LHC10h	
Run	# Events	Run	# Events	Run	# Events
137161	55529	137693	12748	138653	378881
137162	41671	137704	130186	138662	201007
137231	135524	137718	45446	138666	223364
137232	47025	137722	302425	138730	40484
137235	13024	137724	48243	138732	19502
137236	27994	137751	116992	138837	227243
137243	25576	137752	176407	138870	72024
137366	190738	137844	790391	138871	35086
137431	178849	137848	63439	138872	14070
137432	77373	138190	150696	139028	32060
137434	64703	138192	370190	139029	97394
137439	9479	138197	117402	139036	118517
137440	34614	138201	204360	139037	100055
137441	79221	138225	245218	139038	319065
137443	16383	138275	1378945	139105	33192
137530	2472	138364	568316	139107	457169
137531	2621	138396	415187	139173	282030
137539	309692	138438	59813	139309	108465
137541	167926	138439	183064	139310	99070
137544	151801	138442	428186	139314	200978
137546	929	138469	146078	139328	132236
137549	280099	138534	1274353	139329	227662
137595	224116	138578	266922	139360	24027
137608	227323	138579	235203	139437	461837
137638	124465	138582	82628	139438	113067
137639	28466	138583	222555	139465	569481
137685	7259	138621	190880	139503	22551
137686	210434	138624	147221	139505	38971
137691	188299	138638	193690	139507	296860
137692	99679	138652	19912	139510	131010

B Runs used for isolated photon analysis

Table B.1: Run list used for the isolated photon analysis and the corresponding number of events after event selection.

LHC11c		LHC11c		LHC11d	
Run	# Events	Run	# Events	Run	# Events
154126	95815	154286	150445	156889	113001
154130	100378	154289	26753	156891	244162
154132	41133	154382	34880	156896	34581
154136	81141	154383	405792	157203	69748
154141	150071	154385	246936	157220	160088
154143	313104	154478	138005	157227	35760
154207	30425	154480	109387	157257	124002
154211	309285	154482	286302	157261	48683
154219	137597	154483	26585	157262	54704
154220	38374	154485	57367	157277	192693
154221	10100	154495	63644	157475	24263
154222	82401	154763	15054	157496	67530
154252	118268	154773	15424	157560	69959
154257	22968	154780	8279	157562	28377
154261	46788	154783	28186	157567	10897
154266	44200	154786	12036	157569	81222
154269	44706	154787	20291	157818	6771
154273	203175	154789	75913	157819	61828
154281	83123	154793	73298	157975	27281
154283	23459	154796	99160	157976	13397
		154808	293719	159254	55892
				159286	90296
				159532	76409
				159535	105786
				159575	23356
				159577	59459
				159580	132686
				159581	115966
				159582	487187

Bibliography

[AA+|10] J. Alme et al., *The ALICE TPC, a large 3-dimensional tracking device with fast readout for ultra-high multiplicity events*, Nucl.Instrum.Meth. **A622**, 316 (2010), arxiv: 1001.1950, doi: 10.1016/j.nima.2010.04.042.

[AB+|89] P. Aurenche et al., *The Gluon Contents of the Nucleon Probed with Real and Virtual Photons*, Phys. Rev. **D39**, 3275 (1989), doi: 10.1103/PhysRevD.39.3275.

[ABM+|07] A. Andronic et al., *Statistical hadronization of heavy quarks in ultra-relativistic nucleus-nucleus collisions*, Nucl. Phys. **A789**, 334 (2007), arxiv: nucl-th/0611023, doi: 10.1016/j.nuclphysa.2007.02.013.

[AE+|11] F. Arleo et al., *Inclusive prompt photon production in nuclear collisions at RHIC and LHC*, Journal of High Energy Physics **2011**(4) (2011), arxiv: 1103.1471, doi: 10.1007/jhep04(2011)055.

[ALICE|06] C. W. Fabjan et al. (ALICE Collaboration), *ALICE: Physics performance report, volume II*, J. Phys. **G32**, 1295 (2006), doi: 10.1088/0954-3899/32/10/001.

[ALICE|08a] K. Aamodt et al. (ALICE Collaboration), *The ALICE experiment at the CERN LHC. A Large Ion Collider Experiment*, JINST **3**, S08002 (2008), doi: 10.1088/1748-0221/3/08/S08002.

[ALICE|08b] P. Cortese et al. (ALICE Collaboration), *ALICE electromagnetic calorimeter technical design report*, Technical report, CERN, 2008.

[ALICE|12] K. Aamodt et al. (ALICE Collaboration), *Particle-yield modification in jet-like azimuthal di-hadron correlations in Pb–Pb collisions at* $\sqrt{s_{\mathrm{NN}}}$ = 2.76 TeV, Phys. Rev. Lett. **108**, 092301 (2012), arxiv: 1110.0121, doi: 10.1103/PhysRevLett.108.092301.

[ALICE|13a] B. B. Abelev et al. (ALICE Collaboration), *Centrality Dependence of Charged Particle Production at Large Transverse Momentum in Pb–Pb Collisions at* $\sqrt{s_{\mathrm{NN}}}$ = 2.76 *TeV*, Phys. Lett. **B720**, 52 (2013), arxiv: 1208.2711, doi: 10.1016/j.physletb.2013.01.051.

[ALICE|13b] B. B. Abelev et al. (ALICE Collaboration), *Centrality dependence of π, K, p production in Pb–Pb collisions at* $\sqrt{s_{NN}}$ = 2.76 TeV, Phys. Rev. **C88**, 044910 (2013), arxiv: 1303.0737, doi: 10.1103/PhysRevC.88.044910.

[ALICE|13c] B. B. Abelev et al. (ALICE Collaboration), *Centrality determination of Pb–Pb collisions at* $\sqrt{s_{\mathrm{NN}}}$ = *2.76 TeV with ALICE*, Phys. Rev. **C88**, 044909 (2013), arxiv: 1301.4361, doi: 10.1103/PhysRevC.88.044909.

[ALICE|13d] B. B. Abelev et al. (ALICE Collaboration), *Multiplicity dependence of the average transverse momentum in pp, p–Pb, and Pb–Pb collisions at the LHC*, Phys. Lett. **B727**, 371 (2013), arxiv: 1307.1094, doi: 10.1016/j.physletb.2013.10.054.

[ALICE|14] B. B. Abelev et al. (ALICE Collaboration), *Measurement of quarkonium production at forward rapidity in pp collisions at $\sqrt{s}$= 7 TeV*, The European Physical Journal C **74**, 2974 (2014), arxiv: 1403.3648v2, doi: 10.1140/epjc/s10052-014-2974-4.

[ALICE|15] B. B. Abelev et al. (ALICE Collaboration), *$K^*(892)^0$ and $\phi(1020)$ production in Pb–Pb collisions at $\sqrt{s_{\mathrm{NN}}}$ = 2.76 TeV*, Phys. Rev. **C91**, 024609 (2015), arxiv: 1404.0495, doi: 10.1103/PhysRevC.91.024609.

[ALICE|16] J. Adam et al. (ALICE Collaboration), *Search for weakly decaying $\overline{\Lambda}\overline{\mathrm{n}}$ and $\Lambda\Lambda$ exotic bound states in central Pb–Pb collisions at $\sqrt{s_{\mathrm{NN}}}$ = 2.76 TeV*, Phys. Lett. **B752**, 267 (2016), arxiv: 1506.07499, doi: 10.1016/j.physletb.2015.11.048.

[ALICE|17a] S. Acharya et al. (ALICE Collaboration), *The ALICE definition of primary particles*, (2017), https://cds.cern.ch/record/2270008.

[ALICE|17b] J. Adam et al. (ALICE Collaboration), *Measurement of the production of high-p_{T} electrons from heavy-flavour hadron decays in Pb-Pb collisions at $\sqrt{s_{\mathrm{NN}}}$ = 2.76 TeV*, Phys.Lett.B **771**, 467–481 (2017), arxiv: 1609.07104, doi: 10.1016/j.physletb.2017.05.060.

[ALICE|17c] R. T. Jiménez Bustamante (ALICE Collaboration), *Light flavour hadron production in pp collisions at $\sqrt{s}$ = 13 TeV with ALICE*, J. Phys. Conf. Ser. **832**, 012015 (2017), arxiv: 1702.06621, doi: 10.1088/1742-6596/832/1/012015.

[ALICE|17d] E. Perez Lezama (ALICE Collaboration), *Transverse momentum spectra and the nuclear modification factor of charged particles with ALICE*, J. Phys. Conf. Ser. **832**, 012009 (2017), doi: 10.1088/1742-6596/832/1/012009.

[ALICE|18] M. Krüger (ALICE Collaboration), *Bayesian unfolding of charged particle p_{T} spectra with ALICE at the LHC*, PoS **Confinement2018**, 236 (2018), arxiv: 1909.06109, doi: 10.22323/1.336.0236.

[ALICE|19a] S. Acharya et al. (ALICE Collaboration), *Direct photon production at low transverse momentum in proton-proton collisions at $\sqrt{\mathbf{s}}$ = 2.76 and 8 TeV*, Phys.Rev.C **99**(2), 024912 (2019), arxiv: 1803.09857, doi: 10.1103/PhysRevC.99.024912.

[ALICE|19b] S. Acharya et al. (ALICE Collaboration), *Measurement of the inclusive isolated photon production cross section in pp collisions at $\sqrt{s}$ = 7 TeV*, Eur.Phys.J.C **79**(11), 896 (2019), arxiv: 1906.01371, doi: 10.1140/epjc/s10052-019-7389-9.

[AO$^+$|92] T. Awes et al., *A Simple method of shower localization and identification in laterally segmented calorimeters*, Nucl.Instrum.Meth.A **311**, 130–138 (1992), doi: 10.1016/0168-9002(92)90858-2.

[ATLAS|05] H. H. J. ten Kate (ATLAS Collaboration), *ATLAS superconducting toroids and solenoid*, IEEE Trans. Appl. Supercond. **15**, 1267 (2005), doi: 10.1109/TASC.2005.849560.

[ATLAS|08] G. Aad et al. (ATLAS Collaboration), *The ATLAS Experiment at the CERN Large Hadron Collider*, JINST **3**, S08003 (2008), doi: 10.1088/1748-0221/3/08/S08003.

[ATLAS|11a] G. Aad et al. (ATLAS Collaboration), *Measurement of the inclusive isolated prompt photon cross section in pp collisions at $\sqrt{s}$ = 7 TeV with the ATLAS detector*, Phys. Rev. **D83**, 052005 (2011), arxiv: 1012.4389, doi: 10.1103/PhysRevD.83.052005.

[ATLAS|11b] G. Aad et al. (ATLAS Collaboration), *Search for the Standard Model Higgs boson in the two photon decay channel with the ATLAS detector at the LHC*, Phys. Lett. **B705**, 452–470 (2011), arxiv: 1108.5895, doi: 10.1016/j.physletb.2011.10.051.

[ATLAS|12] G. Aad et al. (ATLAS Collaboration), *Observation of a new particle in the search for the Standard Model Higgs boson with the ATLAS detector at the LHC*, Phys. Lett. **B716**, 1 (2012), arxiv: 1207.7214, doi: 10.1016/j.physletb.2012.08.020.

[B$^+$|69] E. D. Bloom et al., *High-Energy Inelastic e p Scattering at 6-Degrees and 10-Degrees*, Phys. Rev. Lett. **23**, 930–934 (1969), doi: 10.1103/PhysRevLett.23.930.

[BB$^+$|94] R. Brun et al., *GEANT: Detector Description and Simulation Tool*, 1994, doi: 10.17181/CERN.MUHF.DMJ1.

[BF$^+$|69] M. Breidenbach et al., *Observed Behavior of Highly Inelastic electron-Proton Scattering*, Phys. Rev. Lett. **23**, 935–939 (1969), doi: 10.1103/PhysRevLett.23.935.

[BK$^+$|95] T. Blum et al., *The beta function and equation of state for QCD with two flavors of quarks*, Phys. Rev. **D51**, 5153–5164 (1995), arxiv: hep-lat/9410014, doi: 10.1103/PhysRevD.51.5153.

[Boo|15] J. Book, *J/Ψ Production in Pb–Pb Collisions with ALICE at the LHC*, PhD thesis, Frankfurt U., Frankfurt, 2015, https://www.uni-frankfurt.de/54952831/PHD_THESIS_JULIAN_BOOK.pdf.

[CB|05] G. Conesa-Balbastre, *Identification of particles and hard processes with the spectrometer PHOS of the ALICE experiment*, PhD thesis, Valencia U., 2005, https://cds.cern.ch/record/988780.

[CB|18] G. Conesa-Balbastre, *Study and emulation of cell energy cross-talk in EMCal*, Internal ALICE-Analysis note, ANA-837, 2018.

[CB|19] G. Conesa Balbastre, *Study of the strong interaction with high-energy photons at the LHC: Experience with the ALICE-EMCal detector operation and measurements*, Habilitation à diriger des recherches, UGA (Université Grenoble Alpes), 2019, https://tel.archives-ouvertes.fr/tel-02306044.

[CC$^+$|13] L. Carminati et al., *Sensitivity of the LHC isolated-gamma+jet data to the parton distribution functions of the proton*, EPL **101**(6), 61002 (2013), arxiv: 1212.5511, doi: 10.1209/0295-5075/101/61002.

[CDF|09] T. Aaltonen et al. (CDF Collaboration), *Search for a Fermiophobic Higgs Boson Decaying into Diphotons in p anti-p Collisions at s**(1/2) = 1.96-TeV*, Phys. Rev. Lett. **103**, 061803 (2009), arxiv: 0905.0413, doi: 10.1103/PhysRevLett.103.061803.

[Cha|32] J. Chadwick, *Possible Existence of a Neutron*, Nature **129**, 312 (1932), doi: 10.1038/129312a0.

[CMS|08] S. Chatrchyan et al. (CMS Collaboration), *The CMS experiment at the CERN LHC. The Compact Muon Solenoid experiment*, JINST **3**, S08004 (2008), doi: 10.1088/1748-0221/3/08/S08004.

[CMS|11] V. Khachatryan et al. (CMS Collaboration), *Measurement of the Isolated Prompt Photon Production Cross Section in pp Collisions at $\sqrt{s}$ = 7 TeV*, Phys. Rev. Lett. **106**, 082001 (2011), arxiv: 1012.0799, doi: 10.1103/PhysRevLett.106.082001.

[CMS|12a] S. Chatrchyan et al. (CMS Collaboration), *Observation of a new boson at a mass of 125 GeV with the CMS experiment at the LHC*, Phys. Lett. **B716**, 30 (2012), arxiv: 1207.7235, doi: 10.1016/j.physletb.2012.08.021.

[CMS|12b] S. Chatrchyan et al. (CMS Collaboration), *Search for the standard model Higgs boson decaying into two photons in pp collisions at $\sqrt{s}$ = 7 TeV*, Phys. Lett. **B710**, 403–425 (2012), arxiv: 1202.1487, doi: 10.1016/j.physletb.2012.03.003.

[CMS|13] S. Chatrchyan et al. (CMS Collaboration), *Measurement of the elliptic anisotropy of charged particles produced in PbPb collisions at $\sqrt{s_{NN}}$=2.76 TeV*, Phys. Rev. **C87**, 014902 (2013), arxiv: 1204.1409, doi: 10.1103/PhysRevC.87.014902.

[CMS|17] V. Khachatryan et al. (CMS Collaboration), *Suppression of $\Upsilon(1S)$, $\Upsilon(2S)$ and $\Upsilon(3S)$ production in PbPb collisions at $\sqrt{s_{\mathrm{NN}}}$ = 2.76 TeV*, Phys. Lett. **B770**, 357 (2017), arxiv: 1611.01510, doi: 10.1016/j.physletb.2017.04.031.

[CP|75] N. Cabibbo and G. Parisi, *Exponential Hadronic Spectrum and Quark Liberation*, Phys. Lett. **59B**, 67 (1975), doi: 10.1016/0370-2693(75)90158-6.

[D0|09] V. M. Abazov et al. (D0 Collaboration), *Search for Resonant Diphoton Production with the D0 Detector*, Phys. Rev. Lett. **102**, 231801 (2009), arxiv: 0901.1887, doi: 10.1103/PhysRevLett.102.231801.

[DM|16] C. De Melis, *The CERN accelerator complex. Complexe des accélérateurs du CERN*, 2016, https://cds.cern.ch/record/2119882.

[dR|12] D. d'Enterria and J. Rojo, *Quantitative constraints on the gluon distribution function in the proton from collider isolated-photon data*, Nucl. Phys. **B860**, 311 (2012), arxiv: 1202.1762, doi: 10.1016/j.nuclphysb.2012.03.003.

[EHS/NA22|88] V. V. Aivazian et al. (EHS/NA22 Collaboration), *Multiplicity Dependence of the Average Transverse Momentum in $\pi^+ p$, $K^+ p$ and pp Collisions at 250-GeV/c*, Phys. Lett. **B209**, 103 (1988), doi: 10.1016/0370-2693(88)91839-4.

[EMCal|10] J. Allen et al. (ALICE EMCal Collaboration), *Performance of prototypes for the ALICE electromagnetic calorimeter*, Nucl.Instrum.Meth.A **615**, 6–13 (2010), arxiv: 0912.2005, doi: 10.1016/j.nima.2009.12.061.

[Fab|87] C. W. Fabjan, *Experimental Techniques in High-Energy Nuclear and Particle Physics (2nd Edition)*, World Scientific Publishing Co. Pte. Ltd., 1987, doi: 10.1142/9789814355988.

[FG|03] C. W. Fabjan and F. Gianotti, *Calorimetry for particle physics*, Rev. Mod. Phys. **75**, 1243 (2003), doi: 10.1103/RevModPhys.75.1243.

[G$^+$|91] H. H. Gutbrod et al., *Proposal for a large acceptance hadron and photon spectrometer*, Technical report, CERN, 1991.

[Gargamelle|73] F. Hasert et al. (Gargamelle Collaboration), *Observation of Neutrino Like Interactions Without Muon Or Electron in the Gargamelle Neutrino Experiment*, Phys. Lett. **46B**(1), 138–140 (1973), doi: 10.1016/0370-2693(73)90499-1.

[GEANT4|03] S. Agostinelli et al. (GEANT4 Collaboration), *GEANT4: A Simulation toolkit*, Nucl. Instrum. Meth. **A506**, 250 (2003), doi: 10.1016/S0168-9002(03)01368-8.

[GL$^+$|18] M. Germain et al., *Isolated direct photon cross section measurement in pp collisions at $\sqrt{s}$ = 7 TeV with the ALICE detector at LHC*, Internal ALICE-Analysis note, ANA-295, 2018.

[GM|64] M. Gell-Mann, *A Schematic Model of Baryons and Mesons*, Phys. Lett. **8**, 214–215 (1964), doi: 10.1016/S0031-9163(64)92001-3.

[Gri|08] D. J. Griffiths, *Introduction to Elementary Particles*, Wiley, 2008, ISBN: 978-3527406012.

[HF$^+$|73] F. Hasert et al., *Search for Elastic ν_μ Electron Scattering*, Phys. Lett. **46B**(1), 121–124 (1973), doi: 10.1016/0370-2693(73)90494-2.

[HM|96] J. W. Harris and B. Müller, *The Search for the quark - gluon plasma*, Ann. Rev. Nucl. Part. Sci. **46**, 71 (1996), arxiv: hep-ph/9602235, doi: 10.1146/annurev.nucl.46.1.71.

[Id|10] R. Ichou and D. d'Enterria, *Sensitivity of isolated photon production at TeV hadron colliders to the gluon distribution in the proton*, Phys. Rev. **D82**, 014015 (2010), arxiv: 1005.4529, doi: 10.1103/PhysRevD.82.014015.

[Kal|12] A. Kalweit, *Production of light flavor hadrons and anti-nuclei at the LHC*, PhD thesis, Darmstadt, Tech. U., 2012, https://cds.cern.ch/record/2119440.

[Kar|15] B. Kardan, *Centrality Determination at 1.23 AGeV Gold-Gold collision and readout-electronics for the HADES electromagnetic calorimeter*, Diploma thesis, Frankfurt U., Frankfurt, 2015, https://hades.gsi.de/sites/default/files/web/media/documents/thesis/Diploma/diplom_thesis_kardan_final_22.06.2015_small.pdf.

[Kle|14] J. Klein, *Jet Physics with A Large Ion Collider Experiment at the Large Hadron Collider*, PhD thesis, Heidelberg U., 2014, https://cds.cern.ch/record/1973326.

[Kni|15] M. L. Knichel, *Transverse momentum distributions of primary charged particles in pp, p–Pb and Pb–Pb collisions measured with ALICE at the LHC*, PhD thesis, Darmstadt, Tech. U., 2015, https://cds.cern.ch/record/2119438.

[Krü|17] M. Krüger, *Mean transverse momentum of primary charged particles produced in pp collisions at $\sqrt{s}$ = 5.02 TeV measured with ALICE*, Master's thesis, Frankfurt U., Frankfurt, 2017.

[KS$^+$|10] M. Kliemant et al., *Global Properties of Nucleus-Nucleus Collisions*, Lect. Notes Phys. **785**, 23–103 (2010), arxiv: 0809.2482, doi: 10.1007/978-3-642-02286-9_2.

[LHCb|08] A. A. Alves, Jr. et al. (LHCb Collaboration), *The LHCb Detector at the LHC*, JINST **3**, S08005 (2008), doi: 10.1088/1748-0221/3/08/S08005.

[Lod|18] D. F. Lodato, *Measurement of the prompt photon production cross section in proton-proton collisions at $\sqrt{s}$ = 7 TeV with ALICE*, PhD thesis, Utrecht U., 2018, https://cds.cern.ch/record/2304097.

[Mar|12] M. Marquard, *Mittlerer Transversalimpuls in Pb–Pb Kollisionen mit ALICE*, Master's thesis, Frankfurt U., Frankfurt, 2012, http://www.uni-frankfurt.de/48070243/Masterarbeit_Marquard.pdf.

[Mas|19] E. Masson, *Mesure de la production de photons isolés dans les collisions proton-proton et proton-plomb au LHC avec l'expérience ALICE*, PhD thesis, SUBATECH, Nantes, 2019, https://tel.archives-ouvertes.fr/tel-02383220.

[MR$^+$|07] M. L. Miller et al., *Glauber modeling in high energy nuclear collisions*, Ann. Rev. Nucl. Part. Sci. **57**, 205 (2007), arxiv: nucl-ex/0701025, doi: 10.1146/annurev.nucl.57.090506.123020.

[MS|86] T. Matsui and H. Satz, *J/ψ Suppression by Quark-Gluon Plasma Formation*, Phys. Lett. **B178**, 416 (1986), doi: 10.1016/0370-2693(86)91404-8.

[NA35|91] A. D. Panagiotou, A. Petridis and G. Vasileiadis (NA35 Collaboration), *Large acceptance hadron detector for an investigation of Pb-induced reactions at the CERN SPS*, Technical Report CERN-SPSLC-91-31. SPSLC-P-264, CERN, Geneva, 1991, https://cds.cern.ch/record/295042.

[Paq|17] J.-F. Paquet, *Overview of electromagnetic probe production in ultra-relativistic heavy ion collisions*, J. Phys. Conf. Ser. **832**(1), 012035 (2017), arxiv: 1611.05020, doi: 10.1088/1742-6596/832/1/012035.

[PDG|02] K. Hagiwara et al. (PDG Collaboration), *Review of particle physics*, Phys. Rev. **D66**, 010001 (2002), doi: 10.1103/PhysRevD.66.010001.

[PDG|16] C. Patrignani et al. (PDG Collaboration), *Review of Particle Physics*, Chin. Phys. **C40**, 100001 (2016), doi: 10.1088/1674-1137/40/10/100001.

[PHENIX|03] K. Adcox et al. (PHENIX Collaboration), *PHENIX detector overview*, Nucl. Instrum. Meth. **A499**, 469 (2003), doi: 10.1016/S0168-9002(02)01950-2.

[PHENIX|13] B. Sahlmueller (PHENIX Collaboration), *Direct Photon Measurements at PHENIX*, Nucl. Phys. **A910-911**, 209 (2013), arxiv: 1207.7115, doi: 10.1016/j.nuclphysa.2012.12.086.

[Phi|13] O. Philipsen, *The QCD equation of state from the lattice*, Prog. Part. Nucl. Phys. **70**, 55–107 (2013), arxiv: 1207.5999, doi: 10.1016/j.ppnp.2012.09.003.

[PK$^+$|15] T. Pierog et al., *EPOS LHC: Test of collective hadronization with data measured at the CERN Large Hadron Collider*, Phys. Rev. **C92**, 034906 (2015), arxiv: 1306.0121, doi: 10.1103/PhysRevC.92.034906.

[PLUTO|78] C. Berger et al. (PLUTO Collaboration), *A Study of Jets in electron Positron Annihilation Into Hadrons in the Energy Range 3.1-GeV to 9.5-GeV*, Phys. Lett. **78B**, 176–182 (1978), doi: 10.1016/0370-2693(78)90377-5.

[PLUTO|79] C. Berger et al. (PLUTO Collaboration), *Evidence for Gluon Bremsstrahlung in e+ e- Annihilations at High-Energies*, Phys. Lett. **86B**, 418–425 (1979), doi: 10.1016/0370-2693(79)90869-4.

[Ros|14] A. D. Rosso, *Particle kickers. Aiguiller les particules*, CERN Bulletin **24/2014** (2014), `https://cds.cern.ch/record/1706606`.

[Rut|11] E. Rutherford, *The scattering of alpha and beta particles by matter and the structure of the atom*, Phil. Mag. Ser.6 **21**, 669 (1911), doi: 10.1080/14786440508637080.

[Sak|08] T. Sakaguchi, *Direct photons basis for characterizing heavy ion collisions* , J. Phys. **G35**, 104025 (2008), arxiv: 0805.4644, doi: 10.1088/0954-3899/35/10/104025.

[SMS|06] T. Sjöstrand, S. Mrenna and P. Z. Skands, *PYTHIA 6.4 Physics and Manual*, JHEP **05**, 026 (2006), arxiv: hep-ph/0603175, doi: 10.1088/1126-6708/2006/05/026.

[STAR|03] K. H. Ackermann et al. (STAR Collaboration), *STAR detector overview*, Nucl. Instrum. Meth. **A499**, 624 (2003), doi: 10.1016/S0168-9002(02)01960-5.

[UA1|83a] G. Arnison et al. (UA1 Collaboration), *Experimental Observation of Isolated Large Transverse Energy Electrons with Associated Missing Energy at s**(1/2) = 540-GeV*, Phys. Lett. **122B**(1), 103–116 (1983), doi: 10.1016/0370-2693(83)91177-2.

[UA1|83b] G. Arnison et al. (UA1 Collaboration), *Experimental Observation of Lepton Pairs of Invariant Mass Around 95-GeV/c**2 at the CERN SPS Collider*, Phys. Lett. **126B**(5), 398–410 (1983), doi: 10.1016/0370-2693(83)90188-0.

[UA2|83a] P. Bagnaia et al. (UA2 Collaboration), *Evidence for Z0 —> e+ e- at the CERN anti-p p Collider*, Phys. Lett. **129B**(1-2), 130–140 (1983), doi: 10.1016/0370-2693(83)90744-X.

[UA2|83b] M. Banner et al. (UA2 Collaboration), *Observation of Single Isolated Electrons of High Transverse Momentum in Events with Missing Transverse Energy at the CERN anti-p p Collider*, Phys. Lett. **122B**(5-6), 476–485 (1983), doi: 10.1016/0370-2693(83)91605-2.

[VH|82] L. Van Hove, *Multiplicity Dependence of p(T) Spectrum as a Possible Signal for a Phase Transition in Hadronic Collisions*, Phys. Lett. **B118**(1-3), 138–140 (1982), doi: 10.1016/0370-2693(82)90617-7.

[WG|91] X.-N. Wang and M. Gyulassy, *HIJING: A Monte Carlo model for multiple jet production in p p, p A and A A collisions*, Phys. Rev. **D44**, 3501–3516 (1991), doi: 10.1103/PhysRevD.44.3501.

[Wie|08] J. Wiechula, *Inbetriebnahme und Kalibrierung der ALICE-TPC*, PhD thesis, Frankfurt U., Frankfurt, 2008, https://cds.cern.ch/record/1295506.

[Wol|14] B. Wolfart, *Vergleich von Algorithmen zur Rekonstruktion von Clustern auf dem EMCal*, Bachelor's thesis, Frankfurt U., Frankfurt, 2014.

[Zwe|64] G. Zweig, *An SU_3 model for strong interaction symmetry and its breaking; Version 2*, (CERN-TH-412), 80 p (1964), https://cds.cern.ch/record/570209, Version 1 is CERN preprint 8182/TH.401, Jan. 17, 1964.